TECHNISCHE UNIVERSITÄT MÜNCHEN

Lehrstuhl für experimentelle Halbleiterphysik E24
Walter Schottky Institut

Growth and Properties of In(Ga)As Nanowires on Silicon

Simon Hertenberger

Vollständiger Abdruck der von der Fakultät für Physik der Technischen Universität München zur Erlangung des akademischen Grades eines

Doktors der Naturwissenschaften

genehmigten Dissertation.

Vorsitzender: Univ.-Prof. Dr. Peter Vogl
Prüfer der Dissertation:
1. Univ.-Prof. Dr. Gerhard Abstreiter
2. Univ.-Prof. Dr. Johannes Barth

Die Dissertation wurde am 27.06.2012 bei der Technischen Universität München eingereicht und durch die Fakultät für Physik am 09.08.2012 angenommen.

Abstract

In this thesis the integration of III–V semiconductor nanowires on silicon (Si) platform by molecular beam epitaxy (MBE) is investigated. All nanowires are grown without the use of foreign catalysts such as Au to achieve high purity material. First, InAs nanowires are grown in a self-assembled manner on SiO_x-masked Si(111) where pinholes in the silicon oxide serve as nucleation spots for the nanowires. This leads to the growth of vertically aligned, (111)-oriented nanowires with hexagonal cross-section. Based on this simple process, the entire growth parameter window is investigated for InAs nanowires, revealing an extremely large growth temperature range from 380 ℃ to 580 ℃ and growth rates as large as 6 µm/h. Complex quantitative *in-situ* line-of-sight quadrupole mass spectrometry experiments during nanowire growth and post-growth thermal decomposition studies support these findings and indicate a very high thermal stability up to >540 ℃ for InAs nanowires. Furthermore, the influence of the As/In ratio on the nanowire growth is studied revealing two distinct growth regimes, i.e., an In-rich regime for lower As fluxes and an As-rich regime for larger As fluxes, where the latter shows characteristic saturation of the nanowire aspect ratio.

For the catalyst-free growth, detailed investigation of the growth mechanism is performed via a combination of *in-situ* reflection high-energy electron diffraction (RHEED) and *ex-situ* scanning and transmission electron microscopy (SEM, TEM). An abrupt onset of nanowire growth is observed in RHEED intensity and in-plane lattice parameter evolution. Furthermore, completely droplet-free nanowires, continuous radial growth, constant vertical growth rate and growth interruption experiments suggest a vapor-solid growth mode for all investigated nanowire samples.

Moreover, site-selective (positioned) growth of InAs nanowires on pre-patterned SiO_2 masked Si(111) substrates is demonstrated which is needed for ultimate control of nanowire properties and homogeneous array-like characteristics. High vertical growth yields of 90 % are achieved on substrates patterned either by e-beam lithography (for small scale arrays) or nanoimprint lithography (NIL, for large scale arrays > 5×5 mm^2). In addition, X-ray rocking curve measurements evidence very low crystal tilt and perfect vertical alignment along

the (111) direction with full widths at half maximum (FWHM) as low as 0.6°. Furthermore, systematic investigations of the size scaling behavior as a function of the pitch (interwire distance) highlight the existence of two growth regimes: (i) a competitive growth regime for narrow pitches and (ii) a diffusion-limited regime for wider pitches, where growth is limited by the diffusion length of In adatoms on the SiO_2 surface ($\sim$750 nm at T = 480 °C).

Furthermore, the growth of ternary InGaAs nanowires on sputter-deposited SiO_x/Si(111) and NIL-patterned SiO_2/Si(111) substrates is investigated. Here, composition tuning with Ga contents ranging from 0–60 % was achieved as confirmed by X-ray diffraction and energy dispersive X-ray spectroscopy. Furthermore, the two different growth strategies are compared yielding a significantly lower FWHM of the 2θ-XRD-peak in the case of NIL-patterned substrates (0.031°) as compared to self-assembled grown nanowires (0.084°). This finding is further supported by Raman spectroscopy showing lower longitudinal optical to transversal optical (LO/TO) intensity ratios and lower LO-FWHM for both the InAs-like and GaAs-like LO modes in the case of NIL-patterned nanowire growth. These observations indicate superior composition homogeneity for positioned nanowire growth on patterned substrates. In addition, low-T photoluminescence (PL) measurements are presented showing band gap tuning over a wavelength range of $\sim$1800–2850 nm where PL peak linewidths are as narrow as $\sim$30 meV, independent of the Ga content.

Finally, the effect of growth parameters on the microstructure are investigated by TEM and XRD analysis revealing a disordered wurtzite (WZ) structure with stacking faults occurring every few monolayers to nanometers for InAs nanowires grown under different As/In ratios. However, the nanowire growth temperature is found to influence the crystal structure more significantly, such that longer phase pure WZ segments up to lengths of >10 nm are observed for elevated growth temperatures ($\geq$530 °C). Furthermore, InAs nanowire ensembles with different diameter (40–135 nm) are investigated by low-temperature PL spectroscopy. The nanowires show relatively strong emission efficiency, characteristic red-shift with temperature and low-temperature band-edge energy position of $\sim$0.41 eV for thick nanowires. Reduction in nanowire diameter yields a characteristic blue-shift which is related to quantum confinement effects as confirmed by simulations.

The good control about In(Ga)As nanowire growth on Si and the obtained understanding of important physical properties as discussed in this thesis provide a valuable basis for the development of effective high-quality nanowire-based devices.

Zusammenfassung

In dieser Arbeit wird die Integration von III–V Halbleiternanodrähten auf Silizium (Si) mit Molekularstrahlepitaxie (MBE) untersucht. Um ein hochreines Material zu erhalten, werden alle Nanodrähte ohne fremde Katalysatoren wie z.B. Au gewachsen. Zuerst werden InAs Nanodrähte auf selbstorganisierte Weise auf SiO_x/Si(111) gewachsen, wobei Poren im Siliziumoxid als Nukleationsspunkte für die Nanodrähte dienen. Dies führt zu vertikal angeordneten, (111)-orientierten Nanodrähten mit hexagonalem Querschnitt. Die Untersuchung des gesamten Wachstumsparameterbereiches für InAs Nanodrähte bringt einen außergewöhnlich hohen Temperaturbereich von 380 °C bis 580 °C und Wachstumsraten bis hin zu 6 µm/h zum Vorschein. Quantitative *in-situ* Experimente mit einem Massenspektrometer, das auf das Substrat gerichtet ist, deuten auf eine sehr hohe thermische Stabilität der InAs Nanodrähte bis zu >540 °C hin. Des Weiteren zeigen Studien zum Einfluss des As/In Verhältnisses auf das Nanodrahtwachstum, dass es zwei unterschiedliche Wachstumsregime gibt, d.h. ein In-reiches Regime für niedrigere As Flüsse und ein As-reiches Regime für höhere As Flüsse. Im As-reichen Regime ist das Seitenverhältnis der Nanodrähte konstant und vom As Fluss unabhängig.

Außerdem wird eine detaillierte Untersuchung des Wachstumsmechanismusses mit einer Kombination aus *in-situ* Beugung hochenergetischer Elektronen bei Reflexion (RHEED) und *ex-situ* Raster- und Transmissionselektronenmikroskopie (SEM, TEM) durchgeführt. Der zeitliche Verlauf der RHEED Intensität und der Gitterkonstanten zeigt einen abrupten Beginn des Nanodrahtwachstums ohne Nukleationsverzögerung. Des Weiteren legen die komplett tropfenfreien Nanodrähte, das kontinuierliche radiale Wachstum, eine konstante vertikale Wachstumsrate und Wachstumsunterbrechungs-Experimente einen katalysatorfreien (d.h. tropfenfreien) Mechanismus nahe.

Darüber hinaus wird ortsselektives (positioniertes) Nanodrahtwachstum auf strukturierten SiO_2/Si(111) Substraten gezeigt, das für die vollständige Kontrolle der Nanodrahteigenschaften benötigt wird. Auf den Substraten, die entweder mit Elektronenstrahllithographie oder Nanoimprintlithographie strukturiert sind, werden hohe vertikale Wachstumsausbeu-

ten von 90 % erreicht. Außerdem bestätigen Röntgendiffraktometriemessungen (XRD) mit einer niedrigen Halbwertsbreite der Rocking-Kurve von 0.6° die sehr geringe Kristallneigung und die perfekte Anordnung entlang der (111) Richtung. Des Weiteren zeigen Untersuchungen der Nanodrahtdimensionen in Abhängigkeit ihres Abstandes die Existenz zweier Wachstumsregime: (i) ein kompetitives Wachstumsregime für kleine Abstände und (ii) ein diffusionslimitiertes Regime für größeren Abstand, in dem das Wachstum durch die Diffusionslänge der In Adatome auf der SiO_2 Oberfläche limitiert ist ($\sim$750 nm bei 480 °C).

Außerdem wurde das Wachstum ternärer InGaAs Nanodrähte auf gesputterten SiO_x/ Si(111) und NIL-strukturierten SiO_2/Si(111) Substraten untersucht. Die Bestimmung des Ga Gehalts mittels XRD ergibt Werte zwischen 0 und 60 % in den unterschiedlichen Nanodrahtproben. Des Weiteren ergibt ein Vergleich der beiden Wachstumsstrategien signifikant kleinere Halbwertsbreiten der 2θ-XRD-peaks für NIL-strukturierte Substrate (0.031°) als für Nanodrähte, die selbstorganisiert gewachsen sind (0.084°). Diese Erkenntnis wird außerdem von Ramanspektroskopie unterstützt, die niedrigere longitudinal optische zu transversal optische (LO/TO) Intensitätsverhältnisse und kleinere LO-Halbwertsbreiten im Fall von NIL-strukturiertem Nanodrahtwachstum zeigen. Diese Beobachtungen weisen auf eine ausgezeichnete Zusammensetzungshomogenität im Fall von positioniertem Nanodrahtwachstum auf strukturierten Substraten hin. Zusätzlich zeigen Tieftemperatur-Photolumineszenzmessungen (PL) ein Bandlücken-Tuning im Wellenlängenbereich von $\sim$1800–2850 nm, wobei Halbwertsbreiten von $\sim$30 meV unabhängig vom Ga Gehalt gemessen wurden.

Schließlich wird die Auswirkung der Wachstumsparameter auf die Mikrostruktur mittels TEM und XRD untersucht. Dabei wird bei den mit verschiedenen As/In Verhältnissen gewachsenen InAs Nanodrähten eine ungeordnete Wurtzit (WZ) Struktur entdeckt, bei der alle paar Monolagen bis Nanometer Stapelfehler auftreten. Es wird jedoch beobachtet, dass die Wachstumstemperatur die Kristallstruktur auf eine stärkere Weise beeinflusst, so dass für höhere Temperaturen ($\geq$530 °C) phasenreine WZ Segmente mit einer Länge bis zu >10 nm entstehen können. Des Weiteren werden Ensembles von InAs Nanodrähten mit unterschiedlichen Durchmessern (40–135 nm) mit Photolumineszenzspektroskopie untersucht. Die Nanodrähte zeigen eine Rotverschiebung mit höherer Temperatur und eine Bandkantenenergie bei tiefer Temperatur von $\sim$0.41 eV im Fall der dicken Nanodrähte. In Übereinstimmung mit Simulationen hat eine Verringerung des Durchmessers eine auf Quantenconfinement zurückzuführende Blauverschiebung zur Folge.

Die gute Kontrolle über das In(Ga)As Nanodrahtwachstum auf Si und das erlangte Verständnis wichtiger physikalischer Eigenschaften liefert eine wertvolle Grundlage für die Herstellung von hochqualitativen nanodrahtbasierten Bauteilen.

Contents

Abstract i

Zusammenfassung iii

Introduction 1

1 Molecular beam epitaxy 7

1.1 The molecular beam epitaxy system . . . 8
1.2 Reflection high-energy electron diffraction . . . 12
1.3 Quadrupole mass spectrometry . . . 15

2 Self-assembled InAs nanowire growth 19

2.1 Substrate preparation and growth details . . . 20
2.2 Growth of self-assembled InAs nanowires on Si(111) . . . 22
2.2.1 Nanowire dimensions and directionality . . . 22
2.2.2 Growth parameter space for InAs nanowires . . . 24
2.2.3 In desorption and thermal decomposition measured by quadrupole mass spectrometry . . . 29
2.2.4 Effect of In and As fluxes on the nanowire growth rates . . . 37
2.3 Conclusion . . . 42

3 Growth mechanism of self-induced InAs nanowires 45

3.1 Self-induced nanowire growth – Growth mechanism . . . 46
3.1.1 Self-catalyzed nanowire growth . . . 46
3.1.2 Catalyst-free nanowire growth . . . 46
3.2 In-situ nucleation analysis by RHEED . . . 47
3.2.1 Self-induced InAs nanowire nucleation . . . 47
3.2.2 Comparison with self-induced GaAs nanowire nucleation . . . 51
3.3 Post-growth investigation of InAs nanowires . . . 53

3.3.1 SEM analysis 53
3.3.2 TEM analysis 55
3.4 Growth interruption experiments 56
3.5 Conclusion 57

4 Microstructure and optical properties of InAs nanowires 59
4.1 Structural properties of InAs nanowires 60
4.1.1 Transmission electron microscopy 62
4.1.2 High resolution X-ray diffraction 66
4.2 Photoluminescence spectroscopy of InAs nanowires 68
4.2.1 Experimental details 68
4.2.2 Temperature dependent PL measurements 69
4.2.3 Power dependent PL measurements 72
4.2.4 Effect of nanowire diameter 74
4.3 Conclusion 76

5 Positioned InAs nanowire growth 79
5.1 Substrate preparation for position-controlled nanowire growth 80
5.1.1 Small size patterned substrates by electron beam lithography 80
5.1.2 Large-scale patterned substrates by nanoimprint lithography 85
5.2 Positioned growth of InAs nanowires on Si(111) 87
5.2.1 Growth selectivity and vertical nanowire growth yield 87
5.2.2 Vertical directionality and crystal tilt 93
5.3 Nanowire growth kinetics 94
5.3.1 Pitch and growth time dependent nanowire size 94
5.3.2 Effect of the As flux on the nanowire growth rates and tapering 99
5.4 Conclusion 102

6 InGaAs nanowire growth and related optical properties 103
6.1 Growth of InGaAs nanowires on Si 104
6.2 X-ray diffraction of InGaAs nanowires 107
6.3 Optical analysis by Raman and PL spectroscopy 110
6.4 Conclusion 114

Conclusion and outlook 115

Appendix 119

A Fabrication of a Si stamp for nanoimprint lithography 119

B Manual 1: Substrate preparation 123
B.1 Substrate preparation for unordered nanowire growth 123
B.2 Substrate preparation for ordered nanowire growth 124

C Manual 2: Nanoimprint 127
C.1 Fabrication of a Si stamp for nanoimprint 127
C.2 Imprint the stamp on a silicon wafer 128

List of acronyms 129

List of Figures 131

List of Tables 133

Bibliography 135

List of publications 147

Conference contributions 149

Acknowledgments 151

Introduction

The first growth of nanowires dates back to 1964 when Wagner and Ellis reported on the novel vapor-liquid-solid growth mechanism [Wag64] for the growth of elongated crystals, named whiskers at that time. In particular, they grew silicon (Si) whiskers with diameters of 100 nm using liquid gold droplets as catalysts. In the following decades Wagner and Givargizov [Giv71, Giv75] were one among a few researchers active in this field, gaining not much attention by other groups. This changed rapidly in the ´90s when the first nanowire device based on light emitting p-n junction GaAs whiskers was fabricated [Hir95] and Wagner's pioneering work [Wag64] was taken as the basis for many scientific reports resulting in more than 3000 citations for Wagner and Ellis today.

Over the past decade semiconductor nanowires have been studied extensively due to their unique geometries and functional properties with heterostructures [Gud02, Lau02], that provide rich prospects for novel electronic and optoelectronic devices [Hua01, Hua04], solar cells [Kay05, Col09], thermoelectric devices [Zha98, Bou08], and biosensors [Zhe05]. In particular, the integration of III–V semiconductor nanowires directly onto Si platform has emerged as a promising route to combine the advantages of cost-effective, CMOS compatible Si technology with the outstanding electronic and optical properties of III–V semiconductors. In addition, nanowire growth benefits from alleviated lattice and thermal mismatch restrictions due to a small contact area to the growth substrate and a fast strain relaxation through the nanowire surface. This facilitates direct growth of III–V nanowires on Si offering the possibility of epitaxial, low-defect density III–V/Si heterojunctions with minimized misfit dislocations and antiphase boundaries [Cir09]. Such high quality III–V/Si heteroepitaxial growth is not easily feasible in conventional thin film epitaxy.

In this regard, InAs-based nanowires and related alloys are of particular interest due to a large number of unique material inherent properties of InAs and peculiar heterojunction properties with Si. InAs offers very small electron effective mass ($m^* \sim 0.023 m_0$) allowing very high electron mobilities (μ_e > 20000 cm^2/Vs at 300 K [Pol93]), high injection velocities, large excitonic g-factors, as well as surface Fermi level pinning which facilitates easy

formation of low-resistive Ohmic contacts. Combined with Si these features allow for very high current densities in e.g. tunnel-junction nanowire field-effect transistors due to steep source-channel p-n heterojunction between InAs and Si, exceeding those of other III–V/Si nanowire-based heterojunctions [Bjo10]. In addition, InAs can be alloyed with GaAs to enable wide direct band gap tuning from 0.36 eV to 1.42 eV (at 300 K), opening up several attractive nanowire photonic device applications. Recently, these unique features led to remarkable prototype nanowire devices such as broad band solar cells and photodetectors [Wei09], light emitting diodes [Chu11, Tom11], Esaki tunnel diodes [Bjo10], and high-performance nanowire-based field-effect transistors [Tan10].

Despite these excellent opportunities for device research, much of the growth and related growth modes that influence the physical properties of III–V semiconductor nanowires has remained an active subject of investigation and debate. To date, the majority of III–V semiconductor nanowires were grown via external catalysts [gold (Au), nickel (Ni), etc.] in the well-established VLS growth mode utilizing a variety of growth techniques, i.e., metal organic chemical vapor deposition (MOCVD) [Dua00, Day09], chemical beam epitaxy (CBE) [Per09, Erc09], molecular beam epitaxy (MBE) [Wu02, Gee07], etc. However, for certain material combinations foreign catalysts may lead to unintentional impurity incorporation within pure crystalline III–V nanowires, obscuring charge carrier profiles and limiting device applications [All08, Bre11]. In addition, gold is well known to introduce deep level traps in the semiconductor bandgap, limiting the performance of functional III–V-on-Si devices [Bro80, Wan06]. This triggered large efforts to investigate foreign catalyst-free growth schemes for III–V-based nanowires on Si.

In III–V based nanowire growth without foreign catalysts, most growth reports – except for nitride-based nanowires (GaN, AlN, InN and related alloys) [Cal07a, Cal07b, Che10, Urb11, Car11] – relied on a self-induced VLS growth mechanism governed by auto-catalytically formed droplets of the group-III element. Especially, in III–arsenide (As) based nanowires this self-catalyzed growth mode has become a favorable method for ready formation of nanowires with high growth rate on almost any substrate [Day07, Fon08a, Col08, Pli10, Man10, Bre11]. Significant understanding of nucleation mechanisms and nanowire size and morphology dependencies on growth parameters helped to establish universal growth models and growth phase diagrams. But still, substantial limitations associated with this droplet-assisted growth remained, i.e., non-abrupt doping and compositional profiles in axial nanowire hetero-interfaces [Pal08, Duf10], unintentional nanowire tapering and kinking [Col08, Pli10, Sch11], as well as mixture of vertical and inclined <111>-oriented nanowires on Si(111) [Ucc11]. Surpassing these limitations, relatively little attention has been paid so far to spontaneous growth of III–As based nanowires – especially by MBE – without

autocatalytic group-III element droplets.

Beyond investigation of nanowire growth and dimensions several characteristic nanowire properties are of great interest, such as crystal structure, electrical and optical properties. For III–As bulk materials the crystal structure is typically zincblende (ZB), which is constructed by two interpenetrating face-centered cubic lattices. In nanowires, however, an additional hexagonal wurtzite (WZ) structure is mostly observed. Today, a considerable amount of publications report on the control of crystal structure in III–As nanowires, mainly grown by MOCVD via Au catalysts on InAs(111)B or InAs(001) substrates. The crystal structure was found to be influenced by growth temperature and V/III-ratio [Dic10], growth interruption of the group-III precursor [Dic10, Bol11], nanowire diameter [Joh10, Bol11], and growth direction [Li11c].

In nanowire growth without foreign catalysts a few reports exist where self-catalyzed GaAs nanowires were grown by MBE on GaAs [Spi09] and Si [Kro10] substrates. The crystal structure was mainly controlled via the V/III-ratio and could be tuned between pure ZB and 70 % WZ content [Spi09]. However, under the absence of liquid droplets – when the nanowires do not grow via the VLS mechanism – control of crystal structure seems to be more difficult. Analysis of InAs nanowires grown by MOCVD on InAs, InP and GaAs substrates [Tom07a] as well as Si substrates [Tom08] are reported. In all cases uncontrolled ZB/WZ stacking faults (SF) taking place every 1–3 monolayers (ML) were observed regardless of the nanowire diameter. Good knowledge and control of the nanowire crystal structure is important for device application due to the influence on electrical and optical properties. For example, mixed crystal structures can lead to carrier scattering yielding lower free carrier mobilities compared to phase pure crystals [The11].

The effects of the crystal structure on the optical emission properties of InAs nanowires have remained heavily underexplored, due to well-known difficulties of photoluminescence (PL) spectroscopy in the infrared (IR) spectral region, i.e., poor detectivity of available detectors, atmospheric absorption, and competing non-radiative recombination processes [Fan90]. Only most recently, Sun et al. provided the first report of low-temperature PL spectroscopy on ensembles of Au-catalyzed InAs nanowires of both pure WZ and ZB crystal phase [Sun10]. But additional insights into the optical emission properties of binary InAs nanowires are much needed.

With respect to functional nanowire devices it is essential to have control over position, size, and directionality of the nanowires in order to allow their implementation into large-scale homogeneous arrays with predictive performance. To meet all these demands, there has been only a limited amount of success for III–As-based nanowires on Si, mainly via selective area epitaxy (SAE) using methods such as pulsed laser deposition, chemical

beam epitaxy, and metal organic chemical vapor deposition [Roe06, Bak04, Day09]. While these reports demonstrated good control of nanowire position, directionality and size, many of them relied on predefined gold-droplet nucleation sites and the growth kinetics were restricted to the VLS growth mechanism. But the growth of device-quality nanowires with high purity should abstain from the common nucleation scheme that employs foreign catalysts such as gold. In contrast, during non-catalytic growth methods – especially on Si substrates – control of preferential growth directionality was difficult to achieve due to the crucial polar/non-polar nature of the group-III–As/Si(111) heterointerface [Tom07b]. These problems have remained a central issue and many attempts have been tried to improve directionality in nanowire growth [Tom08, Ucc11].

In addition to position-controlled growth of nanowires, band gap tuning is essential in particular for optical nanowire devices such as photodetectors or solar cells. In III–As nanowire systems, during the recent five years a few groups worked on the growth and characterization of ternary $In_{1-x}Ga_xAs$ nanowires. But the number of reports are still rather limited, arising from the difficult growth of well-controlled and uniform InGaAs nanowires. Conventional VLS growth with foreign or self-catalysts produced InGaAs nanowires with severe inhomogeneities, evidenced by large composition gradients, undesired tapering, as well as limited group-III element incorporation efficiencies, independent of the applied growth method [Kim06, Reg07, Hei11]. Recent advances were achieved by catalyst-free growth methods, such as mask-free, self-assembled InGaAs nanowires or nanocones on Si [Che11, Shi11, Moe09], and selective area growth (SAG), primarily using metal organic chemical vapor deposition on InP and GaAs substrates [Sat08, Yos10, Koh12]. In the latter studies systematic analysis of nanowire aspect ratio dependencies on growth parameters was performed, although little information on composition homogeneity was provided. On the other hand, InGaAs nanowires on Si as reported so far (via self-assembly) still suffer from significant phase separation, exemplified by bowing of nanowires due to inhomogeneous strain and composition distribution along the nanowire axis and signatures of relatively broad PL and high resolution X-ray diffraction peak widths [Shi11].

The objective of this thesis is to gain knowledge and control over the growth of catalyst-free In(Ga)As nanowires on Si by MBE. This includes the exploration of substrate preparation, the nanowire growth window (temperature, In and As fluxes), the nanowire growth mechanism and position-controlled growth of In(Ga)As nanowires. Furthermore, in close collaboration with co-workers, basic properties of the nanowires such as crystal structure and optical properties should be elucidated.

These topics are addressed in six chapters structured as follows:

- **Chapter 1** gives an introduction to the MBE system used for nanowire growth as well as to the main growth monitoring techniques, namely line-of-sight quadrupole mass spectrometry and reflection high-energy electron diffraction.
- **Chapter 2** demonstrates self-assembled epitaxial InAs nanowire growth on Si(111) and presents the nanowire growth window with respect to temperature, In and As fluxes. Special investigation on the high temperature growth using quadrupole mass spectrometry reveals quantitative information of In desorption during growth.
- **Chapter 3** is dedicated to the InAs nanowire growth mechanism. The growth mechanism for InAs nanowires is investigated by utilizing a combination of *in-situ* reflection high-energy electron diffraction during nanowire nucleation and post-growth *ex-situ* scanning and transmission electron microscopy.
- **Chapter 4** shows investigations of the crystal structure of the as-grown InAs nanowires using high-resolution X-ray diffraction and transmission electron microscopy. Moreover, optical analysis by means of low temperature photoluminescence are performed on selected InAs nanowire samples and basic dependencies on temperature and excitation power elucidated.
- **Chapter 5** presents position-controlled nanowire growth using pre-patterned SiO_2 covered Si(111) substrates. First, the sample processing is reported in detail using either electron beam or nanoimprint lithography for patterning periodic holes in the silicon oxide mask layer serving as nucleation sites for the nanowires. Furthermore, the critical interplay between growth kinetics and nanowire dimensions is evaluated by analyzing growth time, temperature, flux and pitch dependencies.
- **Chapter 6** demonstrates the growth of InGaAs nanowires on Si utilizing substrates for self-assembled growth as well as large nanoimprinted substrates. The effects of different In/Ga ratios on the nanowire growth are studied, and the growth quality and the effective Ga content in the nanowires are investigated by high-resolution X-ray diffraction, energy-dispersive X-ray spectroscopy, Raman spectroscopy and photoluminescence spectroscopy.

1
Molecular beam epitaxy

In this chapter the main experimental growth technique molecular beam epitaxy (MBE) and associated methods such as *in-situ* reflection high-energy electron diffraction (RHEED) and quadrupole mass spectrometry (QMS) are discussed. First, an overview of the used solid-source III–V MBE presents details about the system design, pumping facilities, wafer mounting, and temperature and growth flux calibration. Moreover, the two powerful *in-situ* growth monitoring techniques (RHEED, QMS) are introduced where the basic working principles and capabilities are discussed. In particular, the unique design of QMS is described which is installed in direct line-of-sight to the sample surface to enable *in-situ* monitoring of the desorbing fluxes during growth. Parts of this chapter are published in Refs. [Rud11, Her12a].

1.1 The molecular beam epitaxy system

All growth experiments were performed in a solid-source Veeco Gen II molecular beam epitaxy (MBE) system equipped with three vacuum chambers, namely an entry chamber for wafer loading (loadlock), a preparation chamber for a first outgassing of the substrate (T ~300 ℃) and the main growth chamber. In Fig. 1.1a a photograph of the MBE system is depicted showing the main growth chamber on the left and the loadlock on the right. Several He-operated cryo pumps supported by a liquid N_2 flushed cryo shroud reduce residual gas species yielding an ultra-high vacuum (UHV) base pressure of $\sim 1.2 \times 10^{-11}$ mbar as measured by an ionization gauge. In addition, to guarantee a very high purity system, no metals beyond the group-III growth materials are used – especially Au is strictly avoided. These demands are in line with the ultra-high purity operation of this system which has led to remarkable results in the past such as electron mobilities exceeding 10×10^6 cm^2/Vs for a two dimensional electron gas (2 DEG) in a modulation doped GaAs/AlGaAs heterostructure. The system offers furthermore two powerful *in-situ* growth monitoring techniques, i.e., reflection high-energy electron diffraction (RHEED, see chapter 1.2) and a quadrupole mass spectrometer (QMS, see chapter 1.3) installed in direct line-of-sight to the wafer surface as illustrated in Fig. 1.1b.

The system is designed for 2-inch substrates (wafers), which are mounted on tantalum (Ta) holders placed on a sample holder located in the center of the growth chamber (see Fig. 1.1b). Typically, the wafers are bonded onto the Ta holder using a thin film of liquid Ga facilitating a homogeneous temperature distribution all over the substrate. However, this procedure – originally developed for GaAs substrates in the past – faced severe sticking issues when using Si wafers. Hence, the design of a fundamentally different principle for substrate mounting was mandatory. The technical details of the newly applied holders are depicted in three photographs in Fig. 1.2. The main difference compared to the standard holders is their ring-shape yielding two main improvements, i.e., a straightforward mounting system suitable for all kinds of 2-inch substrates and the avoidance of liquid metal films such as Ga guaranteeing a clean wafer backside with easy post-growth fabrication of desired device structures. Fig. 1.2a depicts the ringholder from the front side loaded with a Si wafer. The ringholder front exhibits a narrow edge holding the wafer in place. From the backside the wafer is fixed by a pyrolytic boron nitride (pBN) ring clamped into the ringholder under tension (b). Four coils located in proximity to the sample holder heat up the wafer directly via thermal radiation as opposed to Ga bonded wafers where the massive Ta holder supplies the heat via thermal conduction. Performing several group-III metal (Ga) adsorption experiments under different substrate temperatures (heating currents) one can investigate

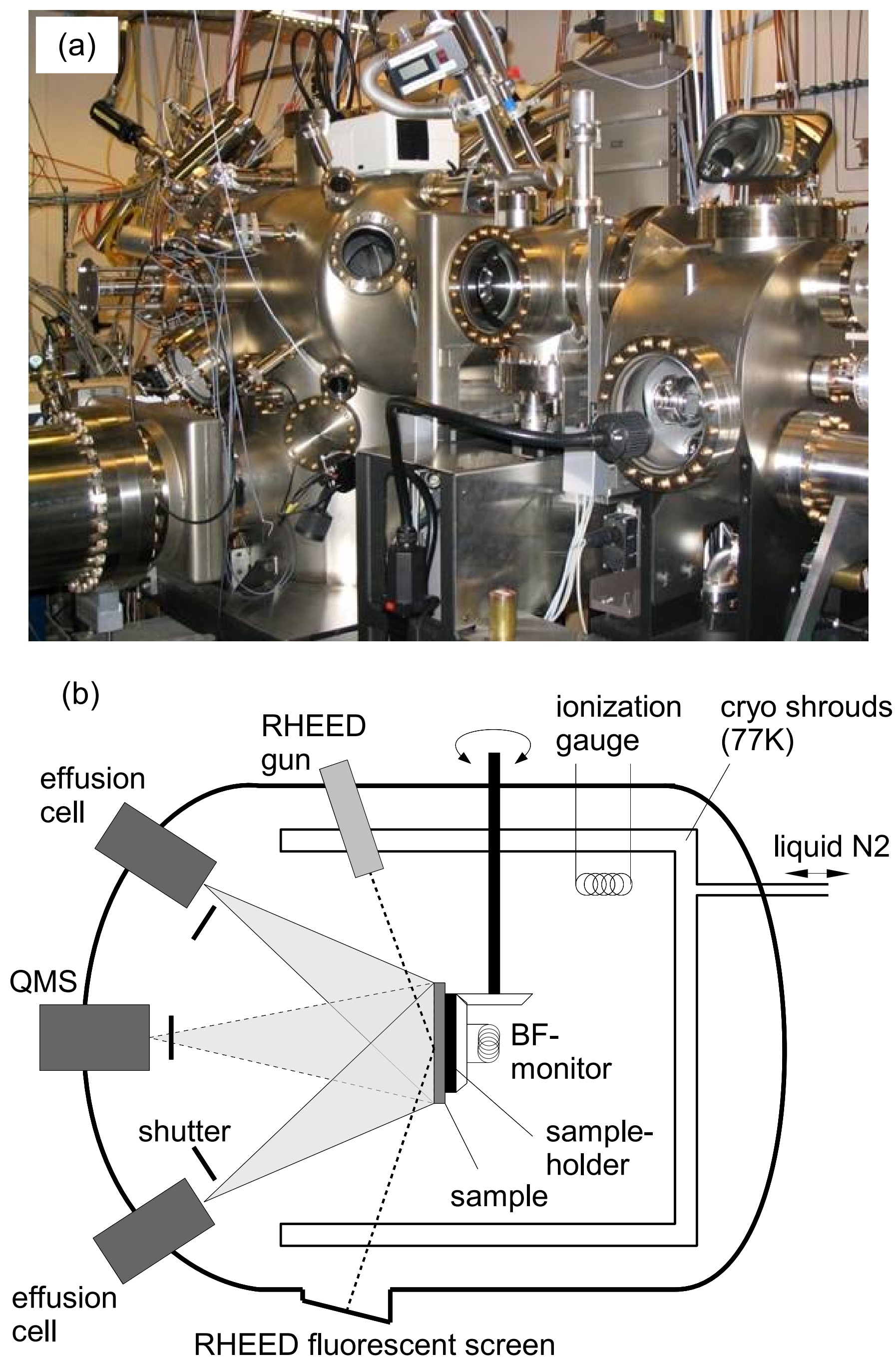

Figure 1.1. Photograph (a) and schematic (b) of the high-mobility Gen II MBE system (Veeco) at the Walter Schottky Institute which was used for all nanowire growths presented in this thesis. The schematic depicts solid-source effusion cells, ionization gauges, sample holder, line-of-sight quadrupole mass spectrometer (QMS) and reflection high-energy electron diffraction (RHEED) system. Liquid N_2 cryo shrouds and several He-operated cryo pumps (not shown) reduce the base pressure of the chamber to $\sim 1.2 \times 10^{-11}$ mbar. Schematic courtesy of Florian Herzog.

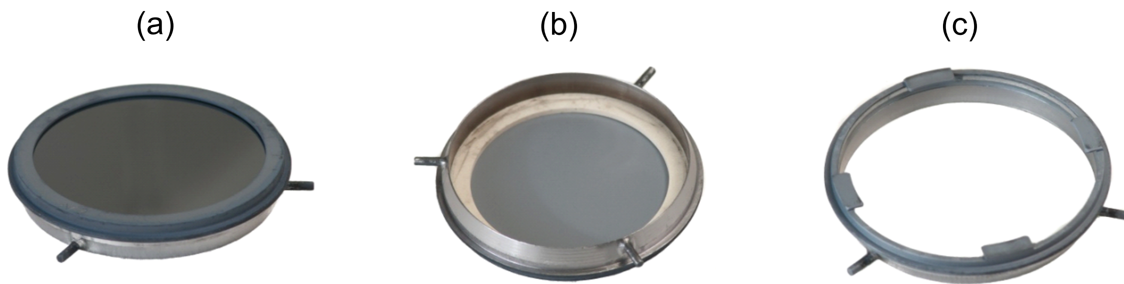

Figure 1.2. The photographs show two different types of the customized tantalum (Ta) substrate-ringholders designed for 2-inch wafers. In (a) and (b) the ringholder type I is depicted with loaded wafer in front and back view, respectively. A pBN ring is clamped in the Ta holder to fix the wafer (b). While this ringholder blocks the incident RHEED electron beam, a modified type of holder (type II) was fabricated where the Ta edge at the holder front was reduced to four distinctive points (c) facilitating *in-situ* RHEED measurements for most angles of incident electrons.

the temperature uniformity of the new ring holder mounting scheme. In detail, supplying a fixed Ga flux for a certain time to the substrate surface (Si) near the boundary conditions where Ga forms large macroscopic droplets, it is possible to map out the temperature profile across the entire wafer area since the formation of Ga droplets is a thermally activated process. Observing how the onset for droplet formation shifts with temperature across the wafer, the temperature uniformity was found to be $\Delta T \sim$15 °C – nearly as good as for Ga-bonded wafers with $\Delta T \sim$10 °C. Furthermore, it has to be mentioned that the Ta edge at the ringholder front end blocks the electron beam, completely inhibiting any RHEED measurements. A slightly modified ringholder (c) where the Ta edge was reduced to four distinctive points and where the wafer now rests on, was found to restore access to the RHEED signal for most angles of incidence.

The substrate temperature is measured twofold, via a tungsten/rhenium (W/Re) thermo couple located at the backside of the wafer close to the four heating coils and by an optical pyrometer facing the center part of the wafer surface. The given growth temperature for all experiments in this thesis always refers to the measurement via optical pyrometer since this temperature gives the actual wafer surface temperature which determines important nanowire growth kinetics. The used Ircon *Modline Plus* pyrometer operates within a spectral range of 910–970 nm and is calibrated to the onset temperature of native oxide desorption from a (001) GaAs wafer surface yielding an emissivity correction of ϵ = 0.3. Furthermore, at maximum heating power (35 V/5.5 A) the temperature on the wafer surface reaches

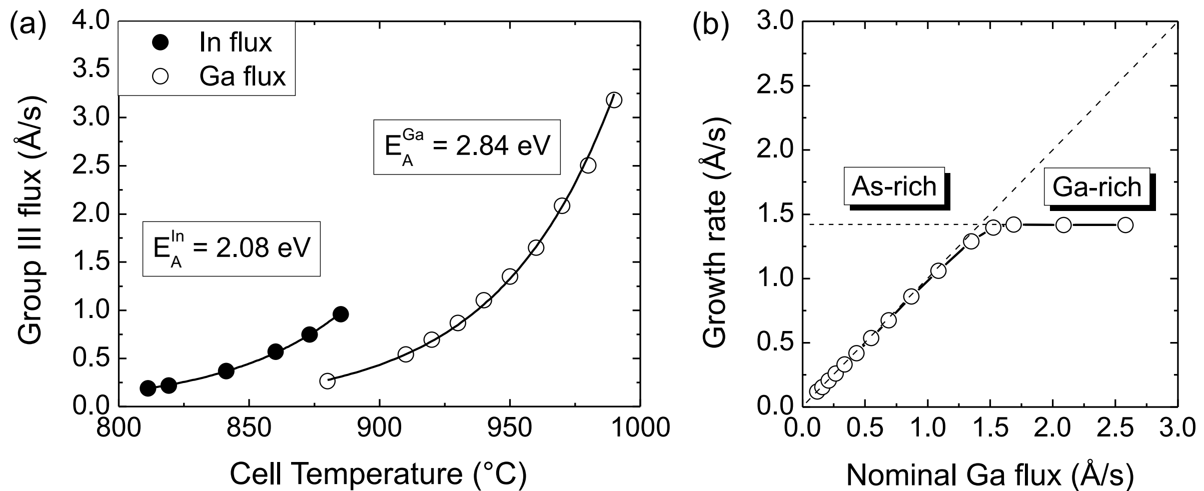

Figure 1.3. (a) In (black circles) and Ga (open circles) 2D equivalent growth rates measured by RHEED oscillations are plotted in dependence of cell temperature revealing a typical exponential behavior. A best fit to the curves is taken to allow flux calibration for any cell temperature for both In and Ga fluxes. (b) 2D GaAs growth rate on GaAs(111)B substrate for fixed As_4-BEP of 2.6×10^{-6} mbar in dependence of the supplied Ga flux. From the As-rich to Ga-rich transition point we derived the equivalent two dimensional (2D) As flux rate, amounting to $\sim$1.41 Å/s for the given As_4-BEP of 2.6×10^{-6} mbar. Published in Ref. [Rud11].

$\sim$730 ℃ on ringholders, significantly higher than the $\sim$650 ℃ limit for the Ga-bonded case.

Moreover, the MBE is equipped with 16–24 cm^3 single filament Knudsen effusion cells (Veeco) for group-III elements (Al, Ga, In), a carbon and silicon source for p- and n-type doping, and a 2500 g Veeco valve cracker cell supplying uncracked arsenic (As_4). For all experiments As_4 was not cracked with typical cell temperatures of 330–360 ℃. The cell shutters are computer-operated allowing automated and accurate growth of sophisticated 2D quantum wells or nanowire heterostructures. To access a quantitative description of the underlying growth kinetics during III–As nanowire growth, appropriate calibration of the employed fluxes is mandatory. The impinging group-III (In, Ga) fluxes are calibrated by recording RHEED intensity oscillations (see section 1.2 for details) during 2D layer deposition under As-rich environment, where the growth rate (units of Å/s) is limited by the active group-III flux. Representative flux measurements are depicted in Fig. 1.3a where the In (black circles) and Ga (open circles) flux – as measured by RHEED – are plotted in dependence of cell temperature. The graph clearly reveals the expected exponential behavior, which can be fitted to derive the desired In or Ga fluxes for any given cell temperature. Furthermore, from Arrhenius plots (not shown) activation energies for thermal

evaporation of In and Ga were determined to 2.08 eV and 2.84 eV, respectively, and matched with the exponential temperature dependence of the group-III flux.

The As flux, on the other hand, is usually given in units of beam equivalent pressure (BEP) of uncracked As_4 molecules as measured by an ionization gauge installed at the backside of the substrate holder (marked as *BF-monitor* in Fig. 1.1b). This makes a direct assessment of the actual As flux (in units of growth rate) and the active As/In or As/Ga flux ratio at the growth surface difficult. Hence, we used a similar method as for group-III flux calibration and determined the As fluxes in units of equivalent (2D) growth rate using RHEED oscillations for both Ga- and As-limited GaAs growths on GaAs(111)B surfaces. The experiment was performed by varying the Ga flux under fixed As_4-BEP (in mbar) consecutively from low Ga fluxes (heavily As-rich conditions) to high Ga fluxes (slightly Ga-rich conditions) at constant substrate temperature of $\sim$580 °C. This experiment was also performed for a series of different As_4-BEP. Results of one particular experiment at fixed As_4-BEP of 2.6×10^{-6} mbar are exemplified in Fig. 1.3b. Increasing the Ga flux yields an expected linear increase in growth rate, as far as As-rich conditions are maintained. However, beyond a critical Ga flux the growth rate saturates, indicating a transition to Ga-rich conditions, where the growth rate is limited by the active As flux. Here, only few RHEED oscillations could be observed until the intensity contrast was damped due to the shadowing effect of accumulated Ga droplets. From the transition point to saturation we derived the equivalent 2D As flux rate, amounting to $\sim$1.41 Å/s for the given As_4-BEP of 2.6×10^{-6} mbar. The entire series of various As fluxes revealed a linear behavior between As_4-BEP and 2D As rate. It has to be mentioned that this calibration was furthermore converted to the 7.1 % higher lattice constant of InAs with respect to GaAs yielding $\sim$1.51 Å/s for the given As_4-BEP of 2.6×10^{-6} mbar in terms of As-limited InAs(111) growth rate. Comparison of these rates with the nanowire growth rate allows a quantitative description of the rate-limiting fluxes and effective V/III ratios at the nanowire growth front as discussed in chapter 2.

1.2 Reflection high-energy electron diffraction

Reflection high-energy electron diffraction (RHEED) is a very powerful *in-situ* technique to analyze crystalline materials. This surface sensitive method is well known from thin film MBE growth where it is commonly used to determine growth rates and strain relaxation in heteroepitaxial systems and investigate the overall growth and morphological quality. The basic principle of RHEED is electron scattering at crystalline surfaces where high-energy electrons are diffracted according to kinematic and dynamic diffraction theories. Technically,

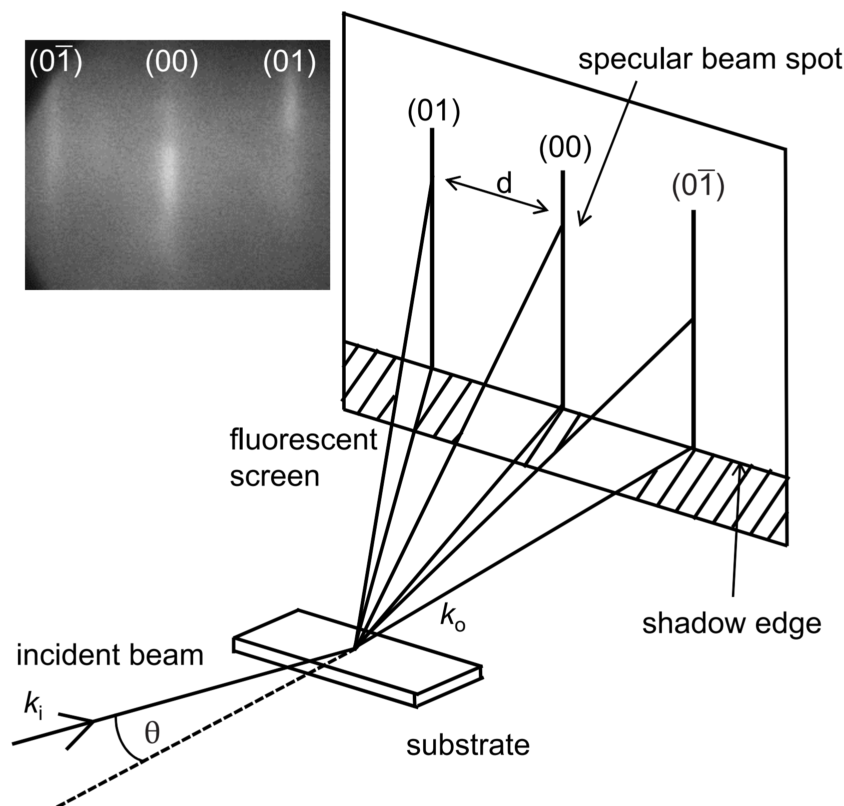

Figure 1.4. Schematic of the basic principle of *in-situ* RHEED measurements. The electron beam strikes the wafer surface under a very flat angle (θ = 1–3°) during MBE growth. The diffracted beam is then visualized on a fluorescent screen. As an inset a photograph of the Si(111) diffraction pattern is presented exhibiting typical zeroth and first order streaks. Adapted from [Her96, Kob04a].

an electron gun is installed in the MBE chamber under a very flat angle θ to the wafer surface such that the electron beam strikes the wafer and subsequently hits a fluorescent (phosphorus) screen on the other side of the chamber (see Fig. 1.1b). The electron beam – generated by an electron gun typically operated at $\sim$1.5 A current and 15 kV acceleration voltage – is focused on the wafer surface via a complex interplay of magnetic and electric fields. Fig. 1.4 illustrates a crystalline wafer which scatters incident electrons due to the wavelike character of the substrate atoms, generating a diffraction pattern on the fluorescent screen. Bright spots or streaks are observed wherever the change between incident ($\vec{k}_\text{i}$) and outgoing ($\vec{k}_\text{o}$) electron wave vector equals the reciprocal lattice vector $\vec{G}$ according to Ewald sphere construction [Her96]. For 2D surfaces such as a polished wafer surface this well-known so-called Laue equation

$$\Delta\vec{k} = \vec{k}_\text{o} - \vec{k}_\text{i} = \vec{G}$$

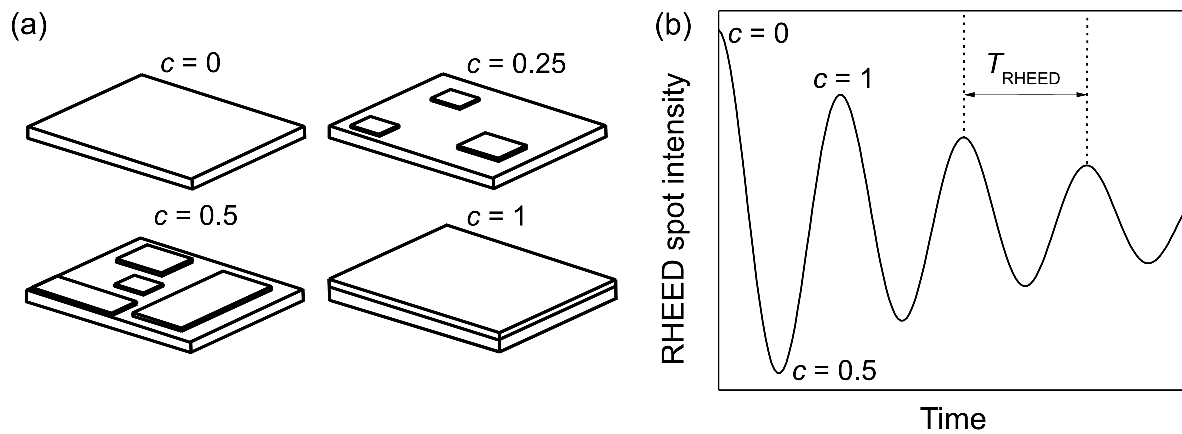

Figure 1.5. (a) Illustration of 2D layer formation during MBE growth for different fractional layer coverage *c* of 0, 25, 50 and 100 % and according intensity of the specular RHEED spot (b). The well-known RHEED oscillation is observed with full intensity for complete layers and minimum intensity for maximum disorder in the case of 50 % fractional layer coverage. The duration between two peaks (T_{RHEED}) represents thus the growth time for one monolayer.

predicts bright streaks as diffraction pattern. An example is given in the inset of Fig. 1.4 showing a RHEED image of the diffraction pattern of a Si(111) wafer covered with a $\sim$2 nm thin SiO_x layer prior to nanowire growth. Three streaks are clearly visible which – according to the adjacent schematic – can be referred to the zeroth (middle) and first order (two outer streaks) diffraction.

In this thesis the RHEED technique was mainly used to gain detailed information about Bragg spot intensity evolution and lattice relaxation time scales during InAs nanowire nucleation on Si. These results allowed *in-situ* investigation of the growth mechanism (as reported in chapter 3) by utilizing the reciprocal dependence of the RHEED streak separation on the lattice constant during crystal growth. When three dimensional (3D) islands grow on the wafer – as it is the case at the onset of InAs nanowire growth – the streaky pattern is superimposed by distinct spots and their separation (i.e., lattice constant) adapts to the lattice constant of InAs (for more details see section 3.2.1). Continuous movies with a time resolution of 0.3 s of the respective diffraction patterns were recorded and analyzed via a kSA 400 camera system (k-space Associates) for straightforward time-resolved evaluation of the 2D Si(111)–3D InAs transition.

We furthermore calibrated the Ga and In fluxes in terms of 2D equivalent GaAs and InAs growth rates by RHEED oscillation measurements as discussed in section 1.1. This is achieved by recording the intensity of the specular RHEED spot as a function of time during MBE deposition of 2D InAs or GaAs layers as illustrated in Fig. 1.5. An intensity

oscillation is observed with high intensities when a full monolayer (ML) is completed – due to a maximum degree of order. Partly completed MLs exhibit a disordered surface with mono atomic steps obscuring the RHEED signal [Nea83]. For all experiments the electron beam is focused on the substrate prior to growth and remains unmodified during growth. Hence, the electron beam gets out of focus the more layers are grown resulting in an overall decrease in RHEED intensity, i.e., damping (see Fig. 1.5b). The growth rate r can be calculated by determining T_{RHEED} – the duration for the formation of one ML – with respect to the thickness of one ML (d) via

$$r = \frac{d}{T_{\text{RHEED}}}.$$

Typical growth rates for Ga and In fluxes used in this study were 0.2–0.9 Å/s, which are much lower than in conventional thin film growth.

1.3 Quadrupole mass spectrometry

To acquire fundamental knowledge of the surface kinetic and thermal dissociation processes, quadrupole mass spectrometry (QMS) was used as a novel *in-situ* method to quantitatively determine the desorbing species during III–As nanowire growth. Technically, this method was realized – as reported by G. Koblmüller in Ref. [Kob04a] – by selecting a specific geometrical configuration between sample surface and mass spectrometer, such that the ionizer of the mass spectrometer is directed in line-of-sight to the sample wafer (see Fig. 1.6a). We used a conventional state-of-the-art quadrupole mass spectrometer (*Process Eye Professional* operated *Spectra Microvision Plus* from MKS Instruments) installed on a flange designated for beam sources and collimated with an appropriate aperture. This aperture restricts the acceptance angle to the desorbing species originating merely from the center area of the sample wafer, completely suppressing any background signals from substrate manipulator or chamber walls. However, collimation reduced the signal strength relative to background and shot noise, but elaborate geometrical work on QMS-to-sample distance and aperture plate design was performed to optimize probing conditions. Detection of ions in a mass range of 1 to 300 atomic mass units (amu) with a resolution better than 0.5 amu (at 10 % peak height) is achieved with this mass spectrometer. This QMS is also equipped with a dynode electron multiplier, enabling partial pressures to be detected as low as 1×10^{-14} mbar with a time resolution of 2 s.

In the case of InAs nanowire growth, the desorbing species of main interest are the Indium isotope ^{115}In and Arsenic ^{75}As. To provide a direct measure for the amount of desorbing ^{115}In and ^{75}As in more convenient units of desorption rate, the QMS-measured

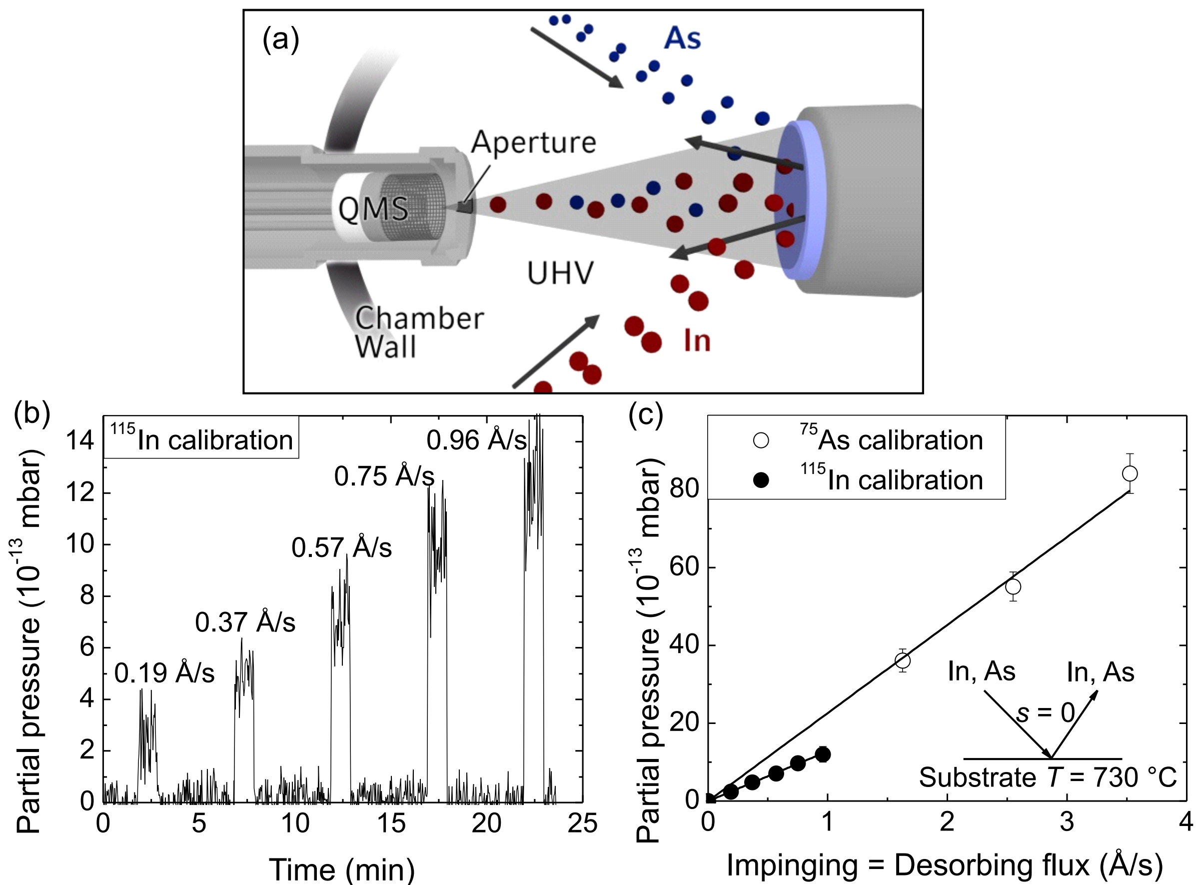

Figure 1.6. (a) Schematic of the experimental setup for quantitative *in-situ* line-of-sight QMS. Important features are shown, such as ion gauge and aperture which restricts desorption measurements to a small (∼1-inch wide) area of the wafer center region. The QMS calibration is performed at 730 °C substrate temperature where the sticking coefficient (*s*) of In and As on SiO_x/Si(111) is zero, i.e., all impinging fluxes desorb completely – thus they can be set equal. For calibration the QMS partial pressure is plotted as a function of time (b) while a sequence of incident fluxes is applied (here exemplified for the ^{115}In case). This determines a linear relation between QMS partial pressure and 2D equivalent growth rate, which is shown in (c) for ^{75}As and ^{115}In. Published in Ref. [Her12a].

partial pressure should be given in actual 2D equivalent growth rate units. Thus, direct comparison with the incoming fluxes can be facilitated, as these are well calibrated by RHEED growth rate oscillations. As demonstrated in Refs. [Kob04a, Kob04b] for GaN MBE growth, such direct mass balancing of the incoming and desorbing fluxes allows further quantification of the most important surface kinetic processes, such as incorporation, thermal decomposition (adatom detachment) and associated desorption rates and helps to monitor growth at any stage.

To achieve this, a sequence of well-known In and As fluxes was directed to a SiO_x/Si(111)

substrate kept at such high temperature (T = 730 °C) that the total supplied flux desorbed completely from the surface. In measuring the partial pressure signal for each individual impinging flux (Fig. 1.6b), an expected linear relationship between impinging (desorbing) flux and as-measured partial pressure was found (Fig. 1.6c). From the linear relationship one can derive proportionality constants for both ^{115}In desorption ($\sim$1.27$\times$10^{-12} mbar/Å/s) and ^{75}As desorption ($\sim$2.26$\times$10^{-12} mbar/Å/s). These proportionality constants are used to convert as-measured partial pressures to desorbing flux rates (units of Å/s) for all experiments performed in this work.

2

Self-assembled InAs nanowire growth

In this chapter the MBE growth of self-induced, catalyst-free (i.e., Au-free) InAs nanowires on Si(111) is presented. Here, growth is performed in a self-assembled (unordered) manner using a thin granular SiO_x mask to provide nucleation sites for the nanowires. First, basic investigations of the as-grown nanowires by means of scanning electron microscopy, transmission electron microscopy and X-ray diffraction will be shown emphasizing their vertical, i.e., epitaxial relationship with the underlying Si substrate. Furthermore, the entire growth parameter space regarding temperature, In and As fluxes will be elucidated and limitations of successful nanowire growth discussed. Based on fully quantitative *in-situ* line-of-sight quadrupole mass spectrometry, also the rate limiting factors in high-temperature InAs nanowire growth are determined by direct monitoring the critical desorption and thermal decomposition processes of InAs nanowires. In addition, closer investigation of the group-III and group-V flux dependencies on growth rate will be conducted and two apparent growth regimes derived, an As-rich and an In-rich regime defined by the effective As/In flux ratio. The results presented in this chapter are published in Refs. [Kob10, Her12a].

2.1 Substrate preparation and growth details

The substrates used for the growth of InAs nanowires were commercially available single-side polished 2-inch Si(111) wafers (on axis orientation $\pm$ 1°) grown by Czochralski (CZ) technique. If not otherwise specified the $\sim$275 µm-thick wafers were p-type doped with boron doping concentrations in the 10^{16} cm^{-3} range (resistivity 1–30 Ωcm). In a first preparation step $\sim$30 nm of SiO_x was sputter-deposited on the wafer surface using a radio frequency (rf) sputter-deposition chamber (Materials Research Corporation *8620* system). Subsequently, the wafer was etched in a Honeywell aqueous hydrogen fluoride (HF) solution to a final thickness of 2–5 nm as measured by standard ellipsometry technique. To get rid of all etching remnants after HF etching the wafers were cleaned in deionized water followed by a dip in isopropanol and a final nitrogen blow drying. The HF etching of the granular SiO_x mask layer opened nanometer size pinholes which serve as nucleation sites for the nanowires. For a better understanding of this process three atomic force microscopy (AFM) images and according schematics are depicted in Fig. 2.1. In (a) the bare Si(111) wafer is shown as covered with very smooth, (i.e., low roughness) native oxide. After sputter-deposition of 30-nm-thick SiO_x the AFM image exhibits a granular surface (b). HF etching of the oxide to a final thickness of 2–5 nm opens pinholes [black suppressions in (c)] exposing the underlying Si substrate. The pinholes are anticipated to serve as nucleation sites for InAs since the sticking coefficient of In adatoms on Si(111) is much higher than on SiO_x. It will be later shown that the nanowire density is lower than the pinhole density meaning that not all pinholes lead to nanowire formation. Furthermore, it has to be mentioned that this scheme is very similar to previously reported substrate preparation for self-catalyzed GaAs nanowire growth on SiO_x masked GaAs(111)B substrates [Fon08a]. A detailed step-by-step manual reporting all critical parameters of the substrate preparation for self-assembled nanowire growth is given in appendix B.1.

After HF etching the wafer surface remains hydrogen terminated preventing re-oxidation for a few hours even when exposed to air. Subsequently, the wafers were directly (within less than 30 min) loaded into the UHV environment of the MBE system. Before transferring the wafer into the final growth chamber it was slightly annealed at $\sim$300 °C for at least 1 hour. Prior to growth the SiO_x-covered Si(111) wafer was further annealed in the growth chamber at higher temperatures (T = 730 °C) for 15 min to remove residual contaminants. Subsequent InAs nanowire growth was performed after cool-down to the desired substrate temperature. Nanowire growth was initiated by first opening the valve of the As source for a few minutes before subsequent opening of the In cell starts the nanowire growth. This two step procedure ensures a balanced As flux guaranteeing reproducible growth experiments.

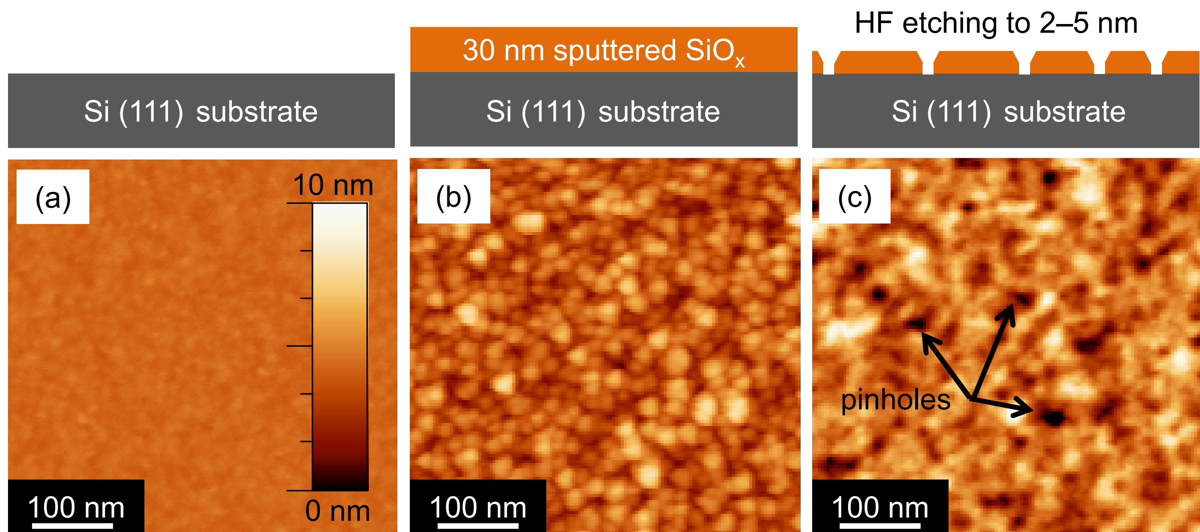

Figure 2.1. AFM images of (a) a Si(111) wafer surface and (b) after rf sputter-deposition of ∼30 nm SiO_x. (c) HF etching to a final thickness of 2–5 nm opens pinholes in the grainy SiO_x layer visible as black suppressions in the AFM micrograph. A certain amount of these pinholes reach the underlying Si substrate and serve as nucleation sites for the nanowires.

Note that at typical growth temperatures (> 380 °C) the supplied As desorbs completely, thus the substrate surface remains free of any residual As-rich layer prior to growth. After growth the In shutter was closed and the temperature was quenched immediately while – if not otherwise specified – the As shutter was kept open during cool down.

For the growth series investigated here, substrate temperatures between 380 °C and 600 °C were employed, In flux rates (2D equivalent growth rates) between 0.24 Å/s and 0.90 Å/s and As_4 beam equivalent pressures (BEPs) between 2.6×10^{-6} mbar and 5.0×10^{-5} mbar. For direct comparison, the As_4 BEPs were further calibrated in terms of As-limited 2D growth rate on GaAs(111)B surfaces via RHEED intensity oscillations, yielding growth rates ranging from 1.51 Å/s to 29.04 Å/s, respectively (see section 1.1 for calibration details). This allows direct determination of the active V/III flux ratio as supplied to the substrate surface. After growth scanning electron microscopy (SEM) was performed on small $\sim1\times1$ cm^2 samples cleaved from the very center of the 2-inch wafer to guarantee data analysis un-obscured by temperature fluctuations across the wafer surface and to allow comparison of morphological data from individual growth runs.

2.2 Growth of self-assembled InAs nanowires on Si(111)

2.2.1 Nanowire dimensions and directionality

To demonstrate how catalyst-free InAs nanowires grow on the as-prepared SiO_x/Si(111) substrates, an exemplary growth is shown in Fig. 2.2 for a growth temperature of 460 ℃, a fixed In flux of 0.24 Å/s, As beam equivalent pressure (BEP) of 2.6×10^{-6} mbar (1.51 Å/s) and growth time of 45 min. The SEM image of Fig. 2.2 shows that the InAs nanowires exhibit predominant vertical directionality related to the $\{111\}$-family of orientations, indicating direct relationship to the underlying Si(111) substrate. Occasionally, individual nanowires were identified to be slightly tilted (< 10°) against the vertical [111]-direction. Furthermore, all nanowires are fairly straight (i.e., non-tapered) with hexagon-shaped geometries as can be seen in the two insets of Fig. 2.2 showing magnified images of single nanowires in tilted and top-view configuration. According to recent observations of [111]-oriented group-III–As-based nanowires with hexagonal geometry, their six sidewall facets are expected to correspond to the $\{110\}$-family of orientations [Zar09]. Furthermore, the length (L) and diameter (D) as determined by SEM yield L = 726 nm $\pm$ 39 nm and D = 51 nm $\pm$ 4 nm (averaged for 10 nanowires). Top-view SEM imaging of a larger area (not shown) yielded furthermore an InAs nanowire density in the range of 2×10^9 cm^{-2} ($\widehat{=}$ 20 μm^{-2}) for the applied growth conditions.

Moreover, the magnified SEM micrograph in Fig. 2.2 shows that the nanowire tip does not exhibit any In droplet indicating a growth mechanism that may differ from the common vapor-liquid-solid (VLS) growth observed for semiconducting nanowires. Extensive *in-situ* RHEED studies in combination with *ex-situ* SEM and TEM analysis were performed to explain the apparently droplet-free growth mode for self-induced MBE-grown InAs nanowires. All details on these experiments will be given in chapter 3.

To confirm the structural quality between the InAs nanowires and the Si(111) substrate out-of-plane symmetric X-ray diffraction (XRD) 2θ–ω scans in a Philips *Xpert MRD* diffractometer were performed on the same InAs nanowire sample. As shown in Fig. 2.3a, only two characteristic peaks were identified over a wide 2θ range (0–50 deg), with their positions corresponding to InAs at 25.4° and Si(111) at 28.4°. This demonstrates the direct epitaxial relationship between the InAs nanowires and the Si(111) substrate. It has to be mentioned that a precise attribution of the InAs peak to the dominant crystal structure, either a hexagonal (wurtzite) InAs structure [h(002): 2θ = 25.36°] or to a cubic (zincblende) InAs structure [c(111): 2θ = 25.44°] demand higher resolution as presented in the current scan.

More insights into the nucleation of InAs nanowires were provided by TEM analysis (Fig. 2.3b) using a FEI *Tecnai FEG* microscope operated at 200 kV. The bright-field high-

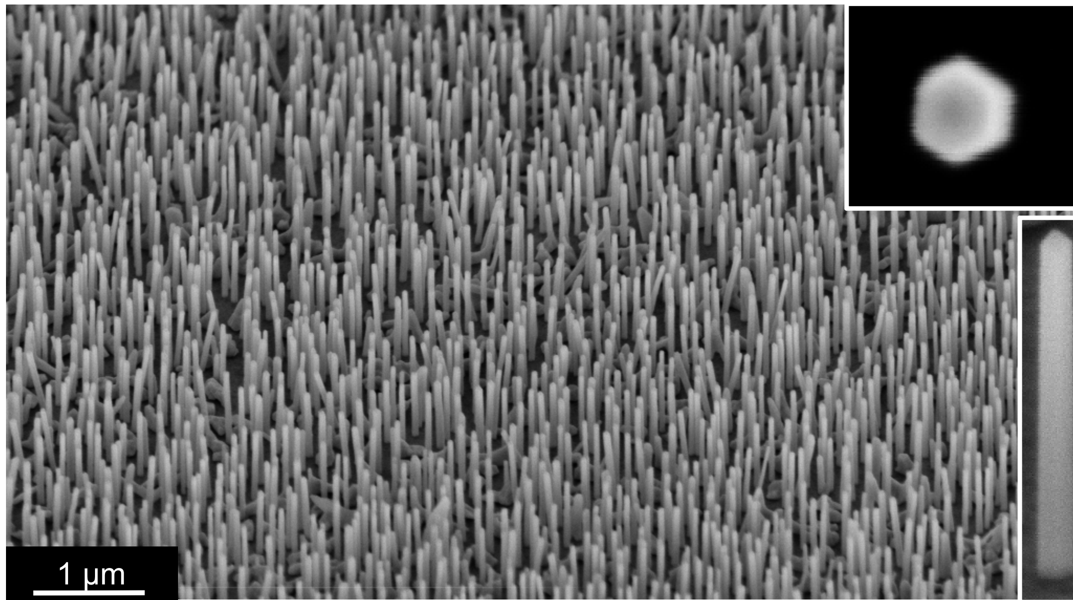

Figure 2.2. Scanning electron micrograph of vertically aligned InAs nanowires grown on Si(111) at a temperature of 460 ℃. The magnified area and top-view image show the nanowire/substrate interface and hexagonal geometry, respectively.

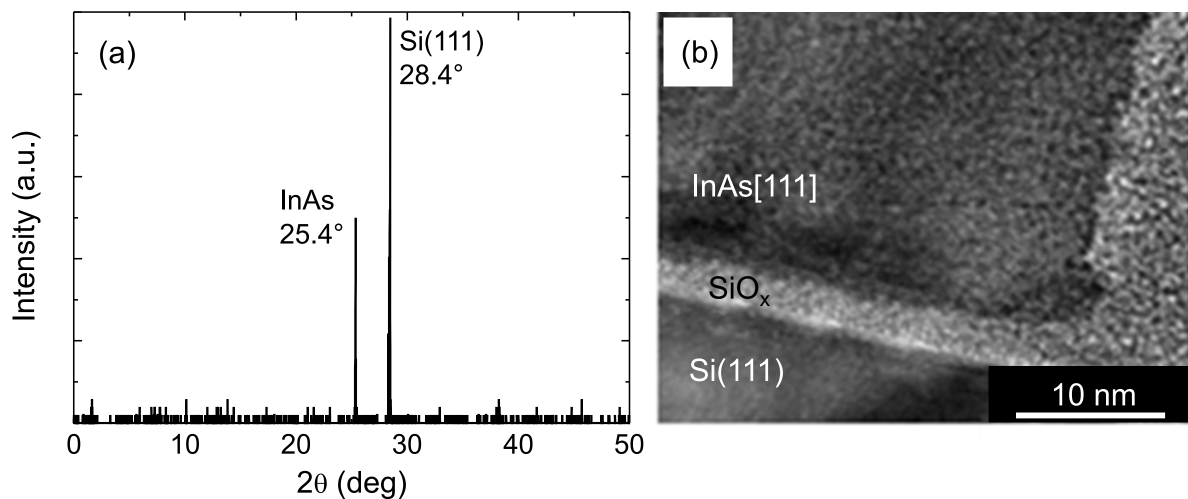

Figure 2.3. (a) X-ray diffraction 2θ–ω scan of representative InAs nanowire sample (grown at 460 ℃) illustrating two peaks associated with InAs (25.4°) and the Si(111) substrate (28.4°). (b) Cross-section TEM image of a typical InAs nanowire nucleated on Si(111) (460 ℃ sample) presented with high magnification focused at the bottom nanowire/substrate interface. The nanowires nucleate at pinholes in the SiO_x layer located close to the center region of the nanowires. TEM image courtesy of J.-P. Zhang, Suzhou Institute of Nano-Tech and Nano-Bionics. Published in Ref. [Kob10].

magnification TEM image in Fig. 2.3b shows the interface between the Si(111) substrate and a representative InAs nanowire (sample grown at 460 ℃), evidencing nucleation of the InAs nanowire at the amorphous ∼3-nm-thick SiO_x mask layer. The original nucleation site of the nanowire is anticipated within the pinhole in the SiO_x layer which is typically located in the center region of the nanowires (left of the visible part of the image) – similar to previous reports on GaAs nanowires grown on SiO_x-masked GaAs substrates prepared by the same method [Fon08a]. During growth the nanowire dimensions increase in axial and radial direction resulting in an overgrowth of the pinhole.

More structural data based on TEM and high-resolution XRD (HRXRD) of InAs nanowires will be presented in chapter 4 for precise crystal structure investigation.

2.2.2 Growth parameter space for InAs nanowires

To gain further knowledge about InAs nanowire growth the entire growth parameter space is studied here by variation of the active V/III ratio and growth temperature (T) over a large range. Otherwise, growth conditions were kept constant, i.e., fixed growth time of 45 min (for *V/III* = 6.3) and 24 min (for *V/III* = 36.3 and 56.5). Representative SEM micrographs of InAs nanowires grown within this V/III ratio and temperature series are depicted in Fig. 2.4. The micrographs of Figs. 2.4a–d show InAs nanowires grown at T = 410 ℃, 470 ℃, 490 ℃ and 530 ℃ under a V/III ratio of 36.3 (In = 0.24 Å/s, As = 8.71 Å/s), while samples in Figs. 2.4e and 2.4f were grown at 540 ℃ and 570 ℃ under higher V/III ratio of 56.5 (In = 0.36 Å/s, As = 20.33 Å/s). All micrographs reveal vertically aligned InAs nanowires (i.e., along the [111]-direction) with a non-tapered morphology and hexagonal cross-section with $\{110\}$ side facets as was already observed in section 2.2.1.

The SEM micrographs presented in Fig. 2.4 exhibit further a strong variation of nanowire length, diameter and density with applied growth conditions. For the lowest temperature of 410 ℃ (Fig. 2.4a) the formation of large clusters dominated the growth and as shown in Fig. 2.4g the average nanowire (NW) density was rather low (∼0.7 NWs/µm^2). By increasing the temperature to 470 ℃ and 490 ℃ (Figs. 2.4b, c) cluster formation was gradually reduced due to increased In adatom diffusion on the silicon oxide layer and much longer nanowires with a higher density (∼22.1 and 10.7 NWs/µm^2) were obtained. By applying even higher temperatures of 530 ℃ (Fig. 2.4d) shorter and thicker nanowires were produced with decreased average density (∼0.7 NWs/µm^2). The growth of clusters was significantly suppressed for these higher temperatures resulting in an almost InAs-free SiO_x surface between the nanowires. On the other hand, nanowires grown with higher V/III ratio showed the same non-tapered geometry, however, much higher growth temperatures

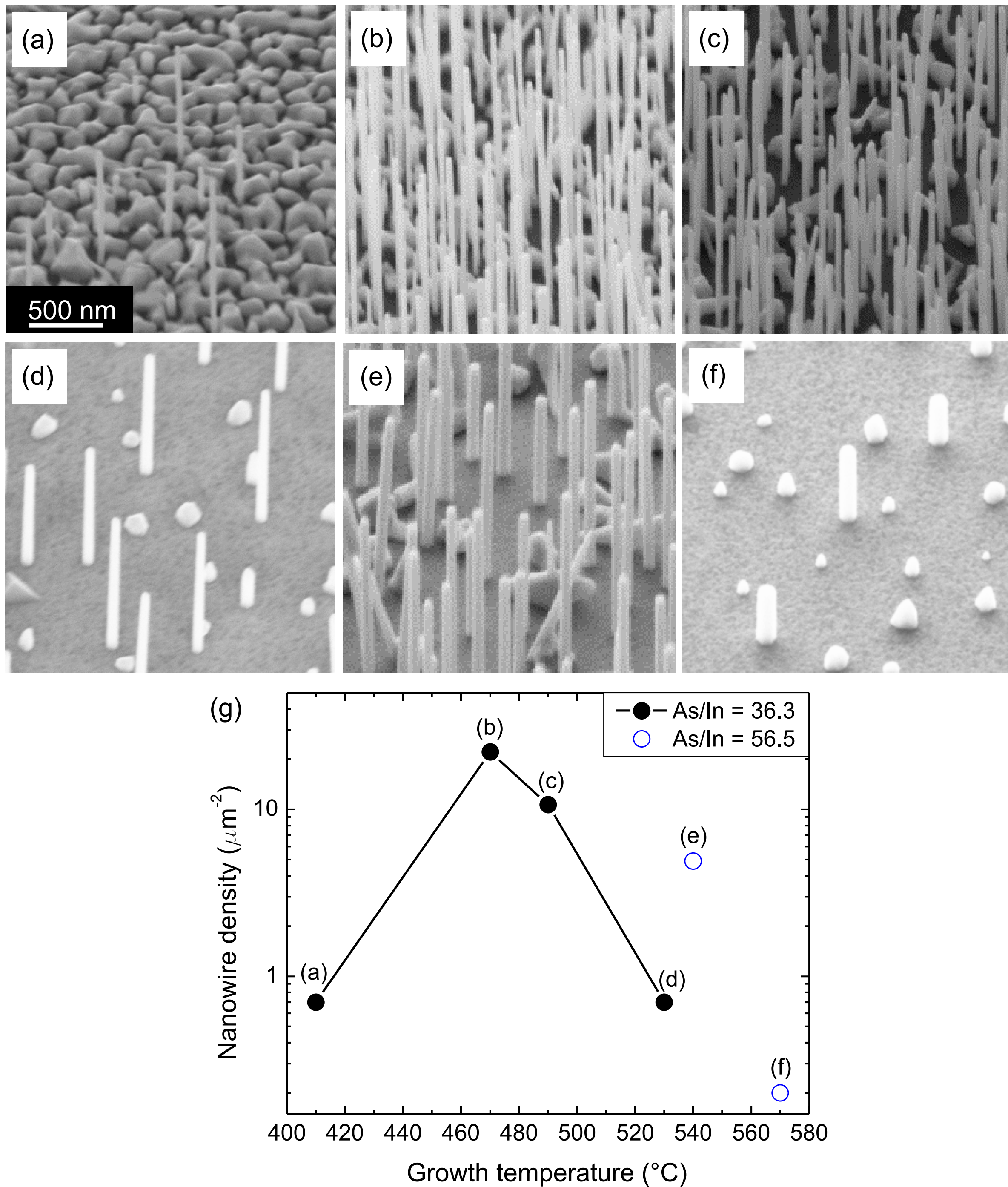

Figure 2.4. SEM images of InAs nanowires grown on a SiO_x /Si(111) substrate for different growth conditions, but fixed growth time (24 min). Samples (a)–(d) were grown with a V/III ratio of 36.3 at consecutively increasing growth temperatures of 410 ℃, 470 ℃, 490 ℃ and 530 ℃. Samples (e)–(f) were grown with higher V/III ratio of 56.5 and at higher temperatures of 540 ℃ (e) and 570 ℃ (f). Note that increased V/III ratio facilitated the growth of InAs nanowires at higher growth temperatures even up to 580 ℃. (g) Nanowire density of samples (a)–(f) as determined from top-view SEM images. Published in Ref. [Her12a].

of up to 570 ℃ were achieved (Figs. 2.4e, f). Here, the average nanowire densities were $\sim$4.9 NWs/µm^2 and $\sim$0.2 NWs/µm^2 for 540 ℃ and 570 ℃, respectively. For similar growth temperature, i.e., 530–540 ℃, the higher V/III ratio resulted in significantly enhanced nanowire length despite a nanowire density more than 5 times higher (compare Figs. 2.4d with 2.4e). Slightly modified In flux for the highest V/III ratio may also contribute to the observed length increase, however the effect was found to be very small (factor of 1.1). The trends for higher nanowire density with increased V/III ratio and/or reduced temperature can be attributed to suppressed surface migration lengths [Li11a], similar to growth of self-assembled three-dimensional InAs nanoislands on Si [Cir99] and InAs nanowires on InP(111)B substrates [Man06].

Effect of growth conditions on the axial growth rate

For a better overview of the dependence of nanowire dimensions on the investigated growth parameters, Fig. 2.5 depicts the values for (a) the axial growth rate and (b) the nanowire diameter summarized from a statistical analysis of >10 nanowires per sample. The axial growth rate is determined by dividing the SEM-measured nanowire length by the respective growth time, whereas the evolution of radial growth is strongly time-dependent (see section 5.3) and thus only the nanowire diameter is given for valid comparison of data. For each V/III ratio series the evolution in axial growth rate (Φ^{axial}) over temperature (Fig. 2.5a) shows similar behavior, i.e., reduced Φ^{axial} at the lower and higher temperature end and maximum growth rate ($\Phi^{\text{axial}}_{\text{max}}$) at intermediate temperature. Interestingly, the change in Φ^{axial} over growth temperature appears more sensitive for higher V/III ratios, whereas lower V/III ratios yielded almost invariable Φ^{axial} for a fairly wide temperature-window (e.g. $\Phi^{\text{axial}}_{\text{max}}$ = 2–3 Å/s for T $\sim$400–505 ℃, at V/III = 6.3).

Concurrent with the previous description, Fig. 2.5a also evidences a clear expansion of the possible nanowire growth window toward higher temperature with increasing V/III ratio. Simultaneously, with increasing V/III ratio $\Phi^{\text{axial}}_{\text{max}}$ shifts also to higher rates, i.e., $\Phi^{\text{axial}}_{\text{max}}$ = 3.0 Å/s, 7.3 Å/s and 13.9 Å/s ($\widehat{=}$ > 5 µm/h) at temperatures of 430 ℃ (V/III = 6.3), 470 ℃ (V/III = 36.3) and 500 ℃ (V/III = 56.5) (see also Table 2.1). It is important to note that the respective increase in $\Phi^{\text{axial}}_{\text{max}}$ is directly related to the increase in supplied V/III ratio. This suggests that for this particular parameter range the axial growth rate is strongly governed by the supplied V/III ratio, as further emphasized in detail in section 2.2.4. Moreover, the maximum temperature (T_{max}) for which nanowire growth is still feasible is 505 ℃ for V/III = 6.3, 560 ℃ for V/III = 36.3 and 580 ℃ for V/III = 56.5, as also listed in Table 2.1. It is worth mentioning that for the highest temperature T = 580 ℃ Φ^{axial} is still as high as 0.9 Å/s ($\widehat{=}$ 0.33 µm/h), while for temperatures above T_{max} small InAs droplets are formed

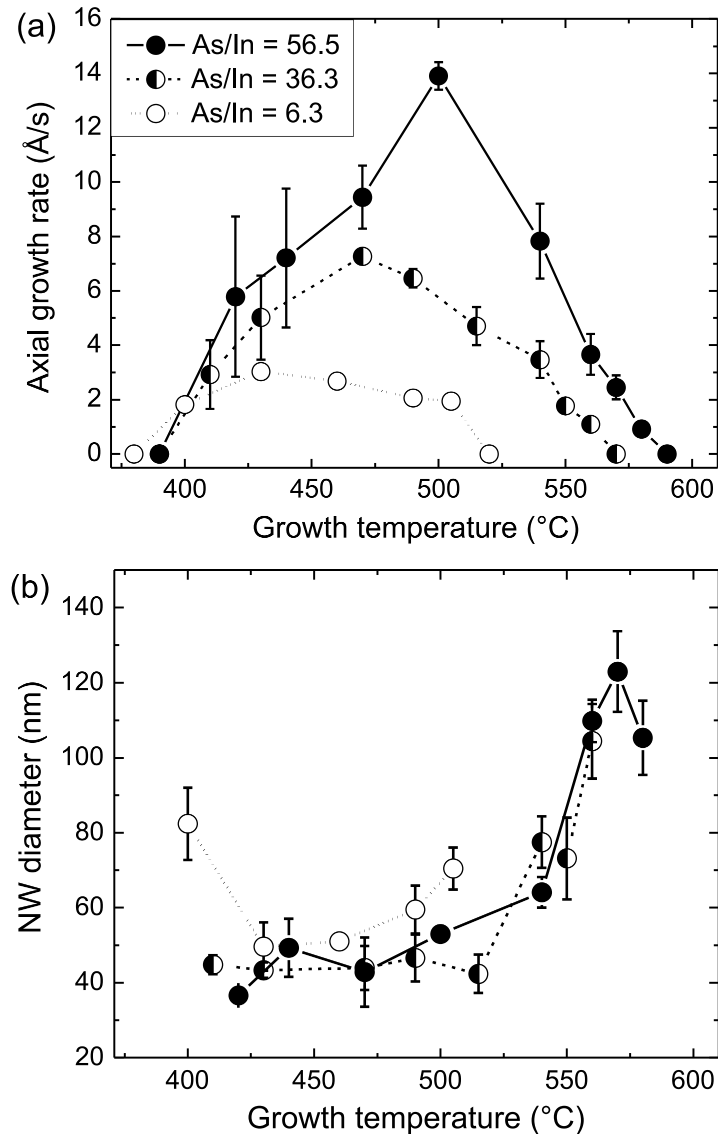

Figure 2.5. Axial growth rate (a) and nanowire diameter (b) as a function of growth temperature for different growth parameters, namely, V/III ratio of 6.3 (In = 0.24 Å/s, As = 1.51 Å/s), V/III ratio of 36.3 (In = 0.24 Å/s, As = 8.71 Å/s), and V/III ratio of 56.5 (In = 0.36 Å/s, As = 20.33 Å/s). A remarkable expansion in the available temperature range for successful InAs nanowire growth was observed with increasing V/III ratio. Published in Ref. [Her12a].

lacking the characteristic hexagonal nanowire cross section.

Overall, these results highlight the existence of a huge temperature range ($\sim$400–580 ℃) for the grown InAs nanowires under selection of appropriate V/III ratios. Of the few existing reports on the temperature-dependence of self-induced InAs nanowires by MBE, no work so far could demonstrate such high-temperature growth. Martelli et al. indicated a rather narrow temperature window of 370–450 ℃ ($\Delta T \approx 80$ ℃) for self-induced

Table 2.1. Growth parameters (V/III ratio, In and As fluxes) delineating the range of possible growth temperatures (T range), maximum nanowire growth rate ($\Phi^{\text{axial}}_{\text{max}}$) and according temperature of maximum growth rate [$T(\Phi^{\text{axial}}_{\text{max}})$].

V/III ratio	In flux (Å/s)	As flux (Å/s)	T range (℃)	$\Phi^{\text{axial}}_{\text{max}}$ (Å/s)	$T(\Phi^{\text{axial}}_{\text{max}})$ (℃)
6.3	0.24	1.51	400–505	3.0	430
36.3	0.24	8.71	400–560	7.3	470
56.5	0.36	20.33	400–580	13.9	500

InAs nanowires on Si(110) [Mar11]. Similar results were obtained for Au-catalyzed InAs nanowires [Mar11, Tch07], suggesting that beyond this temperature range segregation of the Au-In catalyst droplet occurs which limits successful nanowire growth [Tch07]. In contrast, Ihn et al. [Ihn07b] achieved Au-catalyzed InAs nanowire growth up to 500–520 ℃ in solid-source MBE. Common to all of these studies is their comparatively low V/III ratio, leaving the question whether growth is limited by the melting temperature of the stable Au-In phase (in Au-catalyzed nanowires) or limited by the applied V/III ratio. In the present MBE work the maximum growth temperature of $\sim$580 ℃ is obviously determined by the applied V/III ratio. Further increase of the V/III ratio is expected to shift the window even more toward higher-temperature growth. However, for solid-source III–As based MBE this would require unconventionally high As_4 BEP of more than 5×10^{-5} mbar.

To further explain the characteristic behavior of Φ^{axial} with temperature, one needs to differentiate between the low-temperature regime [$T < T(\Phi^{\text{axial}}_{\text{max}})$] and the high-temperature regime [$T > T(\Phi^{\text{axial}}_{\text{max}})$]. In the low-temperature regime, the surface migration length of In adatoms on SiO_x/Si(111) is rather low resulting in higher sticking coefficient and extensive cluster formation (e.g. Fig. 2.4a). With gradually increasing temperature, however, surface migration lengths become longer and the probability for incorporation at the nanowire growth front is enhanced, yielding longer nanowires. On the other hand, entering the high-temperature regime the subsequent decrease in nanowire length must be related to a significant loss of In, since parasitic clusters are largely suppressed and competitive incorporation processes can be neglected. Possible reasons for this In loss are twofold, i.e., either via thermally activated In desorption from the SiO_x/Si(111) surface or from large reverse reaction, i.e., thermally decomposing InAs nanowires. The analysis in the following section provides detailed insights into the In adatom desorption and thermal instability mechanisms during InAs nanowire growth in the high-temperature regime.

Effect of growth conditions on the nanowire diameter

Investigating the T-dependence of radial growth as a function of supplied V/III ratio (Fig. 2.5b), a quite different behavior is found. Most notable, for the two higher V/III ratios the nanowire diameter is nearly invariant (i.e., $\sim$40–60 nm) with T and V/III ratio over a large temperature region from 400 °C to 520 °C. Only the lowest V/III ratio exhibits some slight T-dependence within this region, although the nanowire diameter is still in proximity to the typical values obtained for the other V/III ratios. In contrast, exceeding T = 540 °C a strong increase in radial growth is observed, yielding nanowire diameters of >100 nm in the 560–580 °C range. The strong increase in radial nanowire growth rate at higher growth temperatures was recently also reported for InAs nanowires grown on bare and SiO_x-covered Si(111) and was associated with a diffusion-limited growth mechanism [Man06, Dim11]. In diffusion-limited growth increasing temperature results commonly in lower density nanowires, meaning that the capture area for surface diffusing In adatoms per nanowire is increased. This results in enhanced radial growth rates, in good agreement with interwire-dependent growth kinetics studies on position-controlled InAs nanowires on prepatterned SiO_2/Si(111), as will be shown in section 5.3.

2.2.3 In desorption and thermal decomposition measured by quadrupole mass spectrometry

To further understand the temperature-dependence of the InAs nanowire growth characteristics, it is important to investigate the adatom incorporation and desorption kinetics in a more atomistic fashion. Whereas in the low-temperature regime [$T < T(\Phi_{max}^{axial})$] the origin of the reduced growth rates is mainly attributed to competing cluster formation on the SiO_x/Si(111) substrate, the origin of the rate-limiting processes in the high-temperature regime [$T > T(\Phi_{max}^{axial})$] are not directly obvious and need to be further elaborated.

Analysis during nanowire growth

For in depth investigation *in-situ* line-of-sight quadrupole mass spectrometry (QMS) experiments were performed during nanowire growth to directly measure the In incorporation and desorption behavior from the growth surface. Fig. 2.6a displays a schematic illustration of the experimental setup of line-of-sight QMS, showing the important features of QMS ion gauge and small adjacent aperture necessary for line-of-sight probing of both In and As desorbing atoms. The QMS measurements were recorded via modified growth initiation procedure to guarantee desorption analysis free of shutter transients, which commonly

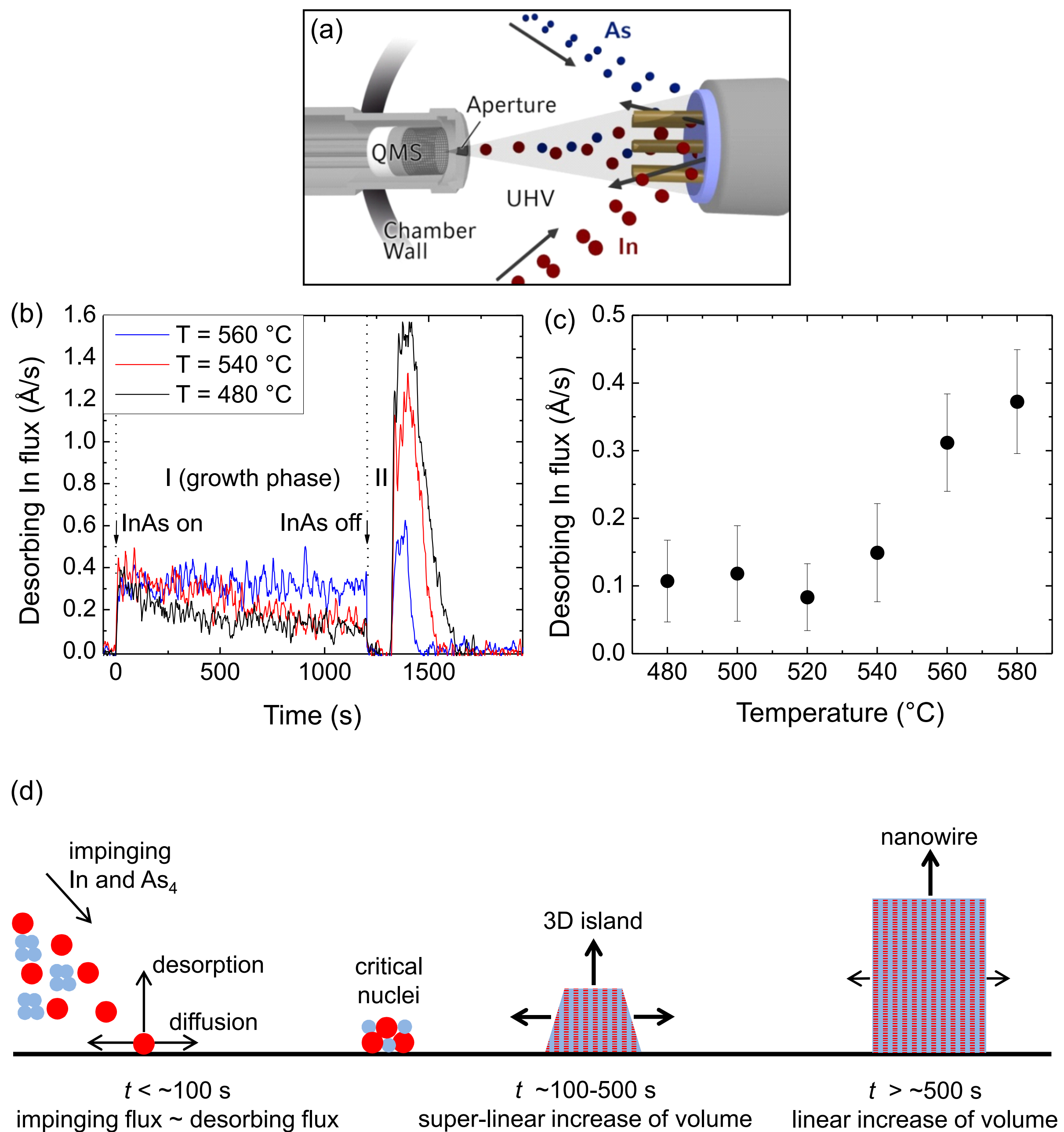

Figure 2.6. (a) Schematic illustration of the experimental setup for quantitative *in-situ* line-of-sight QMS during nanowire growth. (b) Line-of-sight QMS measurement of the desorbing In flux during nanowire growth for three different temperatures of 480 ℃, 540 ℃ and 560 ℃ (V/III = 56.5, t = 20 min). After growth (In and As shutters closed) the temperature was kept constant for 1 min prior to post-growth annealing at 730 ℃ to finally desorb all InAs from the wafer surface. (c) Desorbing In flux as derived from the steady-state part of regime I (growth phase) plotted as a function of growth temperature. (d) Schematic of the surface and growth processes during nanowire growth in regime I. Published in Ref. [Her12a].

obscure the beginning of growth. Prior to growth the substrate was tilted 90 degrees away from direct incidence of the effusion cells, and both In and As shutters were opened for flux stabilization. Since no flux was incident directly at the substrate surface, no desorbing In atoms were measured during this time. After 10 min the substrate was flipped to the growth position and growth was initiated under equilibrated In and As fluxes (t = 0), enabling line-of-sight QMS of the desorbing atoms.

In the first set of experiments, In desorption analysis was performed for a series of different growth temperatures under fixed V/III ratio of 56.5 (i.e., In = 0.36 Å/s, As = 20.33 Å/s) and growth time of 20 min (Fig. 2.6b). After growth (In and As shutters closed) the substrate was kept for 1 min at the given growth temperature before subsequent annealing in vacuum at 730 ℃ desorbed all grown InAs from the surface. This post-growth annealing step was employed for mass balancing purposes and to confirm the validity of the fully quantitative line-of-sight QMS method. In other words, by comparing the total amount of supplied In during the 20 min-long growth phase (0.36 Å/s $\times$ 1200 s = 432 Å of 2D equivalent coverage) with the total amount of desorbed In during both growth and post-growth annealing (i.e., integrated areas of desorption profiles in Fig. 2.6b), a perfect match between these In quantities was obtained (experimental error of < 5 %).

To closely identify the In desorption and the relevant rate-limiting mechanisms for the individual growth temperatures as depicted in Fig. 2.6b, two regimes are defined, marked as (I) **growth phase** and (II) **post-growth phase**. The **growth phase regime** encompasses the early nucleation and growth stage characterized by different evolution of desorption rate with time, which is largely dependent on growth temperature. The **post-growth regime**, on the other hand, defines the steady-state desorption rate right after growth termination, which appears to be negligibly small for all investigated temperatures. The individual regimes are described in more detail in consecutive order.

Right upon growth initiation, almost all impinging In atoms (In flux of 0.36 Å/s) desorb completely from the SiO_x/Si(111) surface, nearly independent of the investigated growth temperature. This is because in SiO_x-masked heteroepitaxy of highly mismatched systems no wetting of the substrate by In adatoms takes place and 3D nucleation phenomena govern the In adsorption/desorption kinetics. Specifically, in wetting-layer free 3D island growth a large energy barrier for nucleation prevails based on the competition between surface and volume free energies of forming islands [Lew79]. This results in a reduced sticking coefficient right at the beginning of growth when islands are below a critical size and most adatoms re-evaporate. When islands grow beyond a critical size, growth continues with a decrease in total free energy and adatom incorporation at the stable islands increases steadily as the 3D island volume increases. This situation describes the observation of

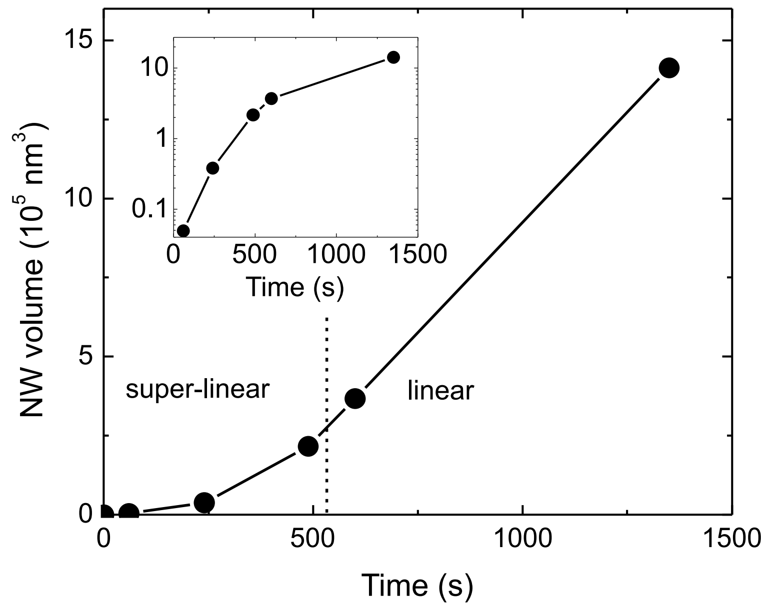

Figure 2.7. Evolution of InAs nanowire volume as a function of time for a series of growths (t = 60–1350 s) under fixed V/III ratio (12.6), temperature (480 ℃) and nanowire density (∼25 µm^{-2}). Note the transition from super-linear to linear growth occurring in between 500 to 600 s of growth. The inset shows the same curve with logarithmic scale. Published in Ref. [Her12a].

continuously decreasing desorption with time, until a steady-state In desorption level is reached. This is evident at least for the lower temperatures of 480 ℃ and 540 ℃, while growth at the highest temperature (560 ℃) is limited by overall fewer nucleation events (much less island densities) and larger re-evaporation of diffusing In adatoms (as discussed below). Similar non-linear characteristics of the group-III element desorption measured by line-of-sight QMS were previously also reported for 3D nucleation of heteroepitaxial GaN islands on SiC [Kob02] and GaN nanowires on Si(111) [Che10].

To prove the direct relation between non-linear decay in In desorption and associated non-linear increase in 3D island volume a growth-time dependent study was performed for InAs nanowires grown with constant V/III ratio (12.6), temperature (480 ℃) and nanowire density (∼25 µm^{-2}). The growth times were varied from 60 s to 1350 s encompassing the whole range of evolution from small 3D islands to larger InAs nanowires with steady-state growth rate. The nanowire volume as derived from length and diameter data (measured by scanning electron microscopy) is plotted in Fig. 2.7 both in linear and logarithmic (inset) representation. As expected, the nanowire volume evidences the typical super-linear increase with time for the initial ∼500 s of growth before the transition to linear growth rate occurred. Such initial power-law growth behavior was also observed during other InAs nanowire growth experiments as well as in many other heteroepitaxial systems, e.g.

self-induced 3D GaN island growth [Hea96, Kob02]. This super-linear growth indicates that significant amounts of In are lost. However, once linear volume growth is reached the loss of In is constant, which is exactly represented by the transition from non-linear to steady-state desorption in Fig. 2.6b, confirming the interpretation of the In desorption characteristics of the **growth phase regime**.

Note further, that the existence of the steady-state In desorption rate corroborates a constant 3D island (or nanowire) density throughout the entire growth procedure, since continuous nucleation would result in non-constant adatom desorption rates over time. Indeed, saturated nanowire densities right upon growth initiation are further confirmed in growth-time dependent studies of self-induced InAs nanowires (see section 3.3), and were also found by other groups [Dim11].

Under these considerations, the different T-dependencies of the initial In desorption can be well explained. While the lowest temperature (T = 480 °C) resulted in the fastest and most pronounced decay, higher temperatures (T = 540 °C and 560 °C) yielded much less reduction in In desorption and substantially decreased nanowire densities. This is due to the increased re-evaporation of the wider diffusing In adatoms on the SiO_x/Si(111) surface.

Once initial 3D island nucleation is completed, the subsequent transition to steady-state desorption marks the actual nanowire growth stage. Here, nanowire growth and desorption are in an obvious dynamic equilibrium, meaning that stable nanowire growth takes place at an overall fixed rate, both for the axial and radial rates. This dynamic equilibrium can be referred to the condition where the radial nanowire growth rate drops significantly meaning that the major contribution to the nanowire volume increase stems from the constant axial growth rate. The steady-state In desorption level in this regime evidences an interesting increase with growth temperature, as plotted in Fig. 2.6c. In particular, the desorption rate shows a pronounced increase for T > 520 °C, reaching even nearly the rate of the total supplied In flux for temperatures between 560–580 °C. From this it is not clear at this point whether the dominant desorption mechanism arises from the low adsorption probability on the SiO_x/Si(111) surface or from a strong reverse reaction, i.e., thermal decomposition and large adatom detachment rate at the nanowire growth front at elevated temperatures.

To resolve this, the **post-growth regime** shows specifically the In desorption rate after InAs nanowire growth was terminated by closure of both In and As shutters, i.e., during post-growth desorption in vacuum at the given growth temperature. Interestingly, for the entire investigated temperature range (480–580 °C) the In desorption rate during post-growth desorption was found to be negligibly small. Only upon further increase of the substrate temperature to maximum annealing conditions (730 °C) the as-grown nanowires are fully thermally decomposed, as evidenced by the individual post-growth annealing

desorption peaks in Fig. 2.6b. Since for the highest growth temperatures the nanowire density was extremely small (compare Fig. 2.4f), detection of the low In desorption rate during post-growth thermal decomposition of the as-grown nanowires might be limited by the background of the QMS ($\sim 1\times10^{-14}$ mbar).

Thermal stability of InAs nanowires

To investigate the thermal stability of InAs nanowires, a second set of experiments was performed, where first InAs nanowires were grown under conditions (V/III ratio = 56.5, T = 500 ℃) to achieve a good nanowire density (5–10 NWs/µm^2) with reasonable length of $\sim$2.5 µm. After closure of both In and As shutters, the sample was cooled down to 300 ℃ and the MBE chamber was pumped to the base pressure of $1–2\times10^{-11}$ mbar for several hours. Subsequently, the InAs nanowire sample was heated up in UHV in increments of 20 ℃ steps and stabilized for 2 min at each temperature while both desorbing ^{115}In and ^{75}As atoms were recorded simultaneously by QMS. The results are depicted in Fig. 2.8a showing an onset temperature for desorption of both In and As atoms (in 2D equivalent rates) of around 540–560 ℃. Moreover, for annealing temperatures exceeding 640 ℃, the InAs nanowires seemed to be completely decomposed as the As desorption level decreased rapidly to zero (not shown). Note that under these static conditions (i.e., post-growth thermal decomposition), As desorption appears to yield much higher desorption rate due to the higher equilibrium vapor pressure of As atoms as compared to In atoms at a given temperature. As mentioned before, the In desorption rate under the static, post-growth conditions was quite small, despite the significantly increased nanowire density and surface coverage. This indicates that In desorption from the nanowire growth front or sidewall facets is infinitesimally small and increases only significantly for T > 560 ℃. The limited In desorption here is most likely due to a phase transition of thermally decomposing InAs nanowires to In droplets (see Fig. 2.8d), where In atoms need to overcome a much higher energy barrier for desorption as compared to freely migrating In adatoms on SiO_x surfaces [Kin08]. To verify the thermal decomposition data derived by *in-situ* QMS, three InAs nanowire samples were further grown under identical conditions (V/III = 24.2, T = 500 ℃, t = 24 min) and two of them were exposed to extended, 2h long post-growth annealing steps under similar MBE vacuum conditions at two distinct temperatures, i.e., 540 ℃ and 580 ℃. Subsequent SEM analysis was performed on all three samples, showing representative micrographs in Figs. 2.8b–d. The nanowires of the as-grown reference sample have a length of 1202 nm $\pm$ 62 nm (Fig. 2.8b). In consistence with the QMS data, the InAs nanowire sample annealed at 540 ℃ shows very similar lengths (1214 nm $\pm$ 70 nm), demonstrating that negligible thermal decomposition of the nanowires occurred up

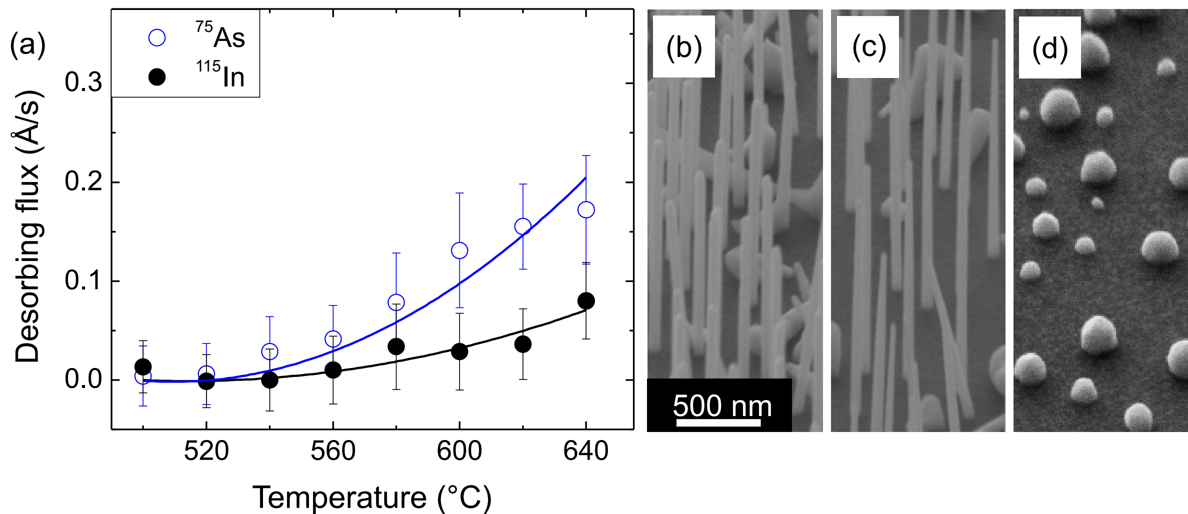

Figure 2.8. (a) Desorbing In and As flux during thermal decomposition of InAs nanowires in ultra-high vacuum (1–2$\times$10^{-11} mbar) under static (i.e., post-growth) conditions. Prior to the experiment nanowires were grown for 30 min (V/III = 56.5 and T = 500 °C) to typical lengths of $\sim$2.5 µm. Upon incremental heating in steps of 20 °C, the desorbing In and As fluxes evidenced an onset temperature for thermal dissociation of InAs nanowires at around 540 °C. Best fits to the data points serve as a guide to the eye. (b–d) SEM images of three InAs nanowire samples grown under identical conditions (V/III = 24.2, T = 500 °C, t = 24 min) showing (b) the as-grown InAs nanowires (L = 1202 nm $\pm$ 62 nm), (c) nanowires after annealing at 540 °C for 2 h (L = 1214 nm $\pm$ 70 nm), demonstrating negligible thermal decomposition of the nanowires at this temperature, and (d) residues of nanowires (In droplets) after annealing at 580 °C for 2 h. Published in Ref. [Her12a].

to this temperature (Fig. 2.8c). On the other hand, the nanowire sample annealed at the higher temperature (580 °C) evidences completely decomposed nanowires (Fig. 2.8d), leaving merely residual metallic In droplets behind. Overall, these results demonstrate surprising thermal stability of (111)-oriented InAs nanowires well above 500 °C, even under ultra-high vacuum conditions in the absence of super-saturation. It can be suggested that this arises from the thermally more stable (111) (growth front) and (110) (sidewall) surfaces as compared to the conventional (001) InAs surfaces, where InAs thermal decomposition readily takes place for lower temperatures of around 500 °C [Cha84]. Certainly, comparison of absolute onset temperatures for thermal decomposition as measured in different systems needs to be reckoned with care due to different temperature calibration schemes. To substantiate these arguments, additional QMS desorption experiments were performed on 500-nm-thick planar (100) and (111)B InAs wafers with otherwise identical specification. Similar to the decomposition experiments performed for the nanowires, the InAs wafers were heated in UHV in increments of $\sim$10 °C steps (with 2-min-long stabilization at each

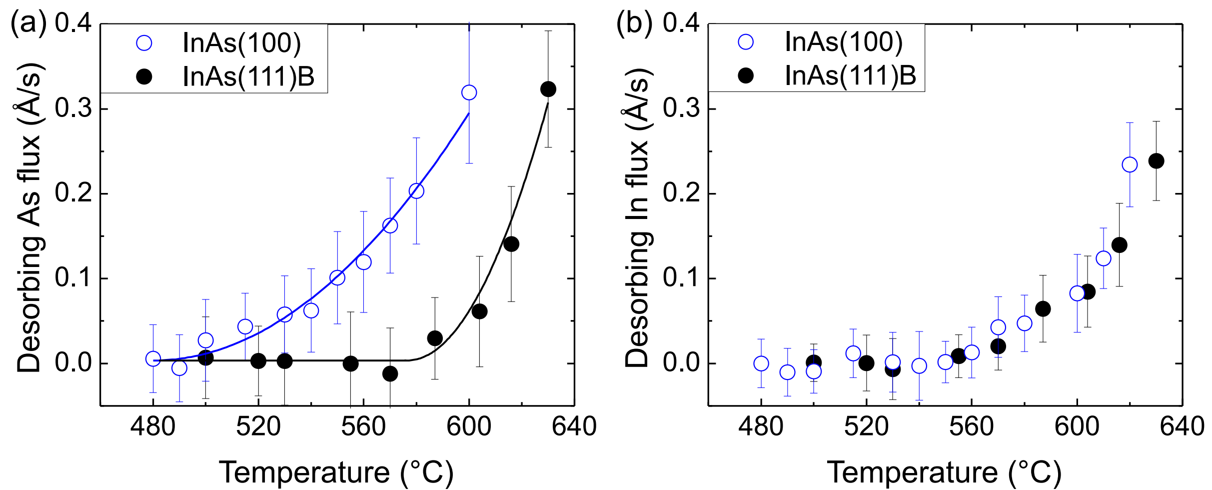

Figure 2.9. Desorbing As (a) and In (b) fluxes during thermal decomposition of planar (100) and (111)B InAs surfaces. Experiments were performed in UHV without any supplied fluxes, to compare directly to data derived from (111)-oriented InAs nanowires in Fig. 2.8. The data confirms that the (111)B-oriented InAs surface is thermally more stable, evidenced by a shift in the onset of As desorption as compared to the (100) InAs surface. Published in Ref. [Her12a].

temperature) while recording the desorption of ^{115}In and ^{75}As atoms (see Fig. 2.9). The results evidence significantly different desorption characteristics between the (100) and (111)B wafer surface. In particular, the ^{75}As desorbing flux, which directly correlates to the breaking of the near-surface In–As bonds, is shifted by about ∼40–80 ℃ to higher temperatures for the (111)B InAs surface (see Fig. 2.9a). The respective onset temperature for decomposition correlates also well with the one found for the (111)B-oriented nanowires and confirms that the (111)B InAs surface is thermally more stable than the respective (100) InAs surface. As expected, no difference in desorption characteristics is found for desorbing In atoms between the (100) and (111)B InAs surface (see Fig. 2.9b), since In desorbs through a second-order process via formation of In droplets and subsequent desorption from the metallic In reservoir (as noted before).

These findings correspond well to early thermal annealing experiments of GaAs surfaces where it is also well known that large (110) and (111) facets stabilize as the thermodynamically most stable surfaces in III–As based materials upon decomposition [Hor89]. Under dynamic growth conditions where enhanced supersaturation prevails by excess As_4, the onset for thermal decomposition is thus expected to shift to even much higher temperatures. This suggests that the reverse reaction (thermal dissociation) is not the dominating rate limiting factor for the as-grown InAs nanowires as presented here. Instead, since significant decrease in axial growth rate occurs already well below the onset of vacuum

thermal decomposition (T ∼540 ℃), the growth rate limiting factor is thus largely governed by re-evaporation from migrating In adatoms on the SiO_x/Si(111) surface. This further explains the observed extension of the growth window to higher temperature with increasing V/III ratio, since under higher excess As the capture probabilities with surface migrating In adatoms are increased, leading to higher nanowire densities and hence reduced In re-evaporation rates (see also sections 2.2.4 and 3.3).

Furthermore, the increased thermal stability for the InAs nanowires may also be directly associated with the In-droplet-free growth mode (the confirmation of this growth mode is given in chapter 3). Various studies of III–V semiconductor surfaces proved that the presence of macroscopic droplets of the group-III element enhances the reverse (i.e., thermal decomposition) reaction quite drastically [Sch65, Li11b]. This may set an upper limit for the feasible growth temperature in droplet-assisted (group-III-rich) III–V growth, where the forward, i.e., growth reaction cannot compensate for the large loss through the reverse reaction. For MBE grown InAs nanowires, this could also explain the large discrepancy in growth temperature window between the present results and the much lower temperatures found for self-catalyzed InAs nanowires by other groups [Mar11].

2.2.4 Effect of In and As fluxes on the nanowire growth rates

Up to now, primarily the effect of growth temperature and different V/III ratios on the growth parameter space and the related axial and radial growth rates was investigated (Figs. 2.4 and 2.5). In the following, the effective V/III ratio at the nanowire growth front is elaborated in more detail by investigating the influence of the individual fluxes (In versus As fluxes) on the nanowire growth kinetics. For this purpose, two separate studies are performed, i.e., (a) an As flux series under fixed In flux and temperature, and (b) an In flux series under fixed As flux and temperature.

As flux series

First, for the As flux series all growth experiments were performed at an In flux of 0.36 Å/s and a temperature of 500 ℃ for constant growth time of t = 24 min, but variable As flux ranging from 2.90 Å/s to 29.04 Å/s. Fig. 2.10a depicts the As flux dependence of axial growth rate (Φ^{axial}) and the nanowire diameter as derived from a statistical analysis of corresponding SEM micrographs. As a reference the 2D equivalent As rate is also given as red dashed line. Interestingly, Φ^{axial} of the nanowires increases linearly and follows exactly the 2D equivalent As rate up to As flux rates of 15 Å/s. Beyond supplied As fluxes of 15 Å/s Φ^{axial} saturates and remains constant as illustrated by the horizontal dashed line

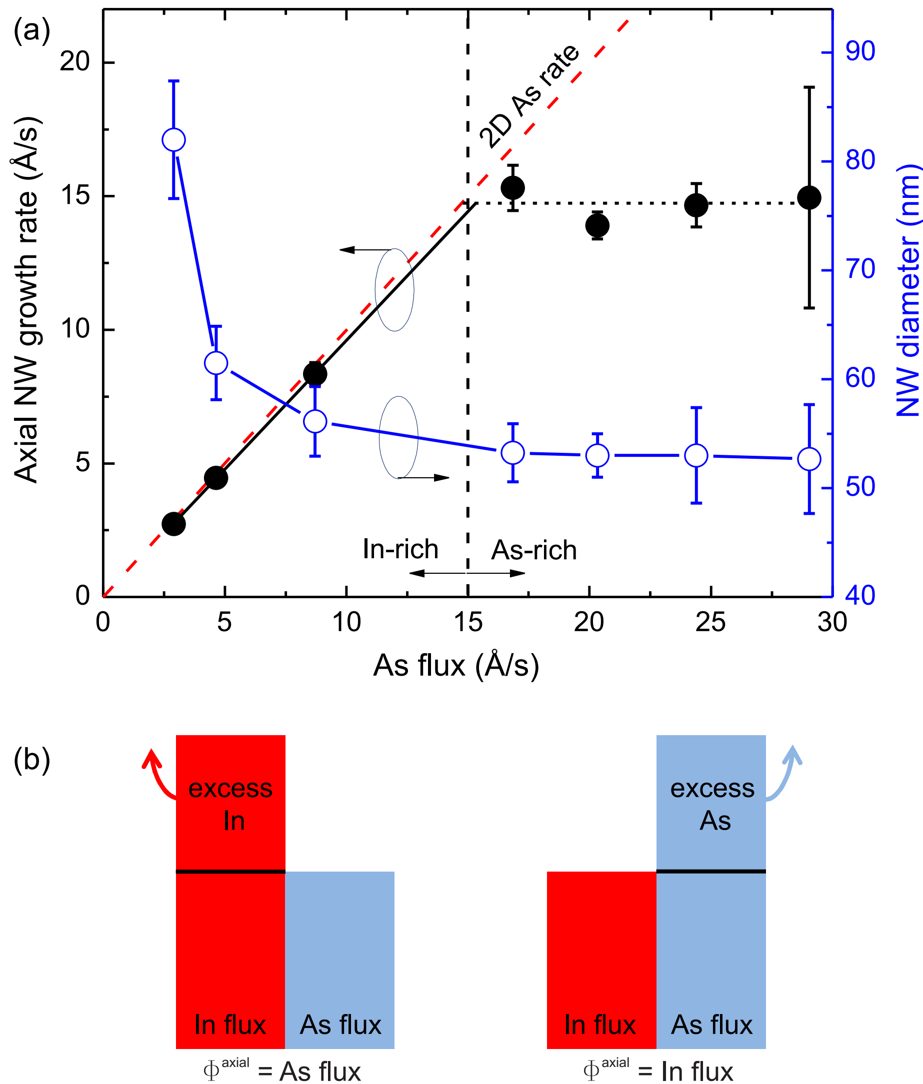

Figure 2.10. (a) Axial growth rate and nanowire diameter plotted as a function of the supplied As flux for fixed T = 500 °C and In = 0.36 Å/s. The variable 2D-equivalent As flux rates are also indicated by the red dashed line. The As flux dependency evidences a characteristic increase and saturation behavior, indicating a transition from In-rich (As-limited) to As-rich (In-limited) growth conditions. The transition boundary corresponds to an *effective* As/In ratio equal to 1. (b) Schematic of an In-rich vs. As-rich growth regime. Published in Ref. [Her12a].

(guide to the eye). In contrast, the nanowire diameter exhibits a different behavior although a similar transition occurs near the critical As flux of ∼15 Å/s. For As fluxes < 15 Å/s, the nanowire diameter decreases rapidly, and is found to be constant for As fluxes > 15 Å/s. These results mean that higher As fluxes result in longer and thinner nanowires, and that for fixed growth time their dimension and aspect ratio are completely invariable under very high As fluxes (> 15 Å/s). Note that for the investigated range the nanowire density varied only marginally, i.e., slightly increasing density with increasing As flux (∼4–7 NWs/µm^2).

Considering that with increasing density nanowire growth is commonly accompanied by large redistribution of arriving adatoms, one would expect rather a decrease in the axial nanowire growth rate (see section 5.3). However, here the opposite trend is observed, i.e., with increasing As flux and slightly increasing nanowire density, the axial growth rate is significantly increased. Therefore, other mechanisms than density-based redistribution of adatoms must be responsible for the observed sharp transition in growth rate.

The transition in growth rate near the critical As flux of 15 Å/s is most likely associated with a transition from locally In-rich [$(As/In)_{eff} < 1$] to locally As-rich [$(As/In)_{eff} > 1$] conditions, similar to observations for self-induced GaAs nanowires [Rud11] and catalyst-free GaN nanocolumns [Che10]. The transition point [$(As/In)_{eff} = 1$] is marked in Fig. 2.10a by the vertical dashed line, defined by the intercept between the linearly increasing 2D equivalent As rate (red line) and the trend line for the saturated axial nanowire growth rate. Here, $(As/In)_{eff}$ describes the *effective* As/In ratio at the (111)B-oriented nanowire growth front, which is quite different from the supplied As/In ratio due to locally increased In fluxes arising via adatom diffusion across the SiO_x surface. This means that despite the nominally supplied As-rich conditions (V/III ratios $\gg 1$), In-rich growth conditions can still prevail at the nanowire growth front under certain conditions. Thus, as illustrated in Fig. 2.10b, for low supplied As fluxes the axial growth rate is As-limited (In-rich growth regime), while for higher As fluxes the saturated growth rate is In-limited (As-rich growth regime). Interestingly, within the In-rich growth regime the axial growth rate does not exceed the 2D equivalent As rate. This finding differs from other metal-rich grown, self-catalyzed nanowire systems where excess of the metal element yields often axial growth rates larger than the expected 2D equivalent rate [Rud11, Jab08]. Such enhanced nanowire growth rates are mostly attributed to the underlying VLS growth mechanism and corresponding fast crystal phase nucleation in the presence of a liquid droplet [Col08, Rud11]. Obviously, this appears different for the present In-rich InAs nanowire growth, suggesting that macroscopic In droplets are absent, likely due to the very high equilibrium In vapor pressure and large In desorption at the nanowire growth front. This situation mimics further the dynamically stable group-III-rich (droplet-free) surface growth conditions as found for a variety of planar III–V (mostly group-III nitride based) surface structures [Hey00, Kob05, Kob07]. Since In desorption is a thermally activated process, it should be noted that one might expect In droplet accumulation at the nanowire growth front under decreased growth temperatures. However, within the investigated temperature range (380–590 °C) this was never observed and the axial growth rate never exceeded the 2D equivalent As rate. This is consistent with growth dynamics studies of self-induced InAs nanowires on prepatterned SiO_2/Si(111) substrates (see section 5.2) and bare Si(111) surfaces [Dim11]. In addition, it has to be

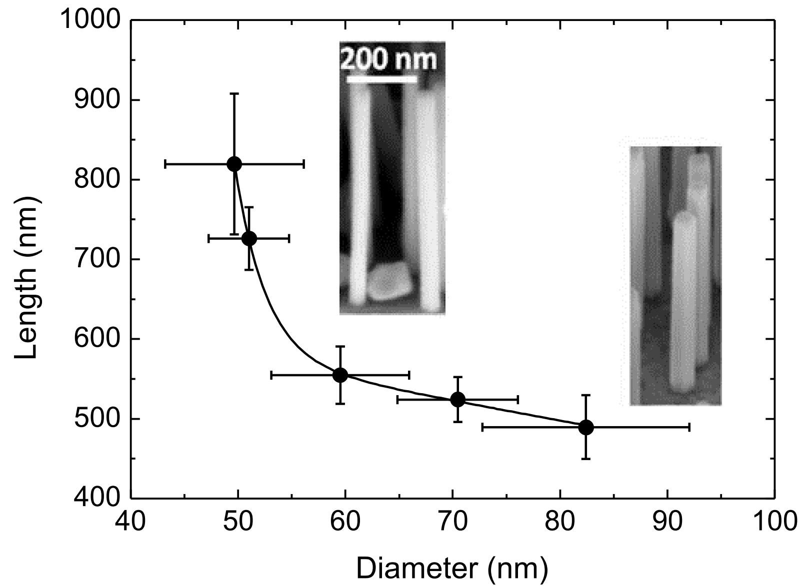

Figure 2.11. Plot of the length to diameter behavior of InAs nanowires grown with As/In ratio of 6.3 at different substrate temperatures. The insets show SEM images of the two extreme cases: the longest (smallest) and shortest (thickest) nanowires. A best fit to the data points illustrates the $L \propto D^{-1}$ dependence – a characteristic behavior of diffusion-limited nanowire growth.

stressed that the observed In-to-As-rich transition in Fig. 2.10a should be applicable to any arbitrary set of In fluxes and growth temperature. This is expected to result in a shift of the boundary As flux, i.e., $(As/In)_{eff}$ = 1, along the As flux axis, meaning shifts to higher (lower) boundary As fluxes when In fluxes (growth temperature) are increased.

To interpret the As flux dependence of the nanowire diameter, one needs to differentiate between whether growth occurs either in the As-limited (In-rich) or the In-limited (As-rich) growth regime. For growth in the In-rich regime, increased lateral growth at lower As flux corresponds to a decreased axial growth, giving an inverse Φ^{radial} to Φ^{axial} dependence. This $L \propto D^{-1}$ dependence is further confirmed by the graph depicted in Fig. 2.11 where the lengths and diameters are plotted for nanowires taken from the sample series discussed in Fig. 2.5 (V/III = 6.3). A best fit through the data points corroborates the suggested inverse length to diameter dependence. Such inverse dependence is a characteristic of sidewall diffusion-limited growth of catalyst-free nanowires, as observed for a variety of material systems [Cal07a, Che10]. In this case, nanowire growth proceeds primarily via In adatom diffusion from the surrounding SiO_x-masked Si(111) substrate and (110) sidewall facets, where the latter is largely determined by the effective As/In flux ratio at the surface at the given temperature. For low As/In flux ratio at the nanowire tip not enough In can be incorporated to maintain a strong diffusion flux along the sidewalls. Consequently,

the In adatom concentration on the sidewalls is higher, and the probability for sidewall incorporation increases. With increasing effective As/In ratio surface adatom diffusion increases and incorporation at the nanowire growth front becomes more favorable than lateral sidewall incorporation. At the limit to As-rich growth the nanowire diameter saturates since here growth is obviously limited by the available In flux, defining a group-III-limited regime rather than a diffusion-limited regime. This agrees well with a previous report of catalyst-free grown InAs nanowires by MOCVD [Tom07b], where large excess AsH_3 supply had only limited effects on the diameter and the axial growth rate, confirming that growth is group-III limited under high excess As supply.

In flux series

In the second series, growth experiments were performed under variable In flux (0.24–0.90 Å/s) under otherwise constant conditions, i.e., fixed As flux of 20.33 Å/s, T = 500 ℃ and growth time of t = 24 min. Again, a statistical analysis of the nanowire dimensions from the entire sample series was performed and the respective axial growth rate (Φ^{axial}) and nanowire diameter were plotted as a function of supplied In flux in Fig. 2.12a. Since the chosen As flux was quite high (well in the As-rich regime of Fig. 2.10a), nanowire growth is expected to occur under In-limited conditions for most In fluxes. This trend is well observed, as with increasing In fluxes (at least up to $In \sim$0.6 Å/s) both Φ^{axial} and the nanowire diameter increase consecutively, validating further the previous assumptions. In this As-rich regime the axial growth rate scales directly with In flux and its quantity thus corresponds to the equivalent 2D In flux rate present at the nanowire growth front. Note that this equivalent 2D In rate is much higher than the supplied In flux, indicating that nanowire growth is strongly governed by huge In diffusion from the SiO_x/Si(111) surface. Interestingly, the ratio between the equivalent 2D In rate at the nanowire growth front and supplied In flux drops from ratio 45 to ratio 25 with increasing In flux beyond 0.6 Å/s. This indicates that despite larger supplied In fluxes less In arrives at the nanowire growth front, meaning that enhanced cluster formation must occur at higher In fluxes.

Furthermore, Φ^{axial} approaches the 2D equivalent As rate (As = 20.33 Å/s) at high enough In fluxes (0.60–0.80 Å/s). Under these conditions the maximum growth rate of 16.7 Å/s was achieved, corresponding to more than 6 µm/h. For In fluxes above this range, transition to In-rich growth is expected to occur in a similar fashion as described before and Φ^{axial} should be constant, limited by the active As flux. Likewise, the nanowire diameter also evidences the expected increase toward the transition to In-rich growth. However, a notable deviation from the expected behavior is observed for In-rich, As-limited growth conditions, i.e., a drop in growth rate, which is associated with substantial cluster formation

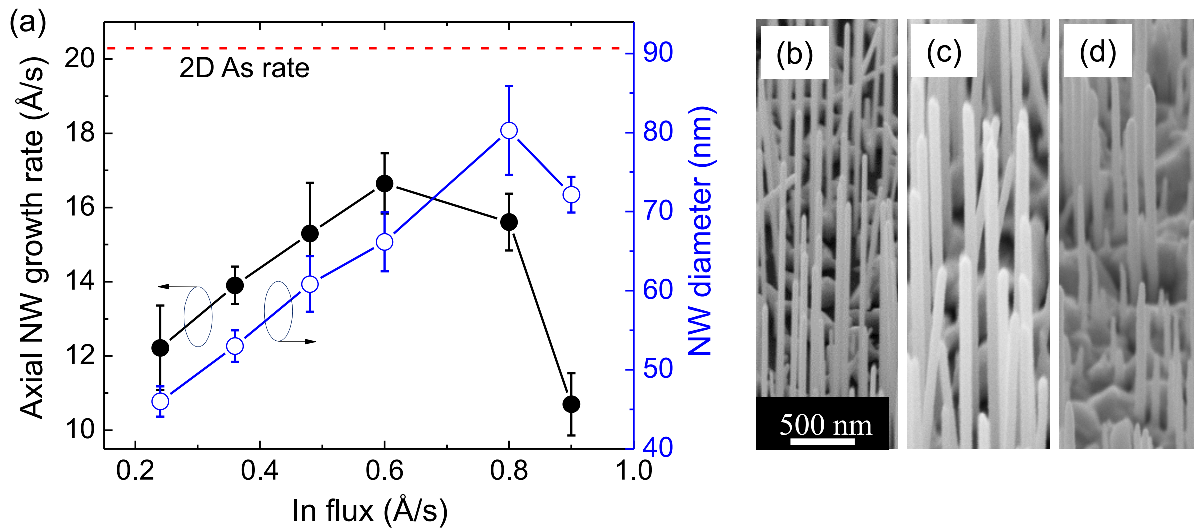

Figure 2.12. (a) Axial growth rate and nanowire diameter as a function of the supplied In flux for fixed growth temperature (T = 500 °C) and As flux (20.33 Å/s). Note the increase in growth with increasing In flux toward the 2D-equivalent As flux rate (indicated by red dashed line). For very high In fluxes both axial growth rate and nanowire diameter decline due to excessive cluster formation. (b–d) Representative SEM images of three InAs nanowire samples grown under different In fluxes of 0.36 Å/s, 0.80 Å/s, and 0.90 Å/s, respectively. Larger amounts of clusters are formed under higher In fluxes. All nanowire morphologies appear non-tapered, corroborating the underlying In-droplet free growth mechanism. Published in Ref. [Her12a].

under very high In fluxes. Excessive cluster formation between the InAs nanowires for increased In fluxes is directly evidenced in the SEM micrographs of Fig. 2.12b–d. Moreover, it should be mentioned that the nanowires exhibit no tapering for all investigated In fluxes. This is in contrast to autocatalytic growth of GaAs nanowires, where variation in supplied Ga flux resulted in strong tapering behavior due to a dynamically non-equilibrated nanowire growth front with accumulation of the group-III element in the form of liquid droplets [Col08]. While this behavior is commonly associated with the underlying VLS growth mode in auto-catalyzed GaAs nanowires, the absence of tapering in InAs nanowires indicates that a VLS-free growth mode is very likely even in the case of effective In-rich growth conditions. For further details on the growth mechanism of self-induced InAs nanowires see chapter 3.

2.3 Conclusion

In conclusion, the MBE growth of self-induced and self-assembled (spatially unordered) InAs nanowires on SiO_x covered Si(111) was presented. First, basic investigations of

the nanowires by means of SEM, TEM and XRD revealed vertically aligned, untapered and catalyst-free nanowires with hexagonal cross section. Furthermore, the entire growth parameter space for these InAs nanowires was delineated. Surprisingly huge growth temperature ranges were obtained with maximum temperatures up to 580 ℃ under increased V/III ratio, surpassing significantly the typical growth temperature range for catalyst-assisted, VLS-grown InAs nanowires. These conditions further highlight remarkable growth rate enhancement of axial growth rates to more than 6 µm/h. Systematic studies of the group-III and group-V flux dependencies on growth rate revealed two apparent growth regimes, an In-rich (As-limited) regime and an As-rich (In-limited) regime defined by the effective As/In flux ratio at the nanowire growth front. Further fundamental knowledge of the growth physics in high-temperature InAs nanowire growth was obtained by fully quantitative *in-situ* line-of-sight QMS, allowing direct determination of the critical desorption and thermal decomposition processes of InAs nanowires at elevated temperatures. Both under dynamic (i.e., growth) and static (no growth, ultra-high vacuum) conditions the (111)-oriented InAs nanowires were found to be thermally extremely stable. Decreased nanowire growth rate at very high-temperature growth is thus primarily limited by excess In desorption from the SiO_x-masked Si(111) surface under In-limited conditions. The remarkable capability of high-temperature growth combined with excellent thermal stability is opening up unique possibilities to process and operate InAs-based nanowire devices even at elevated temperatures (> 500 ℃) and to alloy non-catalytic InAs nanowires with GaAs for full composition-tuning in ternary InGaAs nanowires as shown in chapter 6.

3

Growth mechanism of self-induced InAs nanowires

In this chapter insights into the underlying growth mechanism of self-induced InAs nanowires will be elucidated. Before going into several details, a brief introduction and explanation of the predominant nanowire growth mechanisms, the vapor-liquid-solid (VLS) and vapor-solid (VS) growth mechanism, is given. Based on several complementary methods, such as *in-situ* RHEED and *ex-situ* SEM and TEM it will be shown that the growth mechanism of self-induced InAs nanowires on SiO_x-templated Si(111) is governed by a non-catalytic (VS) growth mechanism free of the formation of In droplets. The results presented in this chapter are published in Refs. [Her11, Rud11].

3.1 Self-induced nanowire growth – Growth mechanism

3.1.1 Self-catalyzed nanowire growth

Recently, increasing effort has been devoted to avoid foreign catalysts for achieving high purity nanowires free of metallic contaminants. The basic idea behind self-catalyzed nanowire nucleation – which was already discussed by Wagner and Ellis 1964 – is that the liquid catalyst is formed by one of the constituent materials of a compound nanowire. For III–V nanowires two methods typically facilitate self-catalyzed nanowire growth, namely (i) the intentional deposition of one of the materials prior to growth (typically the group-III element) [Mat06] or (ii) a joint supply of both materials under optimized growth conditions, leading to the autonomous formation of the liquid catalyst [Sta03, Nov05, Fon08a]. An illustration of self-catalyzed nanowire growth is depicted in Fig. 3.1a with group-III atoms (in red) and As_4 molecules (in blue).

In III–V based nanowire growth without foreign catalysts, most growth reports – except for nitride-based nanowires (GaN, AlN, InN and related alloys) [Cal07a, Cal07b, Che10] – relied on this self-induced VLS growth mechanism. Especially in III–As based nanowires this self-catalyzed growth mode has become a favorable method for ready formation of nanowires with high growth rate on almost any substrate [Col08, Pli10, Man10, Bre11]. In the various studies significant understanding of nucleation mechanisms, nanowire size and morphology dependencies on growth parameters was gained.

3.1.2 Catalyst-free nanowire growth

Regarding the various issues still remaining for self-catalyzed nanowire growth (see Introduction for details), one would prefer to avoid the droplet-assisted VLS mechanism

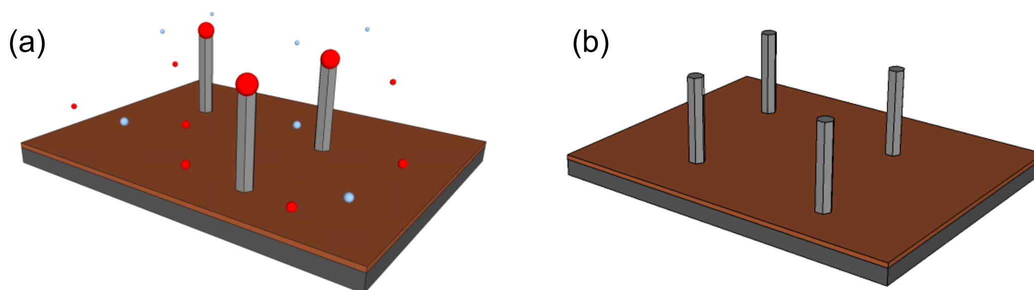

Figure 3.1. (a) Schematic of a self-induced, self-catalyzed VLS growth mechanism where the group-III element forms a liquid droplet prior to nanowire growth. In (b) a droplet-free, non-VLS growth mode is illustrated.

(Fig. 3.1b), which so far was successfully demonstrated during the spontaneous nucleation of nitride-based (GaN, AlN, InN) [Deb07, Cal07a, Cal07b, Con10, Che10, Lan10] and certain II–VI-based (ZnO) nanowires [Jeo10]. For III–As-based materials, however, various efforts have been undertaken to grow nanowires in a self-induced, spontaneous fashion but in nearly all cases self-catalyzed metal particles (i.e., droplets of the group III-element) were observed during growth [Cir10, Man10, Man06, Fon08a, Jab08]. Only a limited amount of reports demonstrate a facet-driven non-VLS growth of III–As nanowires using MOCVD [Nob05, Tom08]. Thus, it has remained unclear whether self-induced III–As based nanowires are fundamentally prone to obey a VLS growth mechanism or if sufficient investigations, in particular *in-situ* growth studies during self-induced nanowire growth, have been lacking.

3.2 In-situ nucleation analysis by RHEED

3.2.1 Self-induced InAs nanowire nucleation

A unique method to investigate the nanowire growth mechanism is *in-situ* RHEED. This method allows to monitor the nucleation characteristics and growth with very high (sub monolayer) precision, as routinely applied in thin film or quantum dot growth using MBE. For details about the RHEED technique see section 1.2. To proceed with specific RHEED experiments, wafer handling and nanowire growth is performed in the same way as described in detail in section 2.1. In particular, the InAs nanowires are grown in a self-assembled unordered manner on p-type doped Si(111) wafers covered with a 1–4 nm-thick, rf sputtered and wet chemically etched, amorphous SiO_x layer. It is important to note that for a sufficient intensity of the streaked RHEED diffractions emanating from the underlying Si(111) the final thickness of the SiO_x layer must not exceed $\sim$4 nm. For the experiments here, an In flux rate of 0.24 Å/s and As_4 BEPs of 2.6×10^{-6}, 5.2×10^{-6} and 10.4×10^{-6} mbar are employed. These conditions correspond to equivalent 2D growth rates of 1.51 Å/s, 3.02 Å/s and 6.04 Å/s (As/In ratio = 6.3, 12.6 and 25.2), respectively.

In Fig. 3.2 representative RHEED patterns taken along the $\langle 1\bar{1}0 \rangle$ azimuth, as well as the corresponding time evolution of Bragg spot intensity and the in-plane strain relaxation during InAs nucleation are depicted for one experiment performed with an As/In ratio of 12.6. The three RHEED patterns shown in Fig. 3.2a were taken consecutively from the recorded RHEED movie after 0 s, 4 s, and 10 s of InAs growth. Prior to growth the SiO_x/Si(111) substrate was exposed to the As flux, meaning that growth was initiated when the In shutter was opened (t = 0 s). The streaky RHEED pattern taken at t = 0 s is therefore

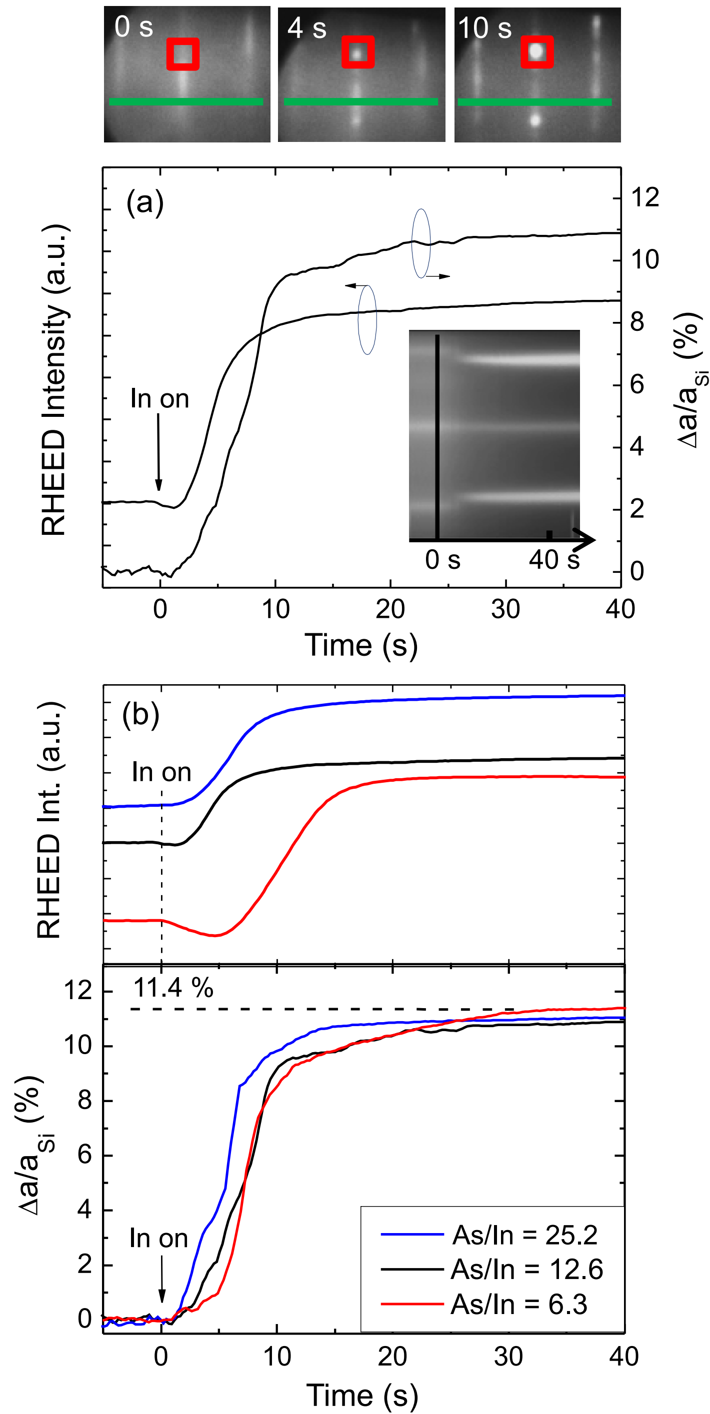

Figure 3.2. (a) Time evolution of the RHEED intensity and in-plane strain relaxation during InAs nanowire nucleation on Si(111) for an As/In ratio of 12.6. Three representative RHEED patterns are shown prior to growth (0 s), after 4 s and 10 s of growth. The red square and green line mark the regions for intensity and d-spacing analysis, respectively. (b) Time evolution of RHEED intensity and in-plane strain relaxation for different As/In ratios ranging from 6.3 to 25.2. Published in Ref. [Her11].

representative for the underlying 2D Si(111) surface morphology (see also section 1.2). As growth proceeds, three-dimensional (3D) (111)-oriented InAs islands start forming on the substrate indicated by an abrupt transition to a spotty RHEED pattern. Concurrent with the fast morphology transition from 2D substrate interface to 3D island growth an instantaneous increase was observed in the RHEED intensity of the InAs Bragg spot as taken from integrated intensity over the red square (illustrated in the respective RHEED patterns). Note that the increase in intensity occurred within the very first 1–2 seconds of InAs growth, corresponding to less than one monolayer (ML) of InAs (1 ML = 0.314 nm) for the given nanowire growth rate, or in terms of In coverage (Θ^{In}) only a fractional, i.e., negligible $\Theta^{\text{In}} < 0.05$ ML [1 ML(In) = 0.495 nm]. The growth rate here is given as the vertical nanowire growth rate along the (111) orientation, which is determined by the impinging As flux (compare with Fig. 2.10).

In addition, the d-spacing was analyzed by plotting the RHEED streak position as a function of time (inset of Fig. 3.2a) along a horizontal line indicated by the green bar. The distance of the two outer streaks was then measured by determining the position of the maximum intensity of the lines via numerical fitting. Subsequently, the distance of the streaks measured in pixel units was converted to real space nanometer units by calibration to the Si lattice constant (a_{Si} = 0.543 nm) as set prior to growth. The measured in-plane lattice constant evolution in Fig. 3.2a (right axis) illustrates the mismatch between the measured lattice constant a and a_{Si}. The results show a very similar time behavior to the intensity analysis, namely that with the relatively large lattice mismatch between InAs and Si ($\Delta a / a_{\text{Si}}$ = 11.6 %), the strain relaxation is very abrupt (within < 1 s of growth). As both abrupt changes in intensity and strain relaxation occur within the very first ML of growth, this indicates not only a very fast nucleation process, but also that there is apparently not sufficient time for droplet (metallic In) formation, as further discussed below.

RHEED intensity and strain relaxation were further investigated for different As/In ratios (Fig 3.2b). While for the low As/In ratio of 6.3 the onset for intensity increase and strain relaxation took approximately 4 s, these onsets occurred faster (< 1 s) for the highest As/In ratio of 25.2. This difference stems directly from the As-limited nanowire growth rate, i.e., larger As/In ratios yield faster growth rates as discussed in section 2.2.4. In consideration of this, the difference between the resolved onset times corresponds hence to always less than 2 MLs of nominally deposited amount of InAs (within accuracy of determination for the appearance of 3D features) – which is indicative of a very fast nucleation process over the entire As/In flux ratio range. This is in reasonable agreement with previous RHEED studies of the growth of Volmer-Weber (VW) like InAs nanoislands on Si surfaces [Cir99].

To ensure that the interpretation of the RHEED data of Fig. 3.2 is representative

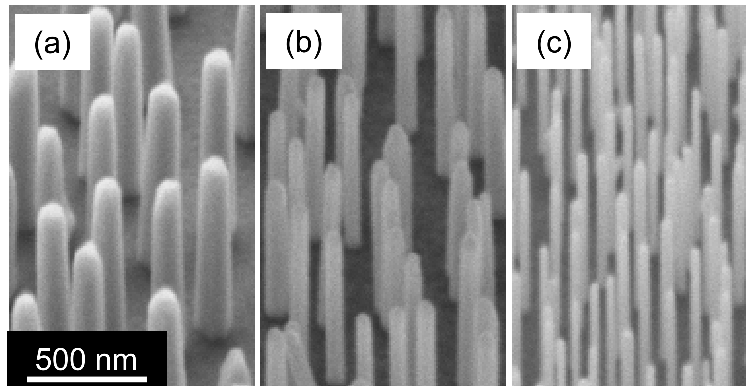

Figure 3.3. SEM micrographs of the RHEED-investigated InAs nanowires for different As/In ratios and growth times, namely (a) 6.3 (45 min), (b) 12.6 (22.5 min), and (c) 25.2 (12 min). All SEM micrographs clearly reveal a clean substrate surface in between the nanowires, i.e., there is no occurrence of clusters which may obscure the interpretation of the RHEED data. Published in Ref. [Her11].

for the nanowire growth mode, SEM images of the investigated samples with the As/In ratios (growth times) of (a) 6.3 (45 min), (b) 12.6 (22.5 min), and (c) 25.2 (12 min) are presented in Fig. 3.3. The growth times were adjusted to compensate different growth rates such that comparable nominal nanowire lengths were achieved. The SEM images show the characteristic nanowire morphologies as observed in previous experiments (see section 2.2). All SEM micrographs clearly reveal a clean substrate surface in between the nanowires, i.e., there is no occurrence of clusters which may obscure the interpretation of the RHEED data. The cluster-free surface was achieved mainly by using moderate In and As fluxes and short growth time. It is worth to mention that despite the apparently different nanowire aspect ratios, it is difficult to identify precise nanowire size- and density-dependent nucleation kinetics. This is because the time scale differences in the measured RHEED strain relaxation characteristics are marginal (1–4 s) among the three investigated samples (compare Fig. 3.2b). Nevertheless, based on the large lattice mismatch with the underlying substrate and the typical substrate wetting incapability in the presence of a thin SiO_x surface layer, InAs nanowire nucleation is suggested to obey the so-called Volmer-Weber island growth mode. After nucleation the islands undergo morphological transitions toward equilibrium crystal shape driven by Gibbs free energy minimization. This is corroborated by the absence of an InAs wetting layer on either clean [Lan10], oxidized (section 2.2) or nitrated Si [Cir99] and nanowire base diameters much larger than the critical radius ($\sim$5 nm) for coherent dislocation-free islanding [Cir99].

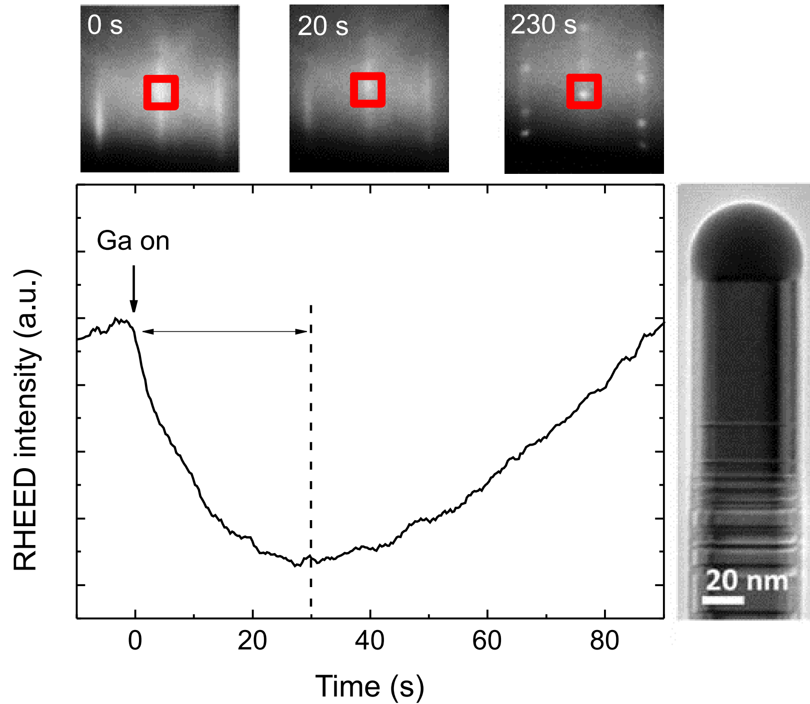

Figure 3.4. RHEED intensity evolution during GaAs nanowire nucleation on Si(111) for an As/Ga ratio of 5.9 and temperature of 630 ℃. A pronounced intensity decrease and substantial delay time after growth initiation was observed due to the formation of macroscopic Ga droplets and associated shadowing effects. The dashed line illustrates the point of intensity recovery, coinciding with morphology transition from streaky to spotty RHEED pattern due to the onset of nanowire formation. The TEM micrograph on the right clearly evidences the existence of a Ga droplet at the apex of self-induced GaAs nanowires.

3.2.2 Comparison with self-induced GaAs nanowire nucleation

Considerably longer nucleation times were found for material systems where nanowire growth obeys a self-catalyzed VLS growth mechanism. The control experiment illustrated in Fig. 3.4 shows the respective RHEED intensity evolution in the case of self-induced growth of GaAs nanowires, grown under similar conditions on Si(111), i.e., using a comparable ∼2 nm-thick SiO_x layer, As_4 BEP of 2.6×10^{-6} mbar and a Ga flux of 0.24 Å/s at 630 ℃ growth temperature, resulting in a vertical nanowire growth rate of 13 Å/s and a similar nanowire nucleation density.

A drastic decrease in RHEED intensity is observed, accompanied by a very long delay time (∼30 s) before the intensity recovers. The point of recovery (dashed line) coincides with the characteristic morphology transition from a low intensity-contrast (2D) streaky to a spotty (3D) RHEED pattern. The final GaAs nanowire morphology clearly evidences the existence of macroscopic Ga droplets at the nanowire apex, as confirmed by TEM

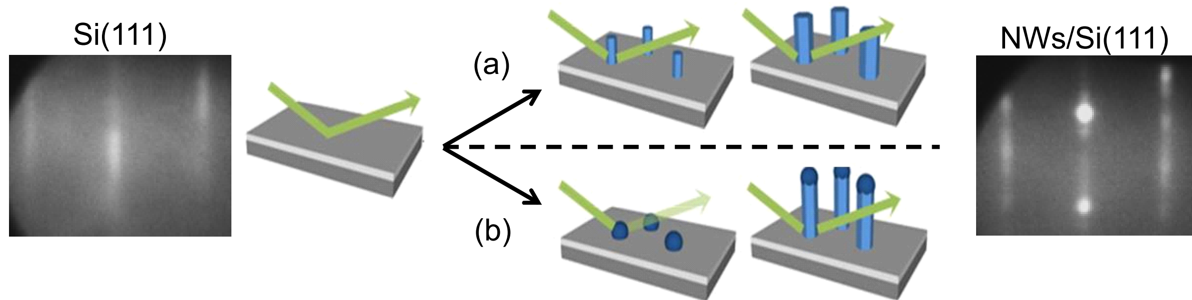

Figure 3.5. Schematic of the *in-situ* nanowire nucleation studies by RHEED for (a) catalyst-free and (b) vapor-liquid-solid nanowire growth, respectively. For catalyst-free nanowire growth an immediate increase in Bragg spot intensity is observed upon growth initiation, whereas in VLS growth liquid droplets obscure the RHEED signal leading to a decrease of intensity as observed in Fig. 3.4. Published in Ref. [Rud11].

micrographs (see inset) taken for this particular sample with nanowires grown to a length of ∼4 µm and a diameter of ∼50 nm. The substantial delay time and gradual intensity decrease at the beginning of GaAs growth is attributed to the formation of liquid Ga droplets at the surface, causing very strong shadowing effects for the diffracted RHEED intensity – a common observation for liquid droplet formation on single-crystalline substrates [Gal07]. This is further illustrated in Fig. 3.5, where a schematic of the RHEED measurements is shown for (a) the catalyst-free vapor-solid (VS) nanowire growth (InAs) and (b) the self-catalyzed VLS nanowire growth (GaAs). The illustration also shows respective RHEED patterns taken before growth (streaky Si(111) pattern) and after growth (spotty NW/Si(111) pattern). At the onset of nanowire growth 3D InAs islands form in the VS case (a) causing an immediate increase in intensity of the InAs Bragg spot as discussed above. The behavior in the VLS case (b) is very different since no island forms but instead liquid Ga droplets develop on the wafer surface. These droplets do not exhibit a defined crystal structure and hence no GaAs Bragg spot can be resolved. Furthermore, the droplets cover the underlying Si(111) wafer obscuring the RHEED signal leading to the intensity decrease measured in Fig. 3.4. After a certain delay time (∼30 s in this case) macroscopic Ga droplets are formed and GaAs starts to crystallize leading to an increase of intensity. For the given As/Ga ratio this delay time corresponds to a loss in nominal nanowire length of ∼40 nm (as calibrated from a growth rate series) – a value which is more than 50 times larger than for self-induced InAs nanowires with the same V/III ratio. This evidences the very different nucleation nature of self-catalyzed VLS nanowires (GaAs) versus the anticipated self-induced non-VLS nanowires (InAs).

3.3 Post-growth investigation of InAs nanowires

In addition to *in-situ* RHEED investigations specific *ex-situ* analytical methods, such as SEM (Zeiss *NVision 40*) and TEM (FEI *Titan* 80–300 kV) were employed to further corroborate the dominant growth mechanism via morphological investigations.

3.3.1 SEM analysis

First, the SEM images showing the InAs nanowires used for RHEED investigation (Fig. 3.3) will be discussed in more detail. For all three samples, growth was terminated identically, i.e., by closing the In supply and quenching the temperature, while the As-shutter remained open during cool-down. In agreement with the results in chapter 2 In droplets were not observed at the apex of the nanowires. The nanowire length L, diameter D, and density ρ obtained from a statistical analysis of SEM images for the three samples are listed in Table 3.1. The tendency for larger ρ with increasing As/In ratio can be attributed to suppressed surface migration lengths as previously reported in section 2.2.4, and was further observed for growth of 3D InAs nanoislands on Si [Cir99].

Table 3.1. Nanowire length L, diameter D, and density ρ for three different As/In ratios (growth times) of 6.3–25.2 (45–12 min).

As/In	t (min)	L (nm)	D (nm)	ρ (µm^{-2})
6.3	45	531 $\pm$ 13	95 $\pm$ 13	15
12.6	22.5	413 $\pm$ 15	66 $\pm$ 8	25
25.2	12	391 $\pm$ 25	32 $\pm$ 4	50

Interestingly, despite the significant variation in nanowire diameter among these samples, all nanowires exhibit non-tapered geometries with tapering factors of less than 2.5 %, independent of the As/In ratio. The tapering is defined as $(D_{\text{bottom}} - D_{\text{top}})/L$ with the length L and the nanowire diameters at the bottom (D_{bottom}) and the top (D_{top}), respectively. Considering the rather large variation in As/In flux ratio, maintaining such equilibrium morphology throughout the nanowire is another indication that growth is not governed by a VLS growth mode. In contrast, for self-catalyzed VLS-grown III–As-based nanowires such independence of tapering on V/III ratio could not be observed – i.e., with decreasing V/III ratio the nanowire morphology changed gradually from tapered or non-tapered to inverse tapered nanowires [Pli10, Col08]. In more detail, Colombo et al. studied the tapering of self-catalyzed GaAs nanowires on GaAs(111)B substrates for a fixed As flux and temperature. The Ga flux was varied from 0.12 Å/s to 0.82 Å/s making a significant impact on the tapering,

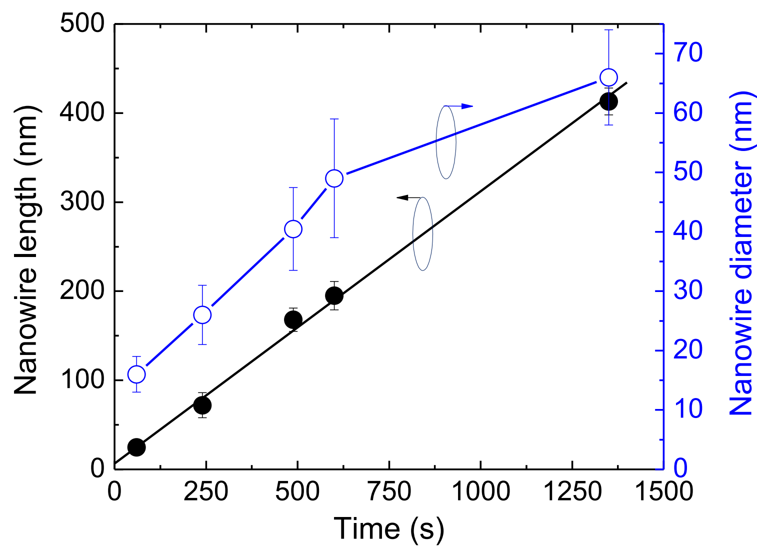

Figure 3.6. InAs nanowire length and diameter as a function of growth time for a series of five different samples grown with an As/In ratio of 12.6. The nanowire length shows a linear growth behavior for the investigated growth times of 60 s to 22.5 min and reveals absence of any delay time in nanowire growth. The given error-bars represent the standard deviation of ten nanowires per sample. Published in Ref. [Her11].

i.e., for lower Ga fluxes straight nanowires were found while for higher fluxes increased inverse tapering factors up to ~12 % were reported. The inverse tapering stems directly from the Ga droplet involved in the VLS mechanism, i.e., for higher Ga fluxes the droplet grows over time resulting in increasing nanowire diameter for increasing growth time. In the case of InAs nanowires no sample with inverse tapered wires has ever been observed, neither in this As flux study nor in the In flux study discussed in chapter 2.2.4. Moreover, the nearly instantaneous onset of InAs nanowire growth as evidenced during *in-situ* RHEED studies is furthermore reflected by *ex-situ* growth time dependence analysis (Fig. 3.6). Using SEM measurements the evolution of nanowire length as a function of growth time (60 s to 22.5 min) is deduced for a fixed As/In ratio of 12.6. A best fit to the data points shows a linear length behavior (linear axial growth rate Φ^{axial} = 3.1 Å/s) without any significant delay in nanowire nucleation. In contrast, a huge delay time of ~4 min was observed for Ga-assisted, VLS-grown GaAs nanowires on GaAs substrates utilizing an identical SiO_x mask layer and identical As-limited growth rates (~3 Å/s) [Fon08a]. Furthermore, the axial nanowire growth rate deduced from Fig. 3.6 (3.1 Å/s) is again very similar to the supplied 2D As rate (2.8 Å/s). These findings – which have already been observed earlier in section 2.2.4 – are a strong indication for a non-catalytic nanowire growth. In contrast, liquid catalysts leading to VLS growth enhance Φ^{axial} to values significantly larger than the supplied 2D

equivalent As flux [Jab08, Che10, Rud11]. In Fig. 3.6 also the nanowire diameter is plotted as a function of growth time (blue curve with open circles) revealing a relatively large radial growth rate, i.e., $\sim$0.5–1 Å/s (merely a factor of 3–6 lower than the axial growth rate). In contrast, VLS-grown nanowires show rather negligible radial growth rate, suggesting that growth proceeds predominantly through the metal catalyst to enhance vertical growth as observed for GaAs and GaN nanowires [Col08, Che10]. Interestingly, the radial nanowire growth rate is constant for the first $\sim$10 min of growth and decreases significantly for t > 10 min. This finding explains well the nanowire volume evolution (derived from this data) as shown earlier in Fig. 2.7, where a transition from super-linear to linear increase of volume was observed for t $\sim$500–600 s.

3.3.2 TEM analysis

To further investigate the absence of metallic In droplets high-resolution TEM was performed at selected samples for different growth termination procedures using As/In ratios of 12.6 (Fig. 3.7b) and 6.3 (Fig. 3.7a, c) resulting in low growth rates of 3.1 Å/s and 2.0 Å/s.

Figure 3.7a is a TEM image taken from a representative InAs nanowire dispersed onto a copper grid covered with a holey carbon film, showing typical alternating wurtzite (WZ)/ zincblende (ZB) stacking faults throughout the entire nanowire. A discussion of the crystal structure would go beyond the scope of this chapter and will be discussed in chapter 4. To be sure which side of the nanowire is top and bottom, high resolution SEM images were taken from the as-grown nanowires (still attached to the substrate) exhibiting the nanowire top to be faceted over the final $\sim$30 nm of the wire. Hence, the top of the nanowire is located on the left hand side in Fig. 3.7a, whereas the bottom is found to be straight. In Fig. 3.7b a magnified image of the near nanowire tip region is presented for the case when InAs nanowire growth was terminated by closing the In-shutter and quenching the temperature with remaining As flux. The micrograph reveals an atomically abrupt interface at the nanowire apex without any In droplet visible.

However, it still needs to be proved that it is impossible that a liquid droplet was governing the growth and may have vanished afterwards. Hypothetically, two effects could play a role, i.e., (i) thermal evaporation of an In droplet at growth temperature and (ii) further InAs nanowire growth consuming the In droplet (since the As shutter is still open). Argument (i) can easily be ruled out since the onset temperature of In desorption from a liquid In reservoir was determined to T $\sim$550 °C [Kob07] – much higher than the applied temperatures in this study. Hence, no post-growth evaporation of In could have occurred in case an In droplet was present. For argument (ii) another growth run was performed with a different

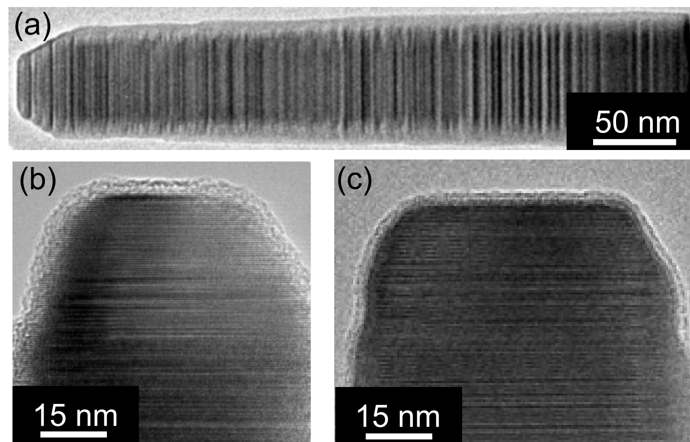

Figure 3.7. (a) TEM image of a representative InAs nanowire with typical stacking faults. Magnified images of the nanowire apex region are furthermore presented for a growth time of 45 min with an As/In ratio of 12.6 (b) and 6.3 (c) under different growth termination procedures. (b) Growth was ended by closing the In-shutter and quenching the temperature under remaining As flux during cool-down, while in (c) the In- and As-shutters were closed simultaneously. Published in Ref. [Her11].

shut-down procedure, i.e. growth was terminated by simultaneously closing the In- and As- shutter. Figure 3.7c shows the nanowire tip for the latter growth experiment providing evidence of a droplet-free, atomically flat nanowire apex. For this experiment it is important to note that within a short 2 s time frame after shut-down (corresponding to an upper bound for additional nanowire growth of only 4 Å) a parameter regime was reached where InAs nanowire growth is not possible (As flux $< 3 \times 10^{-7}$ mbar). That means even if a liquid In droplet had been involved in the growth it would have not been consumed due to the lack of As in the chamber. The fact that there is no liquid droplet visible in Fig. 3.7c proves once more the catalyst-free growth regime.

It is further noted, that in closer view, both images show a homogeneously $\sim$2–3 nm-thick high-contrast amorphous layer at the perimeter of the entire nanowire, which can be associated with a native In_2O_3 layer resulting from exposure to ambient air [Wer09].

3.4 Growth interruption experiments

In addition, another nanowire growth was performed under identical conditions as reported in Fig. 3.3b (As/In ratio = 12.6). However, this time the nanowire growth was interrupted by shutting off the In supply (under remaining As flux) for 2 min after 11 min of growth and subsequently growing the remaining 11.5 min (see Fig. 3.8 for illustration). This

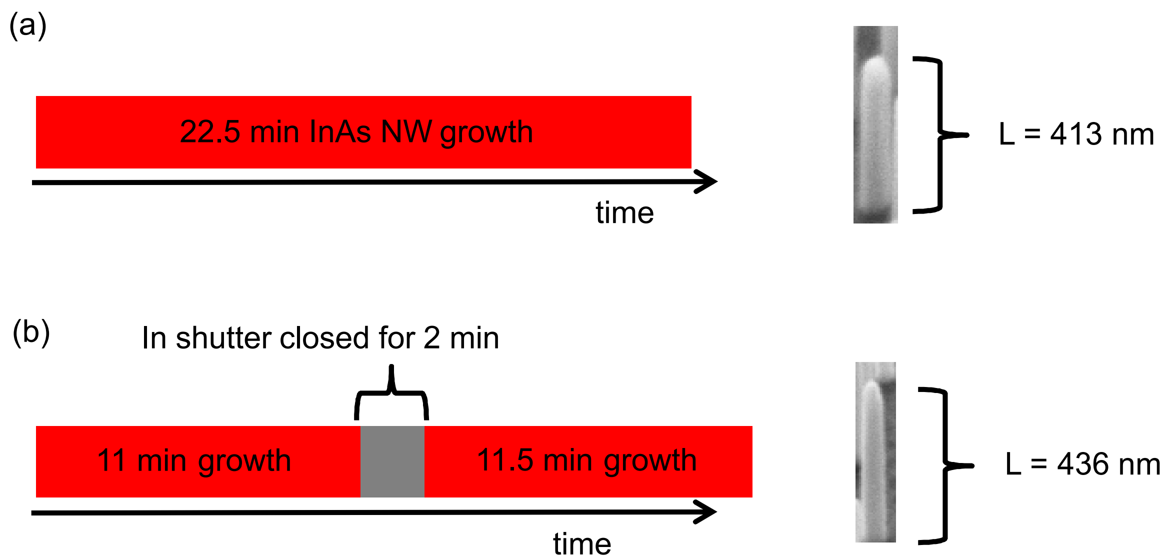

Figure 3.8. Schematics of the growth interruption experiment. The nanowire lengths of the reference sample (grown for 22.5 min) were compared with the nanowire lengths of a growth-interrupted sample with 11 min of nanowire growth followed by a 2-min break and subsequent 11.5 min of growth. During the interruption the In shutter was closed while As and temperature were unaltered. SEM micrographs reveal identical lengths of 413 nm $\pm$ 15 nm and 436 nm $\pm$ 43 nm for the growth-interrupted and the reference sample, respectively.

procedure yielded identical nanowire lengths (within typical errors) of L = 436 nm $\pm$ 43 nm, as compared to L = 413 nm $\pm$ 15 nm for the continuously grown reference sample (3.3b). In contrast, recent literature on self-catalyzed VLS-grown InAs nanowires reported significantly shorter nanowires with complete growth termination during growth interrupts due to consumption of liquid In droplets [Man10]. Hence, the identical nanowire lengths observed in the present study support the previous findings that no In droplet forms prior or during nanowire growth corroborating the catalyst-free VS growth mode.

3.5 Conclusion

In conclusion, various nanowire growth modes were discussed in detail, such as vapor-liquid-solid growth (with liquid catalyst) and vapor-solid growth (without catalyst), and the dominant growth mechanism was derived for InAs nanowires. In particular, a VLS-free growth mechanism for self-induced InAs nanowires on Si(111) was demonstrated using a combination of *in-situ* RHEED and *ex-situ* SEM and TEM investigations. Both the abrupt increase in RHEED intensity and strain relaxation evidence the absence of self-formation

of liquid In droplets prior to nanowire growth, independent of the supplied As/In flux ratio. A direct comparison with RHEED data of self-catalyzed (VLS) GaAs nanowires grown on Si support this finding. The catalyst-free growth mode for InAs nanowires was further confirmed by the absence of residual In droplets at the nanowire tip even for different growth termination procedures. Further evidence was provided by the non-tapered nanowire geometries over the full range of investigated As/In ratios and growth-time dependent studies with no measurable delay in nanowire growth. Moreover, In supply interruptions under remaining As pressure showed no effects on the nanowire lengths, in contrast to VLS grown nanowires.

4

Microstructure and optical properties of InAs nanowires

In this chapter the microstructure and optical properties of InAs nanowires are investigated. In terms of microstructure the effects of As/In ratio and growth temperature are analyzed using HRXRD and TEM, revealing detailed insights into the predominant layer stacking of catalyst-free InAs nanowires. In addition, optical properties by means of low-temperature PL spectroscopy are presented and the near-band-edge emission is analyzed for wurtzite-dominated InAs nanowires. In addition, diameter-dependent emission properties are elucidated and the role of radial quantum confinement for very thin nanowires displayed. Parts of this chapter are published in Ref. [Kob12].

4.1 Structural properties of InAs nanowires

Two specific InAs nanowire sample series were grown for microstructure analysis, namely, (i) an **As flux series** and (ii) a **growth temperature series**. All nanowires were grown on a SiO_x/Si(111) substrate in a self-assembled manner as reported in detail in section 2.1. Sample series (i) was grown with fixed growth temperature of 500 ℃ and In flux of 0.36 Å/s using three different As fluxes yielding As/In ratios of 24.2, 56.5 and 80.7. Apart from the growth time, the nanowire growth conditions are identical with according samples shown in Fig. 2.10. Note that here the nanowires were grown with increased growth times of 90–140 min yielding nanowire lengths of $\sim$4–5 µm. The extended nanowire lengths facilitate additional electrical measurements which were performed in two associated diploma theses [For11, Ges12]. The nanowire diameters for the series presented here are in the range of $\sim$90–130 nm with decreased diameter for higher As fluxes as also found in section 2.2.4. For detailed information on the nanowire dimensions and growth parameters see Table 4.1. According to the results presented in Fig. 2.10 the nanowires were grown in the In-rich growth regime (V/III ratio of 24.2) and in the As-rich growth regime (As/In ratio of 56.5 and 80.7). This allows direct evaluation of different surface kinetic influences on the nanowire crystal quality. In Fig. 4.1a–c representative SEM micrographs of the three samples from series (i) are shown for increasing As fluxes as indicated at the bottom of each image. In agreement with previous findings an increasing volume of InAs clusters is observed for increasing As fluxes. Fig. 4.1d–f shows SEM micrographs of InAs nanowires from sample

Table 4.1. Growth parameters [As/In ratio, growth temperature (T), growth time (t)] and dimensions [nanowire length (L) and diameter (D)] of nanowire samples from both an As flux series (a–c) and a growth temperature series (d–f) are presented. Selected nanowires from these sample series are taken for structural investigations.

Sample	As/In	T (℃)	t (min)	L (nm)	D (nm)
a	24.2	500	140	3767 ± 509	134 ± 16
b	56.5	500	90	5675 ± 1178	115 ± 13
c	80.7	500	90	5130 ± 1411	91 ± 28
d	33.9	430	24	723 ± 222	43 ± 2
e	33.9	490	24	931 ± 49	47 ± 6
f	33.9	530	24	580 ± 99	62 ± 5

series (ii) which was grown for fixed V/III ratio of 33.9, fixed growth time of 24 min, and varying growth temperatures of 430 ℃ (d), 490 ℃ (e) and 530 ℃ (f). These samples are identical with those investigated for the InAs growth parameter study in section 2.2.2. As already discussed previously a significant change in nanowire length, diameter and density

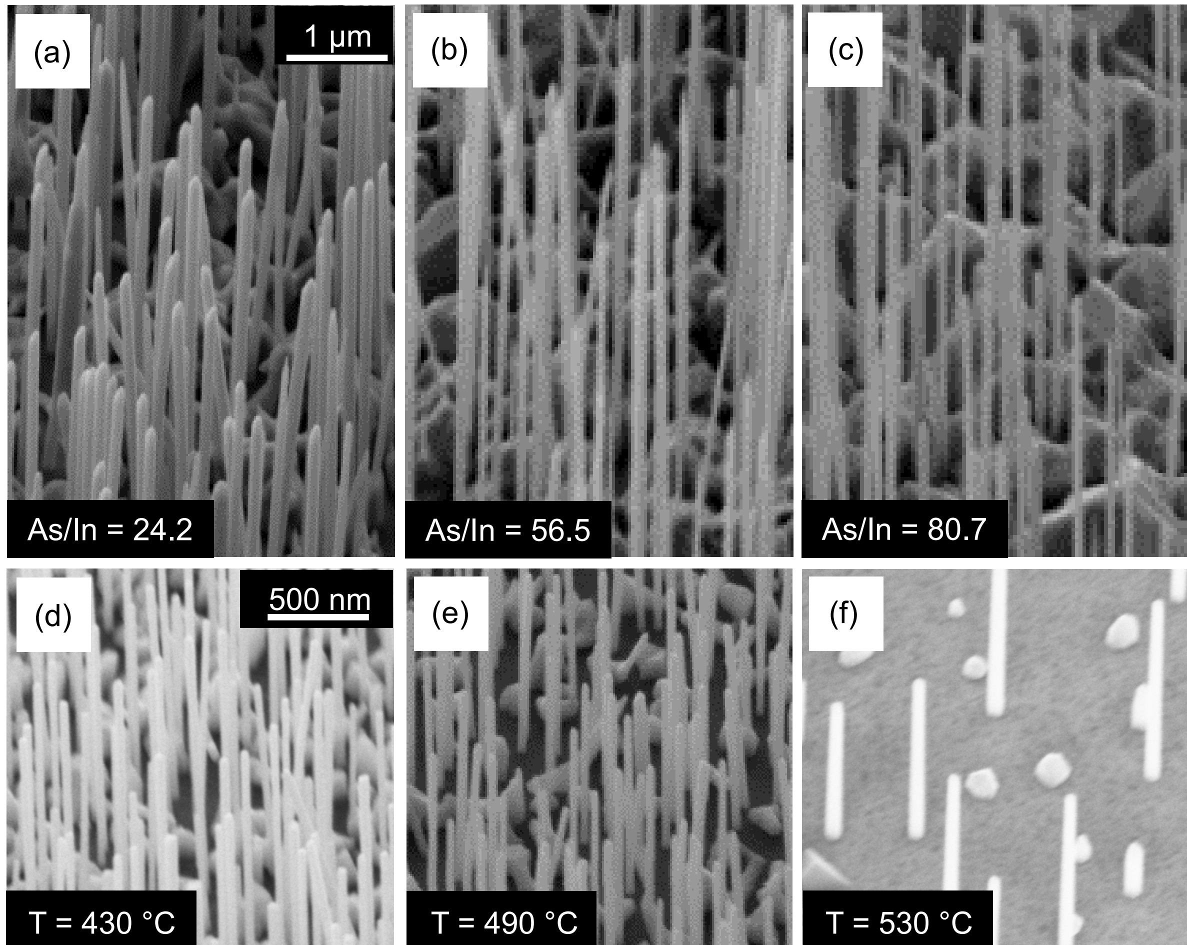

Figure 4.1. SEM micrographs of InAs nanowires grown in a self-assembled manner on a SiO_x/Si(111) substrate. Two sample series are shown, i.e., an As flux series grown with a fixed growth temperature of 500 °C and As fluxes of 8.71 Å/s (a), 20.33 Å/s (b) and 29.04 Å/s (c) yielding V/III ratios of 24.2, 56.5 and 80.7. A second series was grown using a fixed V/III ratio of 33.9, a fixed growth time of 24 min, and varying growth temperatures of 430 °C (d), 490 °C (e) and 530 °C (f). Scalebars for the upper panel (a–c) are all 1 µm and for the lower panel (d–f) 500 nm.

is observed. The most obvious trend is the reduction of nanowire density and increase of diameter for high growth temperatures (see Fig. 4.1f). Further information about the nanowires are given in Table 4.1.

HRXRD and TEM analysis of selected nanowires from these two series will be presented in the following sections. Note that HRXRD was measured on as-grown nanowires free-standing on the Si(111) substrate while the TEM measurements were conducted on transferred nanowires. Hence, a careful evaluation of the HRXRD spectra is mandatory due to recording both InAs nanowires and clusters.

4.1.1 Transmission electron microscopy

The crystal structure of bulk InAs is zincblende (ZB), a cubic close packed (ccp) structure which can be understood as two face centered cubic lattices shifted along the body diagonal by one quarter of the lattice constant. The layer stacking of ZB structures is ABCABC. In InAs nanostructures, however, a second type of crystal structure is often observed, namely the wurtzite (WZ) structure [Kog92, Tom07a, Ihn07b, Buk09, Joh10]. This is a hexagonal close packed (hcp) structure determined by the two lattice constants a_{WZ} (in-plane) and c_{WZ} (along the [001] direction) with ABAB layer stacking.

For analysis of the crystal structure the nanowires were transferred from the as-grown wafer to carbon coated Cu grids. In detail, a small piece of the wafer is submerged in an isopropanol (IP) solution and treated by ultrasound which leads to a breaking of the nanowires. The IP/nanowire solution is subsequently drop-casted onto the TEM grid where the IP evaporates quickly. For TEM analysis of selected single nanowires a TEM *Titan* (300 kV) and a JEOL *2011* (200 kV) are used. It is important to mention that for all analysis the electron beam (zone axis) is perpendicular to the growth direction and perpendicular to one of the $\{110\}$ nanowire side facets. This is important since for other specific zone axes (e.g. a zone axis pointing to a corner of the nanowire) the WZ and ZB selected area electron diffraction (SAED) patterns are identical, i.e. it is impossible to distinguish between WZ and ZB structure.

Field-emission TEM images are shown in Fig. 4.2 with atomic resolution in low (a_1–c_1) and high (a_2–c_2) magnification of representative single InAs nanowires grown with different As/In ratios of 24.2 (a_1–a_3), 56.5 (b_1–b_3) and 80.7 (c_1–c_3). The magnified TEM micrographs show a zoom-in of the area marked by red squares in the low magnification images. The micrographs reveal a heavily disordered nanowire crystal stacking with stacking faults occurring every few monolayers along the growth direction. A stacking fault is caused by an interruption in the layer sequence, i.e., for ZB structure after an ABC sequence not an A-layer follows but a B- or C-layer. In the TEM images these stacking faults occur as stripes (also called lamellar defects) which are perpendicular to the growth direction. The heavily disordered structure of the InAs nanowires is especially evident in the magnified images (a_2–c_2) in which the stacking order is indicated by colored lines in red (WZ), green (ZB a) and blue (ZB b). ZB a and ZB b are rotated 60° to each other and their junction is referred to a rotational twin. The longest segments are WZ phase ranging over $\sim$7 monolayers (i.e. $\sim$3–4 nm). Interestingly, the observations do not show a significant dependence on the As/In ratio meaning that qualitatively similar occurrence of stacking faults are observed for these investigated growth conditions.

This finding is further corroborated by selected area electron diffraction (SAED) recorded

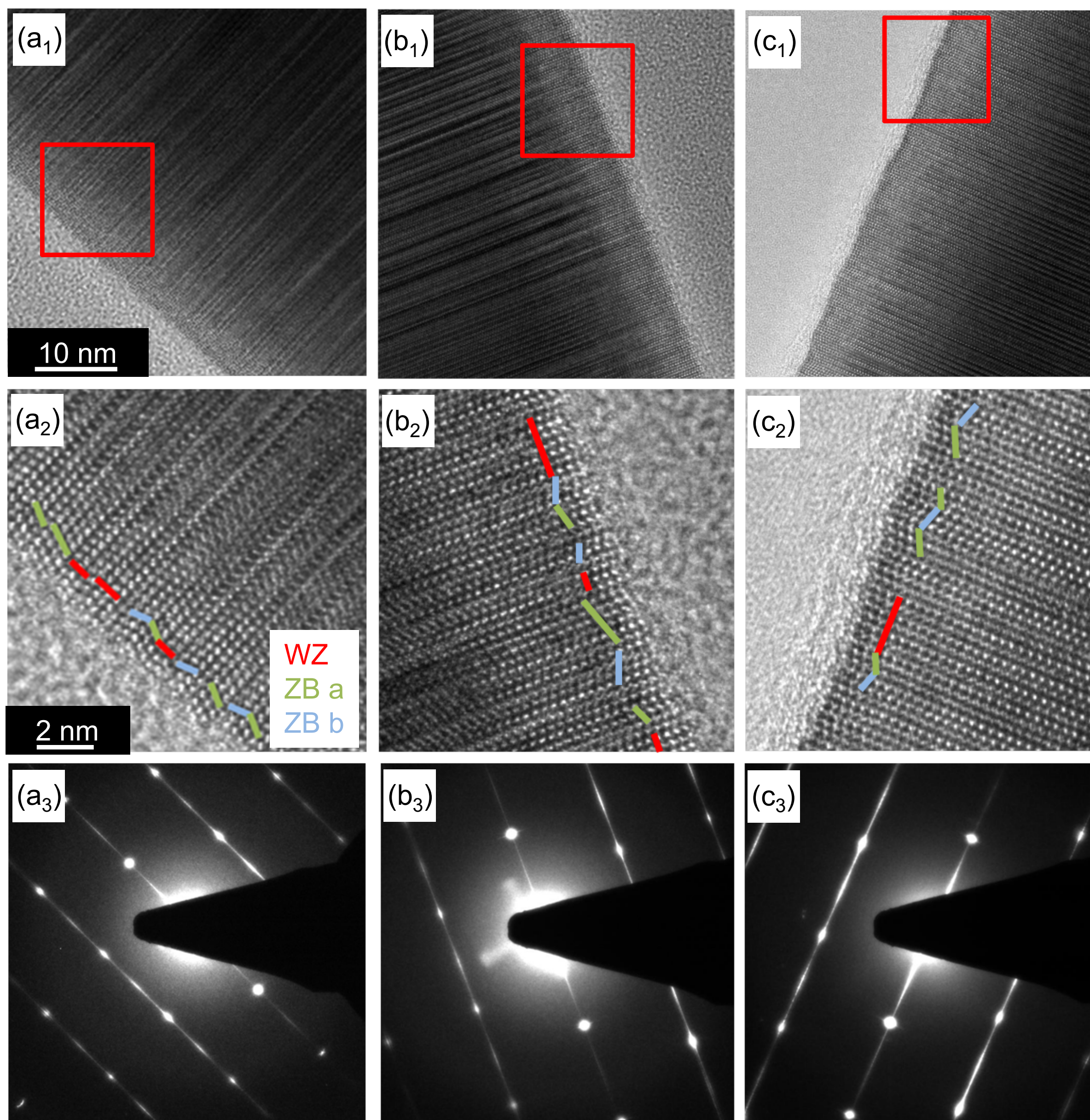

Figure 4.2. Representative TEM micrographs and SAED patterns of single InAs nanowires taken from samples grown with As/In ratios of 24.2 (a_1–a_3), 56.5 (b_1–b_3) and 80.7 (c_1–c_3). The images in the first panel (a_1–c_1) show a smaller magnification of one selected nanowire of each sample. A magnified image of the region marked by the red boxes is shown in the second panel (a_2–c_2). The type of stacking sequence is indexed using colored lines with red for WZ and green and blue for ZB stacking (ZB a and ZB b are rotated 60° to each other). A disordered crystal structure is observed exhibiting some few-nm-long WZ segments. Note that no clear qualitative differences between the nanowire samples could be observed. (a_3–c_3) SAED patterns show similar disordered WZ crystal structure for all investigated nanowires. See Fig. 4.3 for indexing of selected reflections.

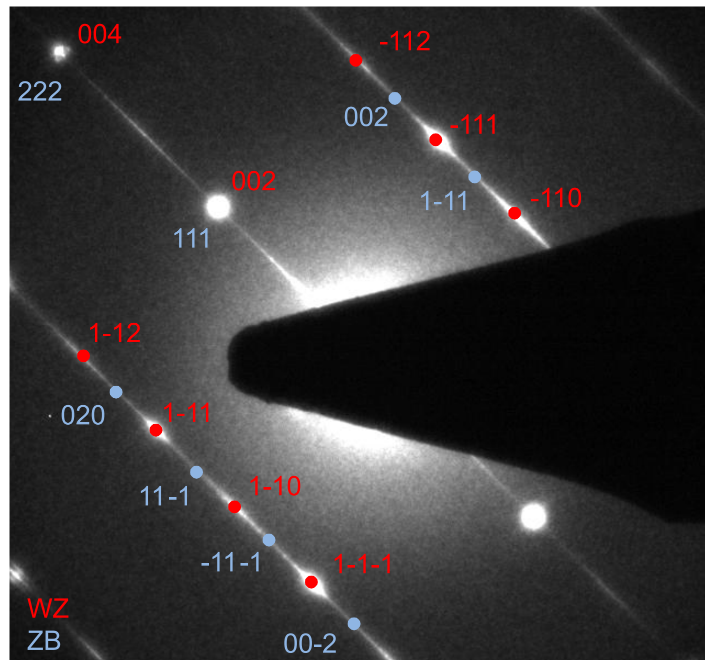

Figure 4.3. Magnified image of the SAED pattern shown in Fig. 4.2a_3 for the InAs nanowire sample grown with As/In ratio of 24.2. The WZ and ZB reflections are indexed in red and blue letters, respectively. Note that certain reflections are identical for both crystal structures, e.g. 002 $\widehat{=}$ 111, which means that these reflections are not suitable for structural characterization. The relatively bright WZ reflections (see for example -111) compared to the much lower intensities of ZB reflections (002 or 1-11) indicate that the nanowires exhibit predominant wurtzite crystal structure. However, the reflections are smeared out which is typically observed for a disordered crystal structure, i.e., WZ/ZB stacking faults or rotational twin defects.

from the entire nanowires and shown in a_3–c_3. For a better understanding of the SAED patterns a magnification of Fig. 4.2a_3 (As/In ratio = 24.2) is shown in Fig. 4.3, where the main WZ and ZB reflections are indexed in red and blue letters, respectively. The position of the reflections indicating the growth direction is identical for the ZB and WZ structure (002 $\widehat{=}$ 111), which means that these reflections give no information about the predominant crystal structure. Other reflections, however, are unique traces of one of the crystal structures, e.g. the -111 reflection for WZ stacking and the nearby 002 and 1-11 reflections for ZB stacking. The WZ-related -111 reflection is much brighter than the ZB-related reflections in its vicinity indicating a predominant WZ structure in the nanowire. However, the reflections are smeared out which is typically observed for disordered crystal structure [Tom07a, Li11c, Rud11]. This situation is evident for all three investigated nanowire samples as can be seen in Fig. 4.2. In all cases similar streaky diffraction patterns are observed with predominant WZ reflections indicating a disordered WZ structure for all investigated As/In ratios.

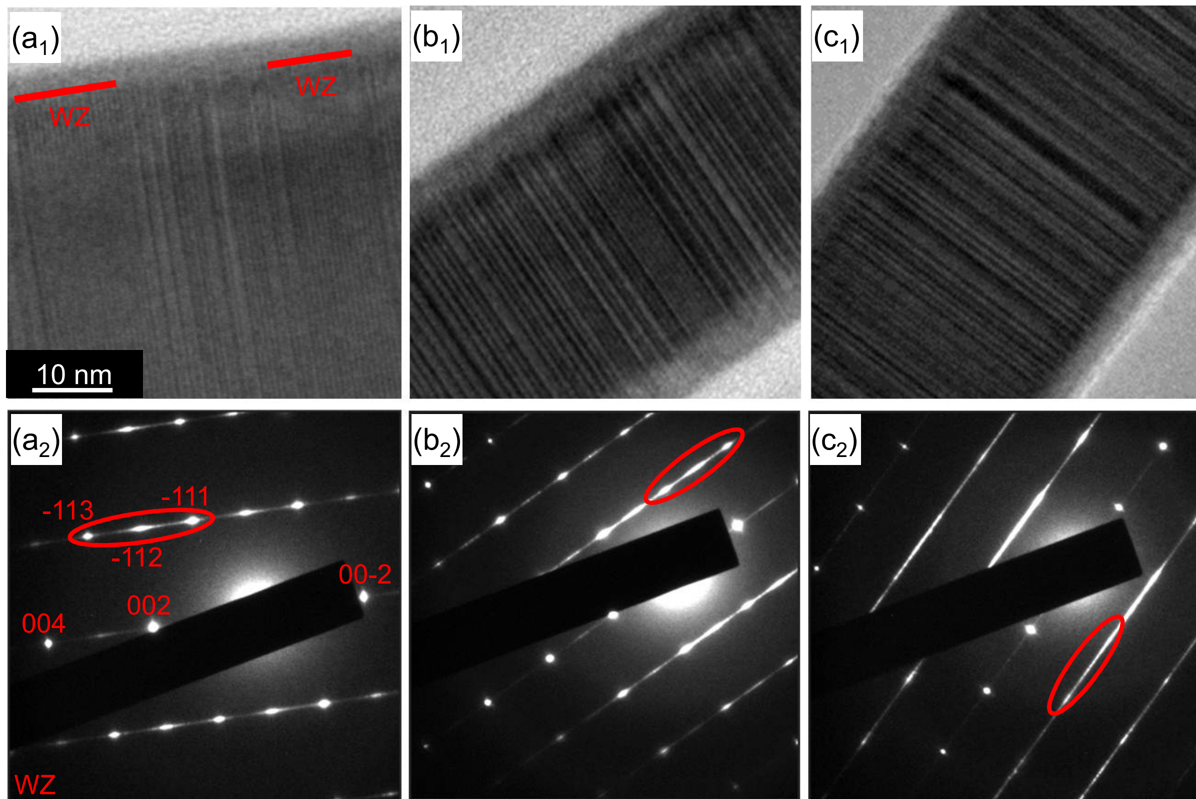

Figure 4.4. TEM micrographs (a_1–c_1) and SAED patterns (a_2–c_2) of InAs nanowires grown with fixed As/In ratio of 33.9, fixed growth time of 24 min, and varying growth temperatures of 530 ℃ (a_1–a_2), 490 ℃ (b_1–b_2) and 430 ℃ (c_1–c_2). A clear tendency of larger phase pure WZ segments with increasing growth temperature is observed in both TEM micrographs and SAED patterns.

A similar TEM investigation was performed for a growth temperature series analyzing selected single nanowires grown with parameters as given in Table 4.1. TEM images and according SAED patterns are shown in Fig. 4.4 for nanowires grown at different temperatures of 530 ℃ (a_1–a_2), 490 ℃ (b_1–b_2) and 430 ℃ (c_1–c_2). The TEM images are of lower quality than the images shown in Fig. 4.2 because a different microscope was used (JEOL *2011*) with a lower maximum acceleration voltage of 200 kV. Despite the lower resolution a clear tendency of longer WZ segments for higher growth temperatures is evident. In more detail, for the nanowires grown with 530 ℃ WZ segments with a length of up to >10 nm are observed, while the maximum WZ segment lengths for the nanowires grown at 490 ℃ and 430 ℃ are significantly shorter (2–5 nm). The according SAED patterns underline this observation and show clear WZ spots only for the nanowires grown with the highest temperature of 530 ℃ (a_2). Here, selected WZ reflections are indexed and three of them enclosed by an red oval. For direct comparison, the according reflections are

also marked in the SAED patterns of the nanowires grown at lower temperatures. The WZ reflections in the SAED pattern of the nanowires grown at 490 ℃ can still be identified but they heavily overlap with the nearby ZB reflections as discussed above. This leads to a streaky image indicating a more disordered crystal structure as compared to the nanowires grown at 530 ℃. Finally, the lowest growth temperature of 430 ℃ results in a SAED pattern in which the WZ reflections cannot be indexed due to a heavily disordered crystal structure without or with very short (<3 nm) segments (see Fig. 4.4c_2).

Although the increase in growth temperature results in longer phase pure WZ segments the influence is yet rather low and complete structural control toward pure WZ or pure ZB phase is still lacking. This seems to be a typical behavior for catalyst-free (111)B-oriented nanowires as shown by various other reports [Tom07a, Tom08, Rud11]. One of the reasons for the formation of stacking faults seems to be the nanowire diameter dependent difference in free energy per atomic pair (E_{free}) between WZ and ZB nanowires. In Ref. [Buk09] ΔE_{free} is calculated for InAs and GaAs nanowires using methods based on the density functional theory. It is shown that ΔE_{free} decreases significantly for increasing nanowire diameter. In detail, for nanowires with diameters smaller than $\sim$10 nm the WZ structure is more stable and hence it should be possible to grow nanowires with pure WZ structure without stacking faults. For nanowires with diameters >10 nm ΔE_{free} is in the range of only a few meV – which is much lower than kT – resulting in the formation of stacking faults. It is noted that the theoretical considerations in Ref. [Buk09] are further supported by Au-catalyzed growth of InAs and GaAs nanowires showing the expected behavior, i.e., pure WZ structure for nanowire diameters of 10 nm and an onset of stacking fault formation for nanowire diameters of 35 nm. Despite this, in VLS grown nanowires influence on the crystal structure has been shown for various III–As nanowire growth [Spi09, Dic10, Joh10, Bol11]. Here, the crystal structure seems to be easier addressable due to the specific VLS growth mechanism and the related nucleation at the triple phase line where WZ was found to be favored for high liquid supersaturation [Gla07]. In catalyst-free III–As nanowire growth, however, control of the crystal structure seems to be difficult [Tom07a, Rud11] and detailed understanding of the nucleation mechanism is still lacking.

4.1.2 High resolution X-ray diffraction

HRXRD analysis was conducted on the as-grown nanowire samples from the As flux series presented in Fig. 4.1a–c. Out-of-plane symmetric HRXRD 2θ–ω scans were measured in a Philips *X'pert Pro MRD* setup using the Cu K_α transition as X-ray source (λ = 0.15418 nm). Prior to data acquisition the system parameters were calibrated to the intense Si(111)

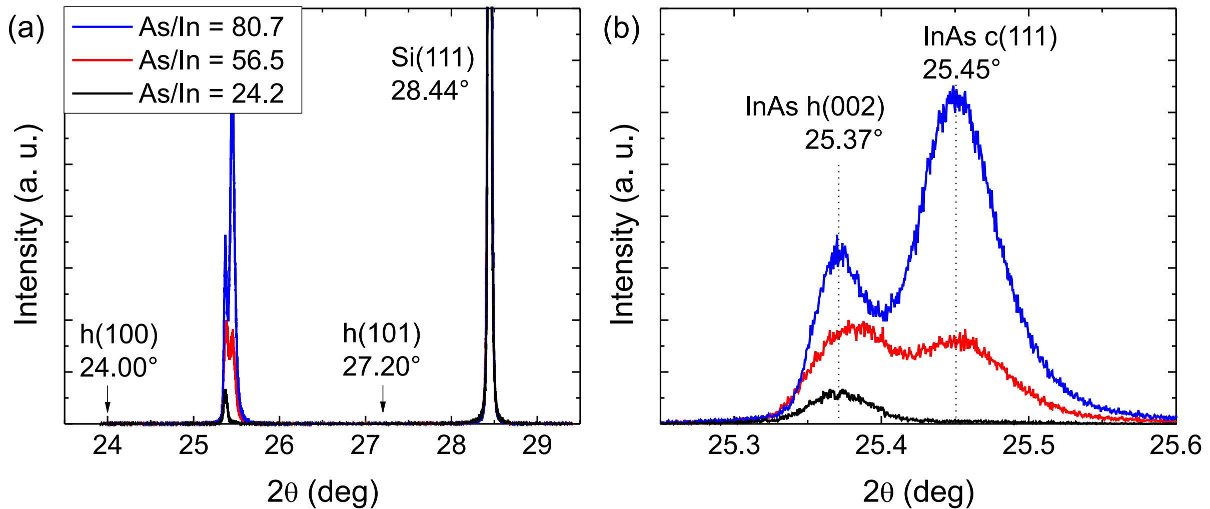

Figure 4.5. Out-of-plane symmetric HRXRD 2θ–ω scans of InAs nanowires grown with different As/In ratios (As flux series). The data is shown over 2θ ranges from 24° to 29° (a) and magnified to the InAs-related reflection from 25.2° to 25.6° (b). The InAs-related peak exhibits a clear substructure, i.e., a peak associated with the WZ(002) reflection at 25.37° and a second peak associated with the ZB(111) reflection at 25.45°. It is suggested that the WZ(002) reflection stems from the InAs nanowires and the ZB(111) reflection has its origin in InAs clusters which form mainly for high As/In ratios.

reflection at 28.44°. All scans were performed with a 1/8° aperture at the detector, an integration time of 4 s per step, and a stepsize of 0.0005°. The X-ray beam size of the setup is ∼3 mm x 4 mm on the sample surface.

Fig. 4.5a shows a 2θ–ω scan over a 2θ range of 24–29° with two significant 2θ peaks associated with InAs at around 25.4° and Si(111) at 28.44°. A closer view on the InAs related peaks reveal a distinct substructure as can be seen in Fig. 4.5b showing a magnified view of the same measurement. In particular, two peaks at 2θ = 25.37° and 2θ = 25.45° are resolved for the higher As/In ratios of 56.5 and 80.7. A comparison to the literature suggests an association with the hexagonal WZ h(002) and the cubic ZB c(111) crystal structure for the peaks at 25.37° and 25.45°, respectively (see Refs. [Tak66, Car08]). This is furthermore in very good agreement to calculations performed via the crystallographic software *CaRIne* yielding 25.36° and 25.44° for the respective peaks. For the sample grown with the lowest As/In ratio of 24.2, only the WZ-related peak at 2θ = 25.37° is observed. Interestingly, no other reflections beyond the h(002) and c(111) reflection could be resolved (see Fig. 4.5a).

Analysis of the relative intensities of the WZ and ZB reflections reveal the tendency of increasing intensity of the ZB peak for higher As/In ratios. Taking the SEM images of this

particular sample series into account (see Fig. 4.1a–c) one can see that more parasitic growth, i.e., InAs clusters, form in between the nanowires for higher As/In ratios. This, together with the fact that the HRXRD measurement of the sample with almost negligible amount of clusters (lowest As/In ratio) exhibits no ZB-related reflection, suggests that only the WZ h(002) peak stems from the nanowires and the origin of the ZB c(111) peak is related to InAs clusters on the SiO_x/Si(111) sample surface.

These findings agree well with the investigations done by TEM as presented in section 4.1.1 where almost all nanowires were found to contain disordered WZ crystal structure with only low amount of ZB stacking. Therefore, InAs clusters on the sample surface require special attention with respect to data interpretation.

4.2 Photoluminescence spectroscopy of InAs nanowires

4.2.1 Experimental details

For basic optical investigation by photoluminescence (PL) spectroscopy, InAs nanowires grown on SiO_x-masked Si(111) wafers were used as presented in section 2.2. The nanowires were grown at fixed temperature of 480 ℃ applying V/III ratios between 12.6 and 56.5 to tailor the nanowires to similar lengths ($\sim$750–1000 nm) and density (20–30 μm^{-2}), while the average nanowire diameter varied, allowing diameter dependent studies of the dominant recombination mechanisms. In particular, three different nanowire samples were investigated with diameters of 135 ($\pm$ 12) nm, 60 ($\pm$ 5) nm, and 40 ($\pm$ 6) nm. The used growth conditions are very similar to the nanowires investigated in section 3.2 where residual cluster formation on the SiO_x was very low (compare Fig. 3.3), guaranteeing PL signatures which arise predominantly from the InAs nanowires. As shown in section 4.1 all nanowires exhibit a predominant WZ crystal structure with heavy stacking disorder along the nanowires (random fluctuations every few MLs). Furthermore, the morphology of all nanowires was non-tapered with nearly identical nanowire diameter across the entire lengths, which is quite important since homogeneous diameters within a given sample allow for clear, unobscured diameter-dependent ensemble PL investigations.

For PL measurements of these samples a Biorad *FTS-40* fourier transform infrared (FTIR) spectrometer was used, where a 1.55 µm continuous InP-based wave diode laser source was utilized for excitation. The samples with as-grown, free-standing nanowires on Si(111) were placed in a cryostat with liquid helium cooling and kept under vacuum conditions, where a temperature controller further enabled temperature-dependent measurements. Even though the spectrometer was purged with dry nitrogen, water absorption

lines could not be completely avoided. The emitted PL signal was measured with a liquid N_2 cooled InSb photodiode detector. The excitation laser spot was focused onto the sample with a spot diameter of approximately 50 µm, corresponding to the excitation of an ensemble volume of $\sim$4–6$\times 10^4$ nanowires. For excitation power dependent measurements the laser power was gradually increased in small increments (few mW-range) in order to avoid excess heating and damage of the nanowires. All measurements were further compared to commercially available $\sim$500-µm-thick bulk InAs(111) reference (NewWay Semiconductor Co., Ltd.) with a bulk n-type carrier concentration specified as $\sim$1–3$\times 10^{16}$ cm^{-3}.

4.2.2 Temperature dependent PL measurements

Representative temperature (T)-dependent PL spectra are shown in Fig. 4.6a (semi-log scale) for the InAs nanowire sample with the largest nanowire diameter (135 nm), as measured under excitation power of 284 mW. Similar measurements were also conducted on the bulk InAs reference, with spectra shown in 4.6b. Several interesting features are observed: First, despite the fact that the nanowires are uncapped and exhibit a large number of stacking defects they give relatively strong emission with PL signal measured up to T >130 K. The PL peak intensities show very dynamic variation (factor of $\sim$50) over the investigated temperature range (T = 15–130 K). This is quite remarkable, considering that in high surface-to-volume ratio nanowires the effect of surface and associated intrinsic electron accumulation (due to Fermi level pinning, in particular for InAs surfaces [Nog91, Ols96]) is expected to rather limit PL efficiencies. Other nanowire samples showed qualitatively similar behavior – however, for the thinnest nanowires the overall PL intensity was significantly reduced at increased temperatures, limiting identification of well resolved PL spectra above $\sim$60 K.

Secondly, the PL peak position of the nanowires shows a pronounced red-shift with increasing temperature from 0.411 eV (at 15 K) to 0.403 eV (at 130 K) with corresponding linewidths (full width at half maximum – FWHM) increasing from 29 meV (15 K) to 44 meV (130 K), respectively. Likewise, the characteristic red-shift and linewidth broadening were also observed for the bulk InAs reference, however, FWHM values of the PL peak are approximately two times smaller as compared to the nanowires (i.e., 17 meV at 12 K and 24 meV at 114 K).

According to the distinct red-shift and large temperature effect on intensity, the PL peak position is attributed to the near-band-edge transition (I^{NBE})[Sun10]. This peak position as measured at low temperature agrees also with the known InAs band gap energy (E_g $\sim$0.41 eV (15 K)[Fan90], as measured and verified on the bulk ZB InAs(111) reference

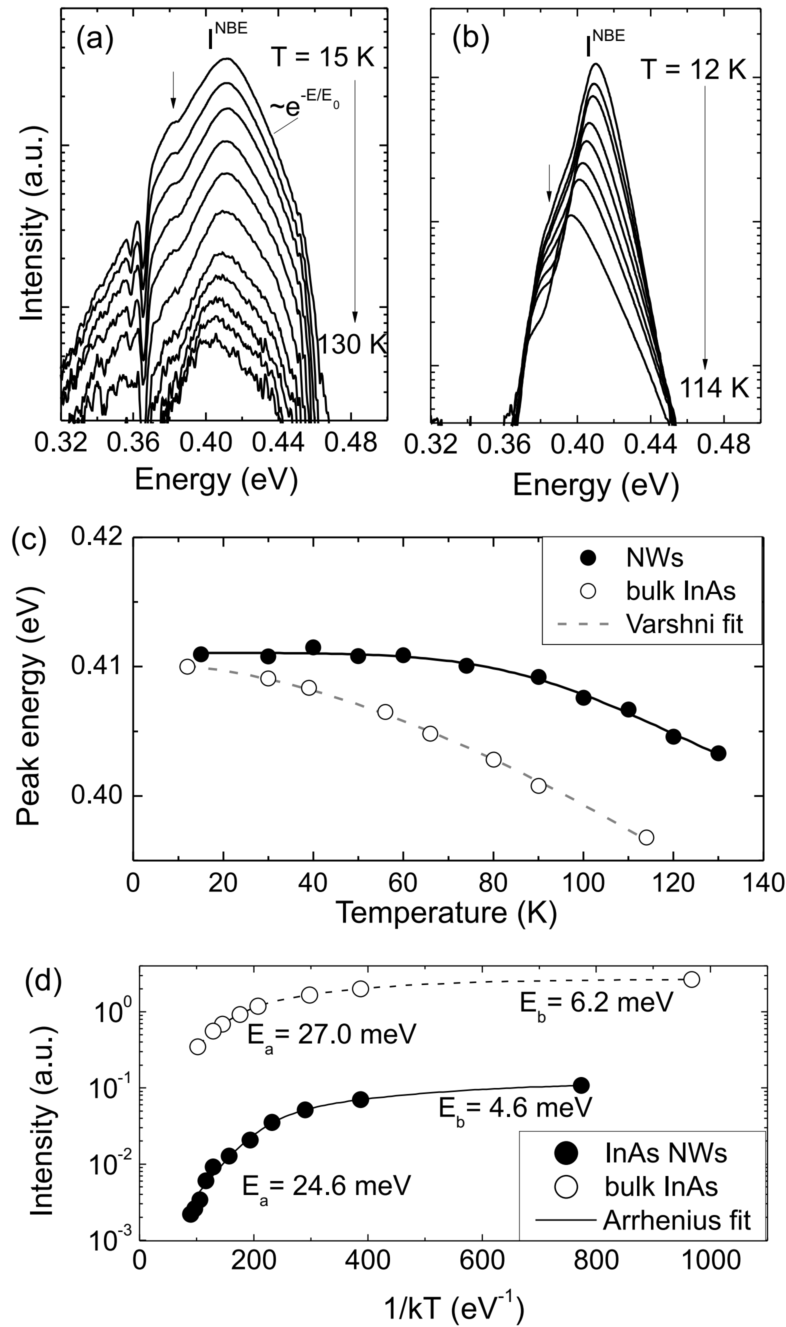

Figure 4.6. Temperature (T)-dependent PL spectra as measured for (a) the sample with nanowire diameter of 135 nm and (b) bulk InAs reference (at 284 mW power). The spectra arranged from top to bottom correspond to increasing temperature from 15 K (12 K for bulk) to 130K (114 K for bulk) with increments of ΔT between 10–15 K. (c) Corresponding T-dependent shift in peak energy emission (red-shift) for these nanowires, as compared to the respective shift obtained for bulk InAs reference (best fitted by Varshni expression). (d) Integrated PL intensity as a function of 1/T (Arrhenius plot) for both the nanowires and bulk reference, demonstrating the quenching characteristics with best fits using two activation energies (E_a, E_b) for the high- and low-T region, respectively. Published in Ref. [Kob12].

(see Fig. 4.6b). Note an extra peak or shoulder (on the low-energy tail side) near ~0.38 eV for both nanowires and bulk (marked by an arrow). This feature does not shift its position with temperature nor excitation power (see also Fig. 4.7) and was further observed in all investigated samples. This indicates that this signature could be associated with either a deep impurity or defect-related acceptor, as reported earlier also for bulk InAs [Fan90, Gro89, Gla06]. With increasing temperature the PL peak energy (I^{NBE}) thus merges with this signature, which might be caused by the effect of thermal ionization of electrons and holes in donor and acceptor states, respectively, resulting in one broader emission peak. In addition, it cannot be ruled out that structural defects (such as stacking faults or point defects) or even atmospheric absorption may contribute to such features on the low-energy side.

The PL spectra also evidence a high energy tail with a distinct exponential dependence on energy via I(E) $\propto$ exp(-E/E$_0$), where E_0 is a specific energy and E the photon energy. The high energy tail further shows a sharp cut-off near E ~0.45 eV (Fig. 4.6a), which is likely related to the well-known atmospheric H_2O absorption band between ~0.45–0.48 eV. Note that the slope of the high energy tail decreases with rising temperature, which reflects the thermal (i.e. Boltzmann) distribution of photoexcited charge carriers in the empty conduction and valence bands, i.e., revealing that PL is related to hot carrier recombination on the high energy side. Thus, the specific energy E_0 should obey a kT-dependence and reflect the kinetic energy of the thermalized charge carriers at least for high enough temperatures, while in the low temperature regime E_0 is a measure for the quality of the material [Sto06, Yan08]. The high energy tail was fitted based on the function given above and obtained values for E_0, which increase with temperature from ~17 meV (at 15 K) to ~37 meV (at 130 K) for the nanowires. For the bulk reference the respective values for E_0 ranged from 6.5 meV (at 12K) to 15 meV (at 114K), respectively, indicating a slightly better material quality.

The evolution of the PL peak energy as a function of temperature is further shown in Fig. 4.6c and compared to the corresponding peak position dependence of the bulk InAs reference. It is found that while the T-dependence of the near band-edge emission of bulk InAs could be well described by the classical Varshni formalism E_g = 0.411 - [3.82$\times$10$^{-4}T^2/(T+249)$] (in eV, T in K, and Debye temperature Θ_B = 249 K [Ger63]), the corresponding red-shift in the nanowires was slightly weaker – e.g. resulting in a PL peak energy at 120 K of ~0.395 eV in bulk, and ~0.404 eV in the nanowires, although both peak positions are equivalent at 15 K (~0.411 eV). One explanation for this slight difference is that in degenerate narrow bandgap semiconductors such as InAs the positions of the band-edge are sensitive to carrier density especially at increased temperatures [Fil87, Li93].

Indeed, from electrical back-gate voltage dependent measurements of single InAs nanowire field-effect transistors the room temperature n-type carrier density was estimated in thick InAs nanowires (diameter > 130 nm) to about 10^{17} cm^{-3} [For11, Ges12]. The more than one order of magnitude higher intrinsic carrier concentration in the nanowires as compared to undoped bulk InAs may thus explain the observed effect. Nevertheless, one cannot rule out a certain possibility of local temperature changes in the nanowires as opposed to bulk due to the underlying laser excitation.

Fig. 4.6d shows the integrated PL intensities as a function of 1/kT (Arrhenius plot) for the InAs nanowires and bulk reference in the measured T-range (12–130 K). Across this range the data could be best described by the relation $I(t) = I(0)/(1 + Ae^{\frac{-E_a}{kT}} + Be^{\frac{-E_b}{kT}})$ where E_a and E_b are the thermal activation energies for high- and low-T regions, respectively, I(0) is the intensity at low temperature, and the coefficients A and B measure the strengths of both quenching processes. Best fitting of data from the nanowires give thermal activation energies of $E_a = 24.6 \pm 3.4$ meV for the high-T region and $E_b = 4.6 \pm 2.2$ meV for the low-T region. Very similar values were also obtained for the bulk reference, i.e., $E_a = 27.0 \pm 3.0$ meV (at high-T) and $E_b = 6.2 \pm 0.6$ meV (at low-T), respectively. The similar thermal activation energies in the high-T region suggest that luminescence efficiencies are not too much different between the nanowires and bulk. On the other hand, PL at low-T is associated with transitions from low-density localized states, and the relatively low, finite activation energies suggest that low-density localized states from band tails are present.

4.2.3 Power dependent PL measurements

More details in recombination characteristics are gained from excitation power-dependent PL measurements at low-T (15 K), as displayed in Fig. 4.7 for all three nanowire samples with diameters of (a) 135 nm, (b) 60 nm, and (c) 40 nm, respectively. The spectra show an expected increase in PL intensity along with a slight shift to higher peak energies (blue-shift) by increasing excitation power (from 27 mW to 284 mW). The blue-shift appears largest for the thickest nanowires ($\sim$5.5 meV for 135-nm-wide nanowires), followed by the thinner nanowires, i.e., ($\sim$3.5 meV for 60-nm-wide nanowires and $\sim$2 meV for 40-nm-wide nanowires). The respective blue-shift for the bulk reference was $\sim$6 meV over the same excitation power range. Increasing excitation power further shows a slight linewidth broadening with FWHM values increasing from $\sim$40 meV (at 27 mW) to $\sim$47 meV (at 284 mW), which is consistent for all three nanowire samples.

The small blue-shift and linewidth broadening over the approximately one order of magnitude variation in excitation power point to a band-filling effect of photocarriers to the

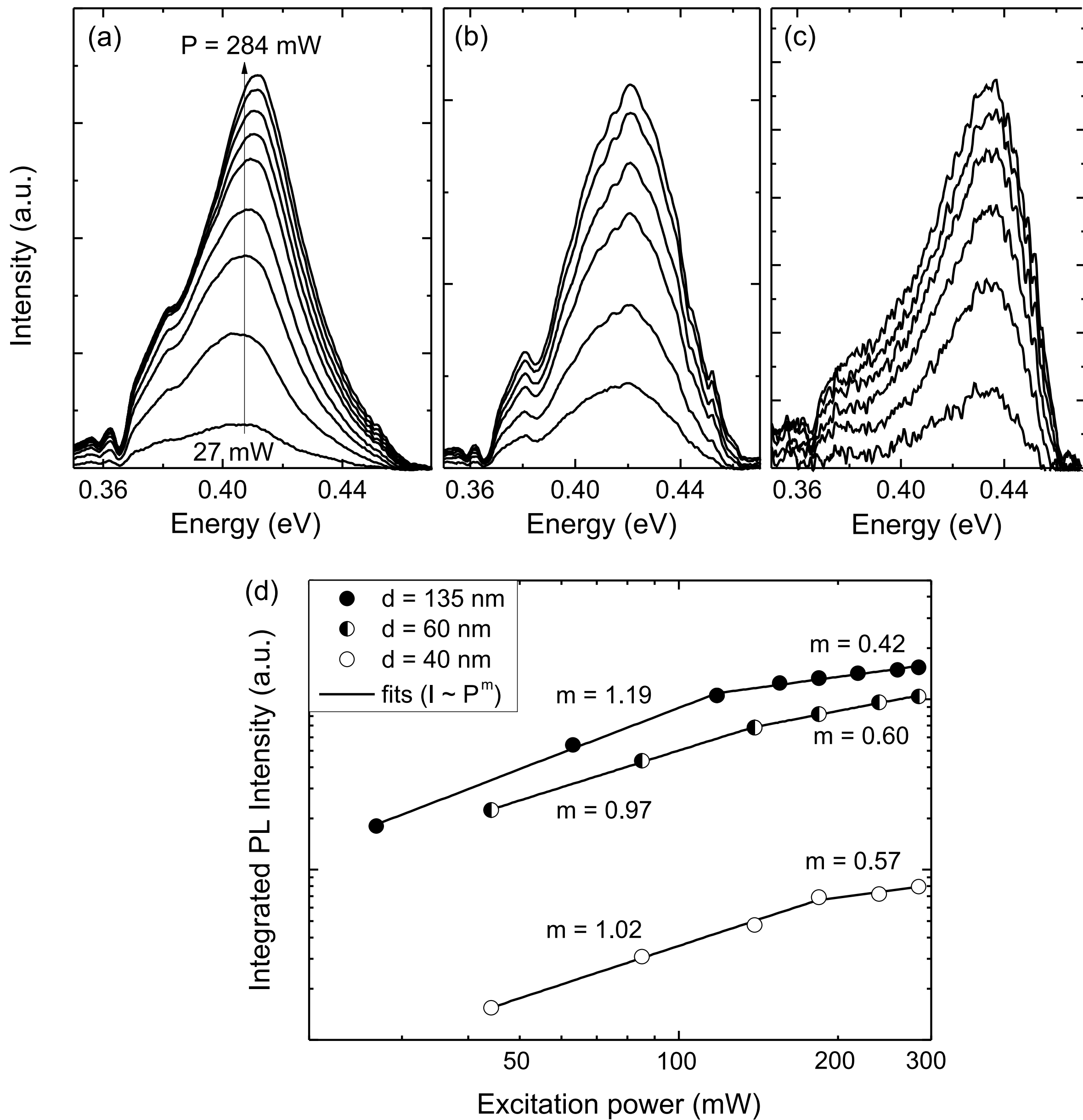

Figure 4.7. Excitation power dependent PL spectra recorded at 15 K for three samples with nanowire diameters of (a) 135 nm, (b) 60 nm, and (c) 40 nm. Spectra (from bottom to top) correspond to increasing power from 27 mW to 284 mW in increments of ΔP ~25–50 mW. (d) Integrated PL intensity versus excitation power (log scale) evidencing a transition from linear scaling (I(P) $\propto$ P^m with m ~0.97–1.19) to saturation (m ~0.42–0.6). Published in Ref. [Kob12].

valence band. However, this effect appears not very strong which could be due to two reasons: (i) the finite PL linewidth of ∼40–47 meV observed in the nanowires may partially obscure the local band filling effects, and (ii) non-linearities in power-dependent PL intensity may lead to saturation at high excitation power. Fig. 4.7d shows the integrated PL intensity as a function of excitation power (log scale), as obtained for the three nanowire samples. The integrated PL intensity scales almost linearly with power for low excitation power (<100 mW), yielding a dependence $I(\mathrm{P}) \propto \mathrm{P}^m$ with a power factor m ∼0.97–1.19 for the three investigated samples. Strong deviation and saturation of the integrated PL intensity occurs at higher excitation power (>100 mW) with power factors reduced to m ∼0.42–0.6.

4.2.4 Effect of nanowire diameter

Since InAs is a degenerate n-type semiconductor with high equilibrium free electron densities >10^{16}–10^{17} cm^{-3}, the linear dependence of integrated PL intensity versus excitation power in the low excitation power regime corresponds to low photocarrier concentrations with respect to background doping. Hence, the low excitation power response represents more accurately the direct band-to-band transition, such that low-T, low-power (15 K, 85 mW) PL spectra are further compared in Fig. 4.8a for all InAs nanowire samples with respect to the bulk reference (in gray). This plot highlights very interesting features: Besides the already discussed broader PL linewidths of the nanowires, the nanowire samples evidence decreased PL intensity, which scales with nanowire diameter (i.e., thinner nanowires give less PL intensity) as expected from increasing non-radiative surface recombination. This observation is, however, strongly governed by the obviously much lower excitation volume in the nanowire samples. To account for excitation volume differences, a fill-factor correction was applied using the known nanowire densities of each sample, which increased the apparent PL intensities by a factor of >10 with respect to uncorrected values. This demonstrates that at least for the thicker nanowires the PL efficiency is not more than ∼5–10 times lower as compared to bulk InAs, confirming our earlier interpretations of strong PL efficiency even from uncapped InAs nanowires.

Fig. 4.8a also shows a gradual blue-shift to higher PL peak energies with decreasing nanowire diameter, with PL peak energies measured at 0.408 eV for 135-nm-wide nanowires, 0.419 eV for 60-nm-wide nanowires, and 0.436 eV for 40-nm-wide nanowires, respectively. To account for this blue-shift we considered quantum confinement effects based on the diameter difference of the nanowires and calculated the respective band-edge energy shift between the ground states of the conduction band (CB) and the valence band (VB). Note that the confinement energy is mainly determined by the ground state energy

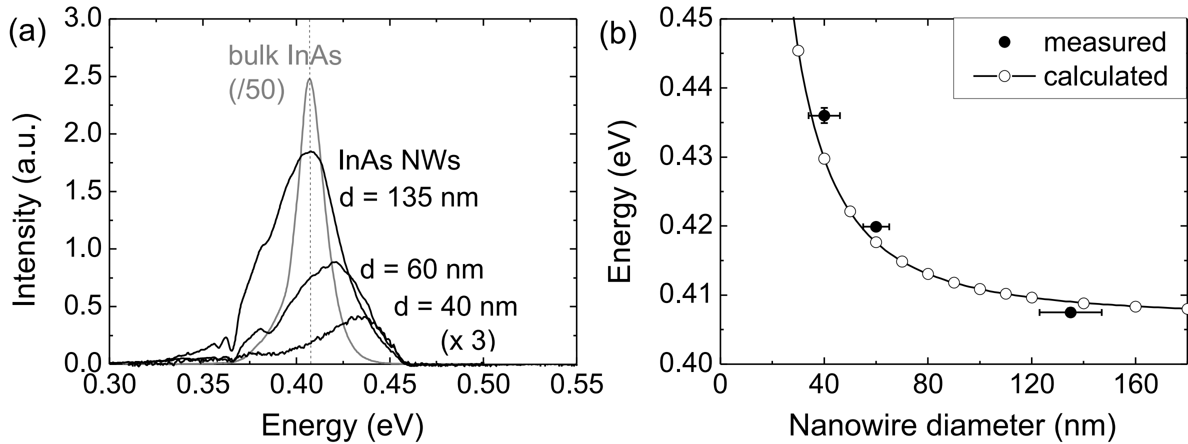

Figure 4.8. (a) Direct comparison of low-T PL spectra (taken at 15 K, 85 mW) of the three corresponding nanowire samples, showing decreased intensities and a pronounced blue-shift with decreasing nanowire diameter with respect to bulk InAs reference (in gray). (b) Plot of the band-edge energy shift as a function of nanowire diameter showing simulated data based on radial quantum confinement effects of the ground state energy (open symbols) in comparison with as-measured data from PL peak positions (closed symbols). Published in Ref. [Kob12].

of electrons in the CB, due to the large difference in electron and hole effective masses in InAs. For the calculation a hexagonal cross-section is assumed with infinite barriers and the nanowire diameter-dependent confinement energy is modeled at 15 K using the *nextnano* device simulator [nextnano]. The simulated result is shown in Fig. 4.8b, where the energy between the CB and VB ground states at infinite nanowire diameter is normalized to the band-edge PL peak position of bulk InAs (i.e., 0.407 eV at 15 K and 85 mW). The simulated data (open symbols) shows a characteristic $1/d^2$ relation between band-edge energy and nanowire diameter (d denoted as nanowire diameter), i.e., giving a shift in band-edge energy from 0.408 eV (d = 200 nm) to 0.443 eV (d = 30 nm). The curve illustrates that the onset of quantum confinement for InAs nanowires occurs already at fairly large nanowire diameter (>60 nm), as a result of the very small electron effective mass of InAs. The measured band-edge PL peak energies (closed symbols) are also plotted and show reasonable agreement with the simulated results. These results suggest that the observed diameter-dependent blue-shift in PL peak energies can be attributed to radial quantum confinement effects.

These results further suggest that the band-edge energies of the InAs nanowires are not much different from bulk ZB InAs, despite the substantially different crystal structure of the nanowires (WZ dominant crystal phase). This indicates that the band gap energy of WZ InAs is close to that of ZB InAs, as also suggested in a recent report by Sun et al. [Sun10].

Since measurements are not performed at absolute zero temperature, one should keep in mind that for narrow-gap semiconductors an energy value on the order of $k_\mathrm{B}T$ may limit the absolute determination of band gap energy. Moreover, it is interesting that the relatively high density of stacking faults do not appear to cause a substantial shift of the dominant band-edge emission position. This observation is supported by the very similar PL peak position of defected WZ-type nanowires measured here and phase-pure WZ nanowires as measured by Sun et al. for comparable nanowire diameters [Sun10]. Structural defects such as random short-period WZ/ZB phase transitions often cause substantial shifts in emission energy for certain nanowire systems. This is shown for instance for mixed WZ/ZB GaAs [Spi09] and InP [Bao08] nanowires, where conduction and valence band (CB and VB) discontinuities and type-II band alignment at such WZ/ZB phase boundaries lead to interface electron-hole pair confinement and spatially indirect recombination at energies significantly lower than the phase-pure bulk case. For the defected WZ-type InAs nanowires presented here these effects appear not as pronounced as in other nanowire systems, possibly due to two reasons: First, no extended ZB segments (with lengths >1–2 ML) were observed in these nanowires (see TEM micrographs in section 4.1.1), such that type-II like quantum wells (QW) along the nanowire are too thin to substantially confine indirect electron-hole pairs. Secondly, the theoretically predicted CB/VB offsets between WZ and ZB phase in InAs are lower than in other systems (GaAs, InP)[Mur94], which would require wider QW segments for more effective confinement. However, as suggested before it cannot be ruled out that the anticipated indirect transitions might be present within the low-energy tail, superimposed by the overall signal and hence invisible over the recorded broad spectra. Further experiments on low-density nanowire ensembles or single InAs nanowires with large ZB segment lengths might be necessary to provide more insights.

4.3 Conclusion

In conclusion, nanowires from two distinct sample series, namely an As flux series and a growth temperature series were investigated by TEM and HRXRD. TEM analysis revealed heavily disordered WZ structure with WZ/ZB stacking faults occurring every few monolayers for InAs nanowires grown with As/In ratios of 24–81. No significant dependence of the crystal structure on the As/In ratio was observed. However, the nanowire growth temperature was found to influence the crystal structure such that longer phase pure WZ segments up to lengths of 10 nm are observed for elevated growth temperatures of 530 ℃. The nanowire samples grown with different As fluxes were further analyzed by HRXRD where a significant InAs WZ h(002) reflection peak at 2θ = 25.37° was found for all investigated samples. An

additional peak at 2θ = 25.45° could be attributed to InAs ZB c(111) stemming directly from cluster formation under high As/In ratios.

In addition, low-temperature photoluminescence spectroscopy was performed on InAs nanowire ensembles with disordered WZ structure. The nanowires were tailored to similar length but substantially different nanowire diameter (40–135 nm) facilitating investigation of the nanowire diameter-dependent band-edge emission. The unpassivated nanowires showed relatively strong emission efficiency with emission up to >130 K, characteristic red-shift with temperature and low-temperature band-edge energy position of $\sim$0.41 eV identical to bulk ZB InAs, particularly for thick nanowires. Reduction in nanowire diameter gave a characteristic blue-shift ($\sim$0.435 eV for 40-nm-thin nanowires) which is related to quantum confinement effects as supported by *nextnano* simulations.

5 Positioned InAs nanowire growth

In this chapter position-controlled growth of InAs nanowires on lithographically patterned SiO_2/Si(111) will be presented. First, the sample processing via e-beam lithography and nanoimprint lithography and its influence on the nanowire growth quality is discussed. Furthermore, the nanowire growth kinetics are investigated in detail, showing the main dependencies of nanowire morphology on growth temperature, nanowire distance (pitch), growth time and As fluxes. The results presented in this chapter are published in Ref. [Her10].

5.1 Substrate preparation for position-controlled nanowire growth

5.1.1 Small size patterned substrates by electron beam lithography

To grow ordered nanowire arrays on Si(111) with full control over the nanowire position, the granular rf sputtered SiO_x mask layer is substituted by 20-nm-thick thermally grown SiO_2. In Fig 5.1 AFM images depict the surface of sputtered oxide (a) and thermally grown oxide (b) on a Si(111) substrate as supplied by the wafer provider *Si-Mat*. The equal height scale of both images (10 nm) allows a direct comparison of the surface roughness. The sputtered oxide exhibits a granular structure promoting the opening of pinholes when etched in HF as discussed in section 2.1, whereas the thermal SiO_2 surface is very smooth with a root mean square (RMS) roughness < 0.2 nm (Fig. 5.1b). This increases significantly HF etching homogeneity and suppresses arbitrary pinhole formation. For example, thermally grown SiO_2 masks demanded HF etching to less than 2 nm before pinhole opening is sufficient for self-assembled nanowire growth [Rud11]. The difficulty to form random pinholes above this thickness enables, however, excellent structural patterning via electron beam (e-beam) lithography and reactive ion etching.

The sample preparation process is illustrated in Fig. 5.2 in six steps for the as-received 20 nm SiO_2/Si(111) wafer (schematic 1) to the patterned substrate after nanowire growth (schematic 6). First of all, 100-nm-thick Polymethyl methacrylate (PMMA) positive e-beam resist is spin coated on the oxide surface and subsequently baked at 180 °C for six minutes (schematic 2). The wafer is then processed by e-beam lithography (Raith *E-line*) where the

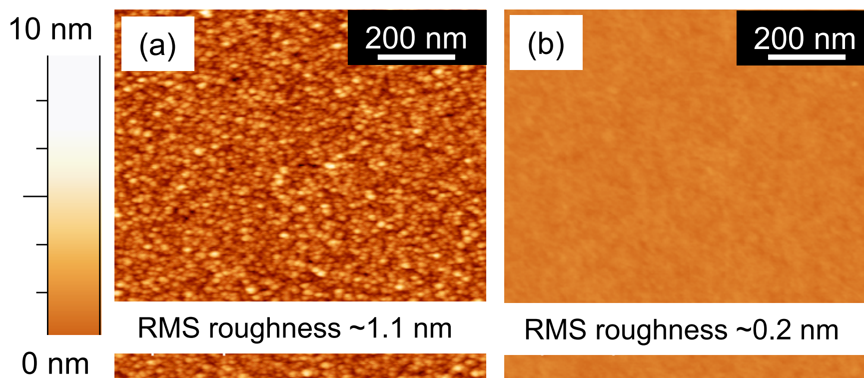

Figure 5.1. AFM images of (a) a 20-nm-thick rf-sputtered SiO_x layer on Si(111) in comparison to (b) a 20-nm-thick thermally grown SiO_2 layer on Si(111). The RMS roughness over a 1×1 μm^2 area is $\sim$1.1 nm and $\sim$0.2 nm, respectively.

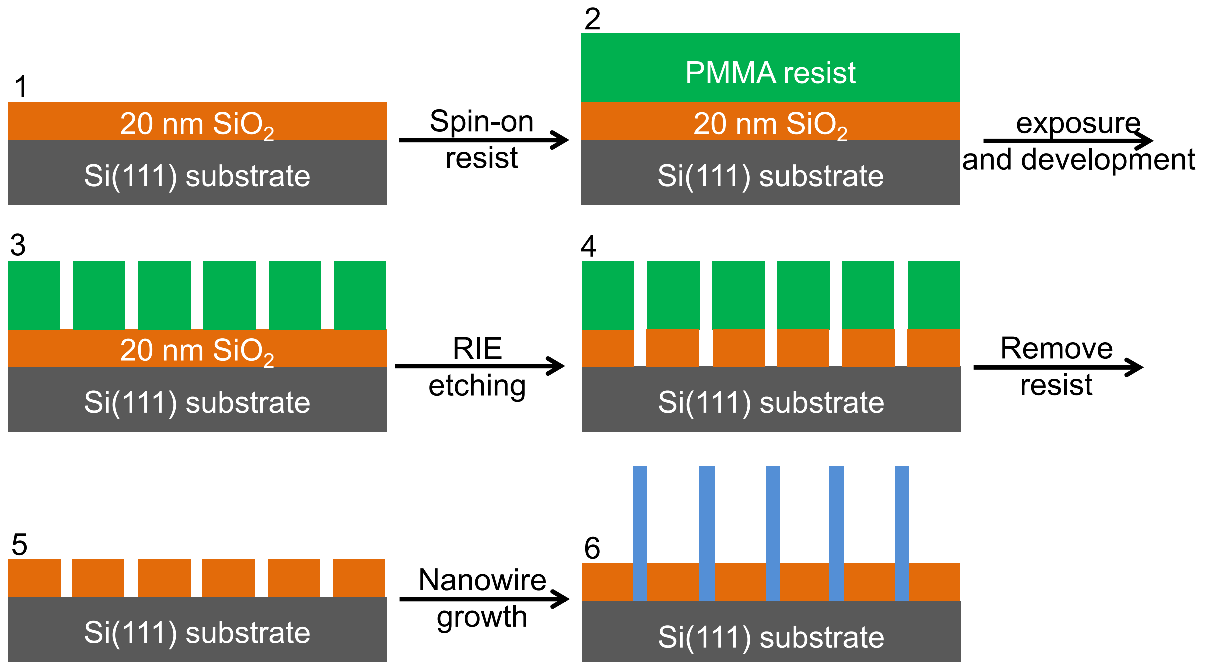

Figure 5.2. Six-step illustration of the wafer preparation sequence prior to position-controlled nanowire growth. The commercially available SiO_2/Si(111) substrates are covered with a 100-nm-thin PMMA resist for e-beam exposure. After exposing the desired pattern and developing the PMMA resist the structure is transferred to the SiO_2 layer by plasma etching (RIE). A final HF dip after acetone resist-removal provides a clean Si(111) surface in the defined holes free of oxide. The wafer is ready for growth and can be loaded into the MBE system.

PMMA is exposed by an electron beam leading to chain secession of the polymer. After e-beam exposure a Methyl isobutyl ketone (MIBK) developer bath removes the cracked polymers and hence transfers the exposed pattern into the PMMA (schematic 3). The hole pattern is subsequently transferred into the underlying SiO_2 layer by reactive ion etching (RIE) using C_4F_8/SF_6 plasma (schematic 4). Finally, the resist was removed in an acetone ultrasound bath (schematic 5) to provide a clean substrate surface. Prior to MBE loading the wafer is submerged in HF removing residual SiO_2 in the defined holes exposing the underlying silicon. Before nanowire growth is performed the substrate undergoes the same pre-annealing steps as reported in section 2.1, i.e., a twofold annealing to 300 and 730 ℃, respectively. It has to be mentioned that a large variety of patterns with squares, lines and circles can be predefined via a software and therefore quickly be patterned into the PMMA. Typically, circles are used with diameters of 30–150 nm and hole to hole distances (pitches) of 150 nm to 10 µm allowing systematic studies of position-controlled nanowire growth under various conditions.

Some of the processing steps need a more careful investigation since they are highly

critical for successful nanowire growth. First of all, the PMMA development is studied in more detail. AFM measurements of one of the holes in the PMMA after exposure and development were performed for different development times. In Fig. 5.3a AFM line scans through such a hole with a nominal diameter of 80 nm (as defined by e-beam exposure) is depicted for development times from 30 s to 60 s. It turned out that a development duration of 30 s (black curve) was too short, i.e., the PMMA was not removed. Using 40 s (red curve) the wafer was submerged in the developer bath for extra 10 s, leading to complete erosion of the hole with a flat bottom and a depth that equals the PMMA thickness of 80–90 nm. For durability studies the wafer was then kept in air for 14 hours and was remeasured by AFM (blue curve) without further treatment. Interestingly, an identical hole shape could be verified indicating excellent stability of the PMMA. This is an important information because converging of the PMMA would demand immediate reactive ion etching to ensure a constant reproducibility. Further development of 50 s and 60 s did not lead to any change in the hole structure (see green and brown curve). To remove any remnant resist particles still adsorbed in the hole, a short oxygen plasma etching step was applied after developing the pattern. Fig. 5.3b shows an AFM measured line scan of a single hole (developed for 60 s) for different O_2 plasma durations revealing two effects, namely (i) a widening of the hole and less tapered geometries with steeper walls which (ii) are achieved already for the shortest applied plasma duration of 10 s. Most likely cracked polymer which was not removed by the developer is etched faster than uncracked PMMA yielding a more cylindrical shape of the pinhole. In contrast, O_2 treatment of more than 30 s enlarges the hole diameter to unwanted dimensions > 100 nm. As a consequence, a 10 s O_2 plasma treatment was routinely performed after development for all samples.

The next step is to transfer this pattern of holes into the SiO_2 layer. This was done by reactive ion etching (RIE) in an Oxford *Plasmalab 80 Plus* using C_4F_8/SF_6 plasma at a pressure in the low 10^{-5} mbar-range at room temperature. The etching rates were calibrated using two kind of wafers, i.e., 22 nm SiO_2/Si(111) wafers and bare Si wafers. Hence, both etching rates of Si oxide and Si could be calibrated by AFM depth profiling of holes etched for various durations. The result is plotted in Fig. 5.4 for SiO_2 (black circles) and the bare Si(111) (open circles) yielding etching rates of 0.61 nm/s and 5 nm/s, respectively. The values for Si (open holes) were shifted by 36 s along the x-axis for illustration purposes. Note that a 2 s ignition delay needs to be added to the calculated etching duration.

The patterns are etched such that 3 nm of SiO_2 remains within the holes to hinder unwanted damage of the underlying Si since this would significantly decrease the nanowire growth yield (see section 5.2.1). The PMMA resist can be removed after RIE etching using an acetone ultrasound bath followed by an Isopropanol (IP) cleaning dip. At this point the

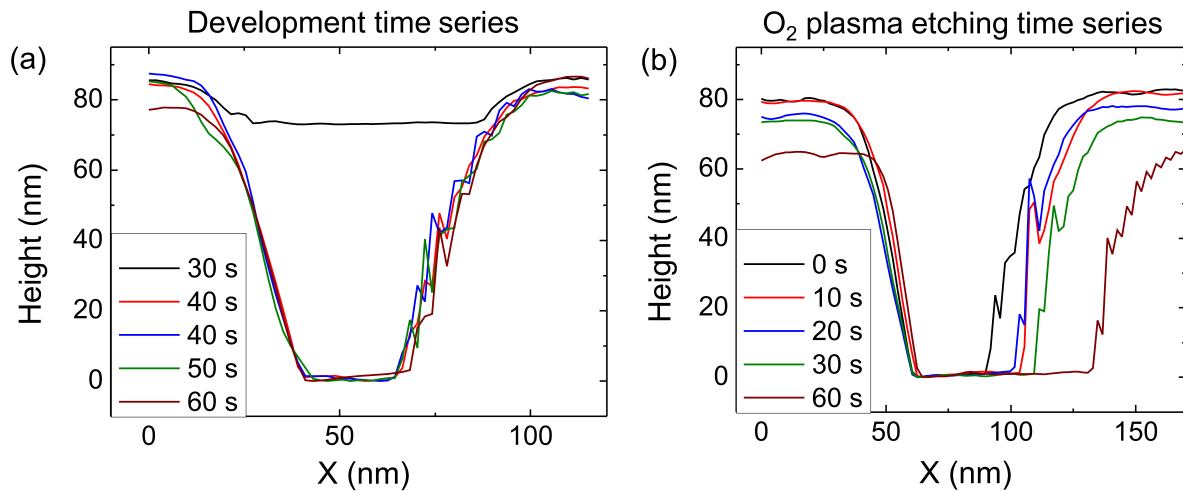

Figure 5.3. AFM line scans across one of the holes developed in the PMMA resist are depicted in dependence of the development duration (a) and the duration of an optional O_2 plasma etching step for a fixed development time of 60 s (b). For durability investigations the 40 s development in (a) was measured twice, i.e., immediately after processing (red line) and 14 hours later (blue line).

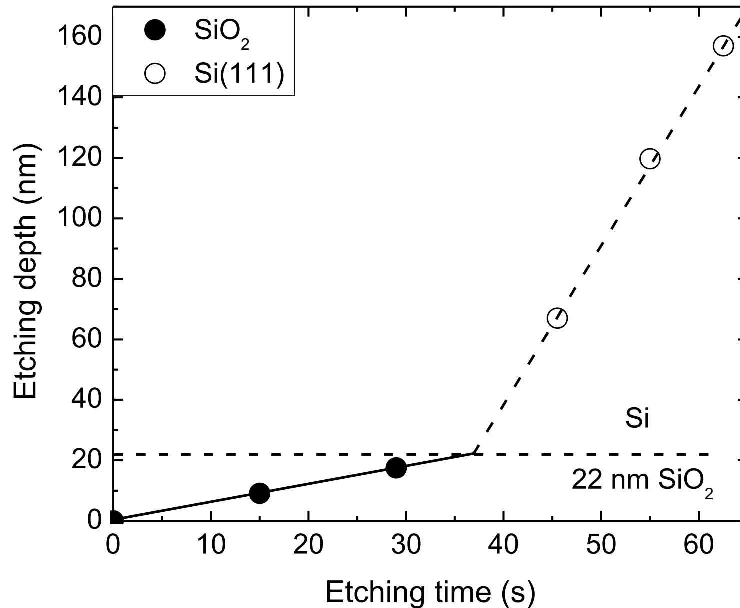

Figure 5.4. RIE etch rate calibration for SiO_2 (black circles) and Si(111) (open circles) applying C_4F_8/SF_6 plasma in an Oxford *Plasmalab 80 Plus*. All values for Si were shifted 36 s along the x-axis for illustration purposes. The plasma etching rate was found to be 0.61 nm/s for SiO_x and 5 nm/s for Si(111).

(a) (b)

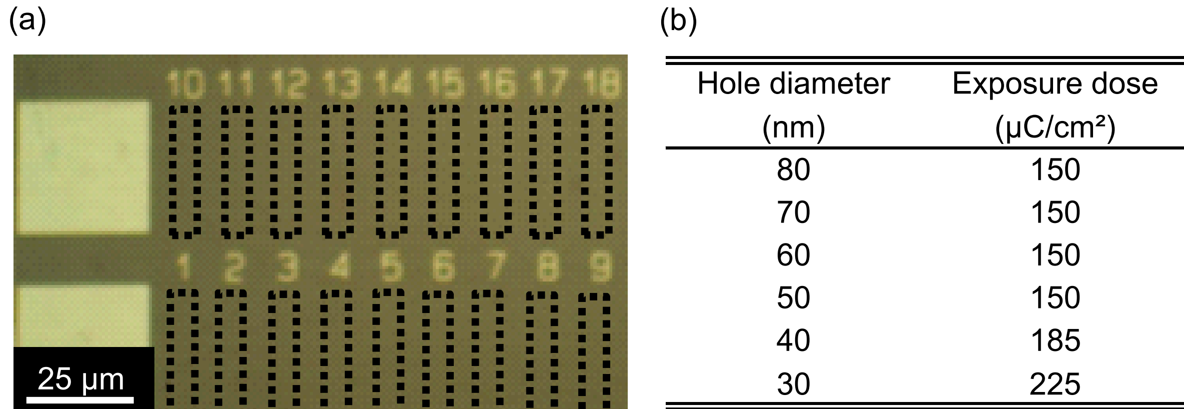

Hole diameter (nm)	Exposure dose (µC/cm²)
80	150
70	150
60	150
50	150
40	185
30	225

Figure 5.5. (a) The photograph shows a part of the developed test-pattern for identification of the optimal e-beam lithography exposure dose. The square markers facilitate fast localization of the structure via optical microscopy. Each line exhibits nine fields of pinholes (marked by dotted boxes) with increasing exposure dose but fixed nominal hole diameters D_{nominal} between 10 nm and 80 nm. After transferring the pattern into the underlying SiO_2 by plasma etching, AFM is used to measure the actual hole diameter D in dependence of the exposure dose. The optimum doses for specific hole diameters where $D = D_{\text{nominal}}$ are given in (b).

holes (now in the SiO_2) are again measured by AFM to check the actual diameter D which highly depends on the chosen exposure dose and can differ from the setpoint D_{nominal} given to the e-beam software. This means the exposure dose needs to be calibrated in order to achieve good control over structure dimensions. The dose calibration was performed as illustrated in Fig. 5.5a. Eight lines, each containing nine fields of holes (marked by dotted boxes), were exposed onto a test substrate. All holes in one line have a fixed nominal diameter D_{nominal} (setpoint in the software) between 10 and 80 nm in 10 nm steps. Each field in a line was exposed with a different dose between 50 and 300 µC/cm^2. The dose represents the charge (i.e., electrons) per area impinging the PMMA and is given in µC/cm^2. Large quadratic markers facilitate fast localization of the pattern even by basic optical microscopy as available in the AFM setup. The diameters D of five holes for each field were averaged and compared with the nominal diameter D_{nominal} revealing the optimum doses where $D = D_{\text{nominal}}$. For too low doses we found typically $D < D_{\text{nominal}}$ whereas for higher doses $D > D_{\text{nominal}}$ was observed. The optimum dose for holes with $D \geq 50$ nm was 150 µC/cm^2 whereas for $D < 50$ nm the dose had to be increased to values of 185 µC/cm^2 (40 nm) and 225 µC/cm^2 (30 nm). A table of optimum exposure doses for different hole diameters is given in Fig. 5.5b. Note that minimum hole diameters D of $\sim$30 nm could be achieved.

Utilizing this knowledge 2-inch wafers were then prepared for position-controlled nanowire

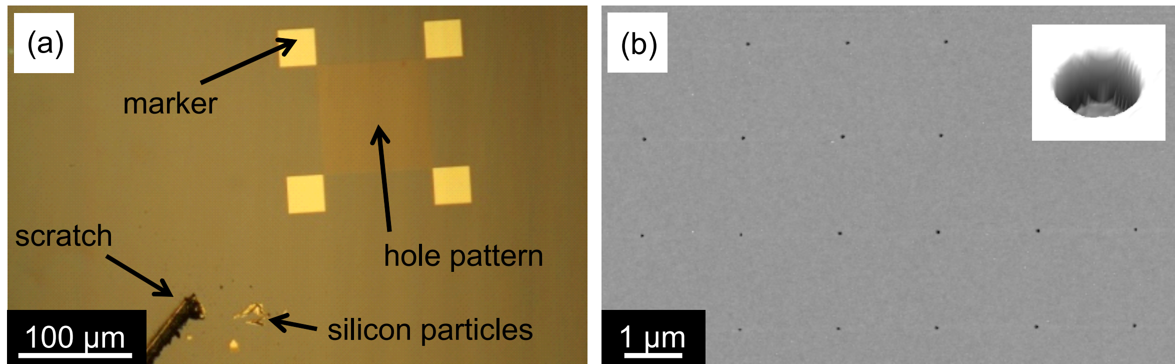

Figure 5.6. (a) Optical micrograph of a patterned field of holes (80 nm diameter and 2 µm pitch) on a 2-inch SiO_2/Si(111) wafer. A scratch on the wafer is necessary for adjustment of e-beam parameters (i.e., focus, stigmator) and helps to find the small pattern with optical microscopy. (b) AFM image of the hole pattern presented in (a). The magnified area (inset) shows a 3D AFM plot of one single hole.

growth. To begin with, a line was mechanically scribed in the SiO_2/Si(111) from the edge to the center of the wafer where the pattern will be exposed. The purpose of this scratch is twofold. First it guides the way to the pattern for coarse localization, and second, Si particles at the end of the scratch facilitate appropriate adjustment of e-beam system optics (focus, stigmator etc.). Pattern exposure in the center of the wafer further ensures reproducible temperature conditions for different growth runs. The optical micrograph presented in Fig. 5.6a shows a hole pattern etched into the SiO_2 layer of a 2-inch wafer. The pattern is surrounded by four markers for fine localization. The 100 µm $\times$ 100 µm large structure was exposed by e-beam lithography applying standard parameters as reported above, i.e., a dose of 150 µC/cm^2 for hole diameters D_{nominal} of 80 nm and a nominal pitch of 2 µm. A magnified image of the pattern taken by AFM is depicted in Fig. 5.6b revealing a perfect match to the applied values. The inset shows a magnified 3D AFM micrograph of one single pinhole with a depth of 17 nm and a perfect cylindrical shape corroborating once more the excellent processing quality. This wafer will be ready for nanowire growth after a short HF dip removing the remnant 3 nm silicon oxide in the defined holes. For extended growth kinetic studies hole arrays with various pitches and hole diameters were arranged on the same wafer.

5.1.2 Large-scale patterned substrates by nanoimprint lithography

The patterns obtained by electron beam lithography can be designed in various manners with different hole diameters and pitches. Several fields of different pitches can be fabricated

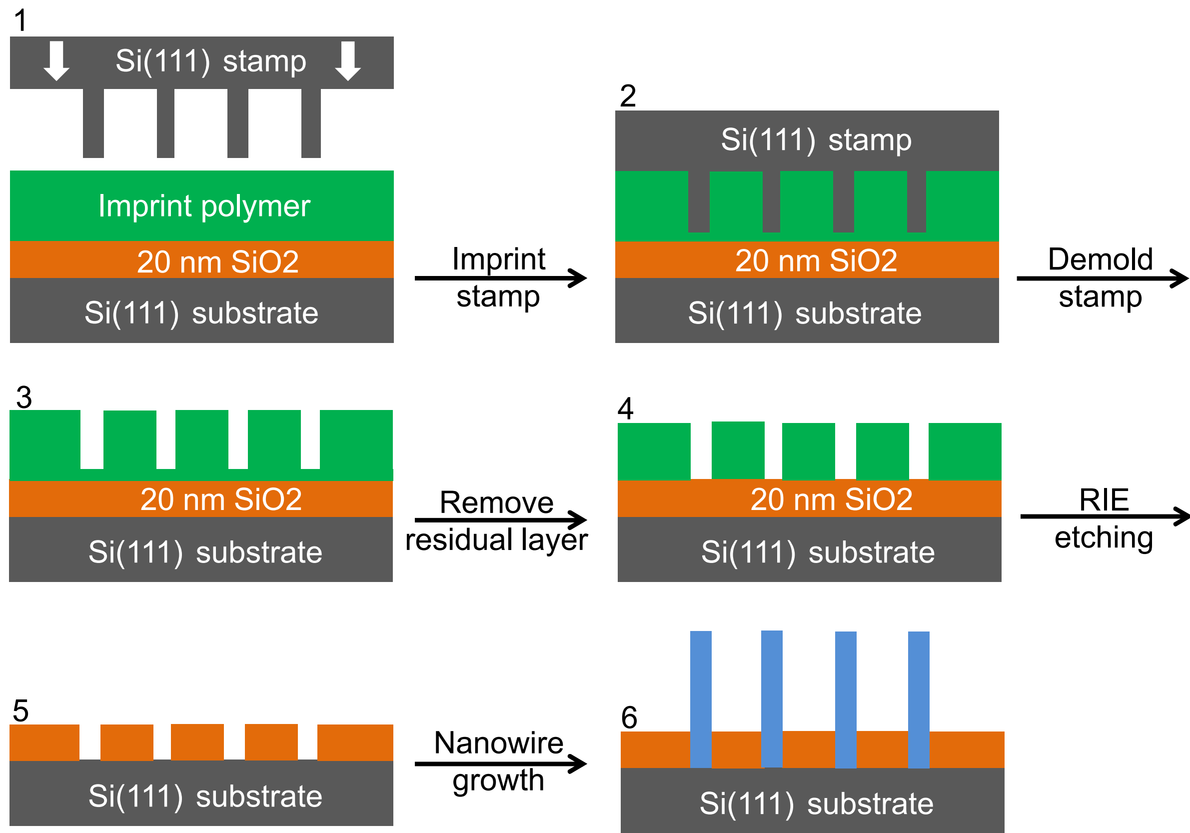

Figure 5.7. Schematic of the nanoimprint process for large-scale patterned substrates. A Si stamp with 100-nm-high pillars is pressed in a special imprint resist with the same height at elevated temperature and under high pressure. Remnant resist in the holes is subsequently removed by O_2 plasma etching. Finally, the pattern is transferred in the SiO_2 layer by reactive ion etching providing an identical pre-patterned wafer as obtained for standard e-beam lithography. NIL offers large-scale patterned structures with high throughput fabrication.

onto one wafer yielding powerful and fast growth kinetic studies with a minimum number of growth runs. However, the sequential nature of e-beam writing leads to high exposure durations limiting the pattern to an area of a few hundred μm^2. For certain post-growth characterization methods (such as X-ray diffraction, see sections 5.2.2 and 6.2) and for device application much larger nanowire fields are required. For this purpose, nanoimprint lithography (NIL) offers a method to fabricate large-scale hole patterns in a fast, parallel process without electron beam lithography by using a Si master stamp. A typical stamp contains a pattern of 100-nm-high pillars which are pressed into a thermal imprint resist (Microresist *mr-I 8010R*) spin-coated on a SiO_2/Si(111) wafer (see Fig. 5.7, schematics 1 and 2). For the 2-min-long imprint process an Obducat *Nanoimprinter* (thermal press NIL) is used at a pressure of 30 bar and elevated temperature of 165 °C. For these parameters

the resist is well above the glass transition temperature of 105 ℃ ensuring an optimum conformation to the stamp structure (schematic 2). During cool-down to 90 ℃ the resist solidifies facilitating preservation of the imprinted pattern after demolding the stamp. The remnant layer of resist is subsequently removed by O_2 plasma etching (schematic 4) before transferring the pattern into the SiO_2 layer as discussed in the previous section (schematic 5). Again, a final HF dip prior to MBE loading of the wafer guarantees oxide free holes making the wafer ready for nanowire growth (schematic 6).

In total, five 12 mm $\times$ 12 mm quadratic Si stamps were commercially acquired with 8 mm $\times$ 8 mm pillar patterns with fixed diameter of 60 nm and different pitches of 250 nm, 500 nm, 1000 nm, 2000 nm and 3000 nm. In addition, other nanoimprint stamps were self-fabricated utilizing negative e-beam resist on Si wafers and reactive ion etching to form the pillars as presented in appendix A. Support with NIL was provided by the group of Prof. Lugli (TU Munich).

5.2 Positioned growth of InAs nanowires on Si(111)

5.2.1 Growth selectivity and vertical nanowire growth yield

InAs nanowires were grown on pre-patterned SiO_2/Si(111) substrates prepared as reported in section 5.1.1. All growth runs presented in this section were performed for different temperatures from 460 ℃ to 520 ℃ at fixed growth time of 90 min and fixed In and As fluxes of 0.24 Å/s and 1.51 Å/s, respectively. As an important parameter defining the quality of growth, *growth selectivity* had to be adjusted which was found to be critically dependent on growth temperature. In general, growth selectivity is defined by whether growth takes place merely within the predefined holes or whether additional material is deposited at the surrounding SiO_2 mask. An example is shown in Fig. 5.8. Obviously, the selectivity depends critically on the growth temperature, as characterized by the area in the vicinity of a single hole in a patterned substrate with 5 µm pitch. For the given V/III ratio, growth at a temperature of 460 ℃ resulted in nanowire formation at the predefined hole but also in large InAs cluster coverage on the SiO_2 surface due to reduced surface diffusion at this temperature (Fig. 5.8a). In contrast, at 480 ℃ surface diffusion on SiO_2 was significantly increased, yielding much lower sticking probability of In on SiO_2 as compared to Si(111) and hence InAs nanowires nucleated only at the predefined holes (see Fig. 5.8b). The length of the nanowires is reduced from $\sim$1.0 µm (460 ℃) to $\sim$0.85 µm (480 ℃). For growth temperatures higher than 480 ℃, the selectivity was still perfectly realized but the nanowire lengths are reduced to shorter nanowires ($\sim$0.52 µm) for 505 ℃ (Fig. 5.8c) and merely

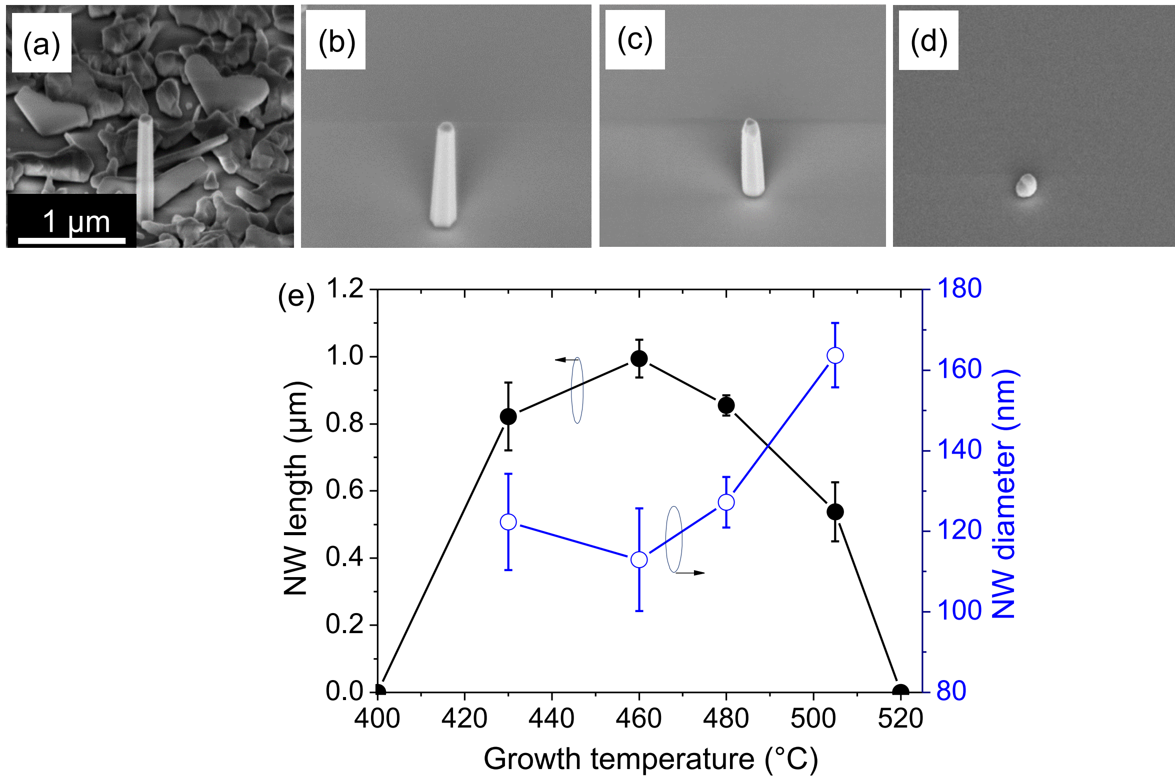

Figure 5.8. SEM micrographs showing the area in the vicinity of a pre-defined hole (lithographically patterned with a diameter of 80 nm and pitch of 5 µm) after growths performed at different substrate temperatures ranging from (a) 460 ℃ to (b) 480 ℃, (c) 505 ℃ and (d) 520 ℃. The growth conditions were otherwise constant with In rate = 0.24 Å/s, and As rate = 1.51 Å/s. (e) Plot of the nanowire length (closed circles) and diameter (open circles) as a function of temperature. Published in Ref. [Her10].

InAs droplets for 520 ℃ (Fig. 5.8d). The length and diameter of ten nanowires per sample are further plotted as a function of growth temperature in Fig. 5.8e. This characteristic length and diameter dependence on substrate temperature reflects perfectly the findings for self-assembled nanowire growth as discussed in detail in section 2.2.2. In particular, it is apparent that the highest aspect ratio is achieved for intermediate temperature and lowest aspect ratio for higher and lower temperatures, in accordance to the trend observed in section 2.2.2. One can conclude, that nanowire growth with good selectivity takes place in a small temperature window between ~480–510 ℃ for the investigated V/III ratio.

Based on the trade-off between selectivity and nanowire length, an optimum substrate temperature of 480 ℃ was selected for all consecutive growth experiments. Fig. 5.9 illustrates that this temperature provided excellent selectivity and high vertical growth yield for a range of pitches and As fluxes. More in detail, Fig. 5.9a shows an AFM image of

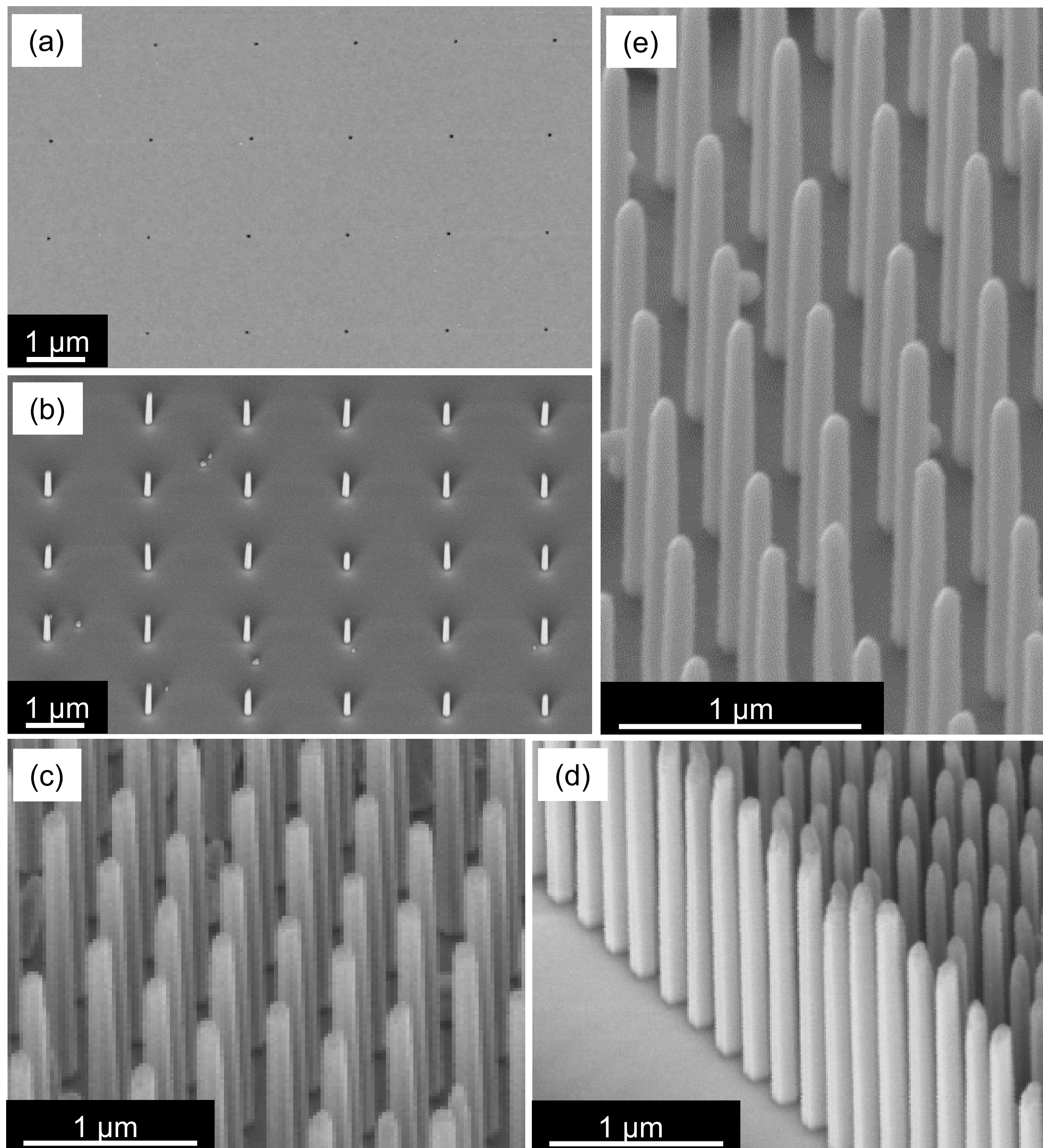

Figure 5.9. (a) AFM image of the pre-patterned SiO_2/Si(111) substrate with 2 µm pitch. (b) Tilted SEM image of 90 min MBE-grown, positioned InAs nanowires on a SiO_2/Si(111) substrate described in (a) at an As rate of 1.51 Å/s. The nanowires only nucleated in the holes and almost no InAs nucleated on the SiO_2 surface. (c) SEM image of InAs nanowires grown for 90 min with a higher As rate of 3.02 Å/s and a pitch of 500 nm. (d) SEM image of the same sample with a pitch of 250 nm. The electron micrograph shows the edge of the patterned field and demonstrates the excellent selectivity. The nanowire yield was improved to 90 % via optimized sample processing. (e) SEM image of nanowires grown on a substrate patterned by nanoimprint lithography with a pitch of 500 nm showing excellent yield (90 %) and selectivity. The nanowires were grown for 60 min with an As rate of 3.02 Å/s. Published in Ref. [Her10].

a representative patterned SiO_2/Si(111) wafer with 80-nm-wide openings (holes) and a pitch of 2 µm. The holes were processed as described in the previous section and had a depth of 17 nm. The SEM image shown in Fig. 5.9b evidences that all InAs nanowires nucleated at the pre-defined hole pattern (i.e., pitch of 2 µm) when grown under identical As flux conditions as before (1.51 Å/s). The nanowires have average diameters of 233 nm $\pm$ 8 nm and lengths of 1000 nm $\pm$ 57 nm. The diameters given here were determined as the averaged values from top and bottom of each nanowire. This approach provide direct information on nanowire tapering as discussed further below. Moreover, all nanowires exhibit hexagonal-shaped cross-section with surrounding $\{110\}$ side facets, similar to observations for non-selectively grown InAs nanowires as reported in section 2.2.1. Figs. 5.9c,d show SEM micrographs of InAs nanowires grown for 90 min with a higher As flux (i.e., 3.02 Å/s, BEP of 5.2×10^{-6} mbar) at two different pitches of 500 nm (Fig. 5.9c) and 250 nm (Fig. 5.9d). Fig. 5.9d was recorded at the edge of the patterned field and shows the intersection between unpatterned and patterned SiO_2 underlining further the very good growth selectivity. This growth resulted in nanowires with identical average diameters of $\sim$131 nm and lengths of $\sim$1.71 µm, which is an increase in aspect ratio (length/diameter) by a factor of two compared to nanowires grown at the low As flux conditions with comparable pitch of 250 nm. In accordance to section 2.2.4 this indicates that for the present growth parameters growth was performed in an In-rich growth regime.

Furthermore, in Fig. 5.9e InAs nanowires are presented which were grown on a SiO_2/Si(111) substrate patterned by nanoimprint lithography. In this case, the imprinted Si stamp was homemade via e-beam lithography with a 3 mm $\times$ 3 mm patterned area of 100-nm-high pillars exhibiting a diameter of 60 nm and a pitch of 500 nm. For details on the stamp fabrication see appendix A. The nanowires on this imprinted substrate were grown with identical parameters as used in Fig. 5.9c. The nanowire lengths and diameters as well as the very high yield of more than 90 % matches perfectly the results obtained for the growth on standard e-beam processed substrates, corroborating the high quality of nanoimprinted patterns.

The vertical nanowire yield of the growths presented in Fig. 5.9 averaged over $\sim$300 holes is 90 percent. The crucial finding to obtain nanowire arrays with such high yield depended on accurate pattern processing, including precise etching of the holes, but much less on nucleation conditions. Different attempts were carried out to vary nucleation conditions based on the relative time period between As_4 and In supply (i.e, t_{As}-t_{In}) as illustrated in Fig. 5.10a,b. In detail, a time variation of As_4 supply ranging from 30 min before opening, to 20 s after opening of the In shutter was studied. This can be referred to as As_4 pre-annealing (t_{As}-t_{In} = 30 min), simultaneous In/As_4 supply (t_{As}-t_{In} = 0), and In

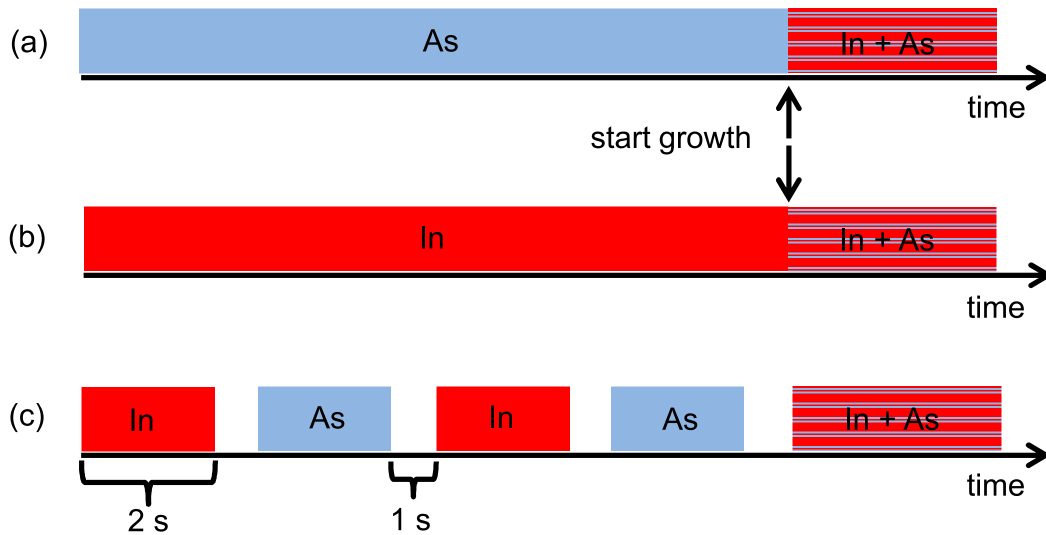

Figure 5.10. Schematic of different pre-wetting strategies, namely As (a) and In (b) pre-opening prior to nanowire growth. In (c) a flow rate modulation of In and As is applied in a 2 s alternating rhythm prior to nanowire growth. All pre-wetting experiments had no effect on the nanowire yield.

pre-wetting (t_{In}-t_{As} = 20 s). The time period for the In pre-wetting experiment correlates to an equivalent In coverage of less than ∼3 MLs. As_4 pre-annealing was also carried out at different substrate temperatures ranging from 350–480 ℃. All these different pre-wetting conditions showed no effect on the ratio of vertically aligned InAs nanowires. This indicates larger independence of the growth yield to the polar/nonpolar nature of the InAs/Si(111) heterointerface as previously identified in Ref. [Tom08]. In this report, which was based on non-catalytically grown InAs nanowires by MOCVD, a significant ratio of nanowires grew along three equivalent inclined <111> B orientations (i.e., tilted by 19.6° to the Si(111) surface) as illustrated in Fig. 5.11a. This finding seems to be a common observation in III–V nanowires on Si indicated by several reports [Mar04, Bak04, Par06]. Via refined modulated AsH_3/H_2 pre-wetting conditions at low temperature (depicted in Fig. 5.10c) a very high vertical nanowire growth yield could be achieved in Ref. [Tom08]. The difference with the experiments shown here may be related to the different surface chemistries in MBE and MOCVD processes, i.e., hydrogen- and carbon-containing precursors in MOCVD versus atomic III elements and molecular As_4 in MBE processes. Molecular As_4 is known to readily desorb at temperatures above ∼250 ℃ in UHV environment [Art66], therefore the time period of As_4 supply relative to In shuttering should have no influence on the surface kinetic properties during nanowire nucleation. Furthermore, comparison among different patterned fields with different pitches (such as in Fig. 5.9) resulted in consistently identical growth yields. This further implies significant independence of the growth yield from the interwire

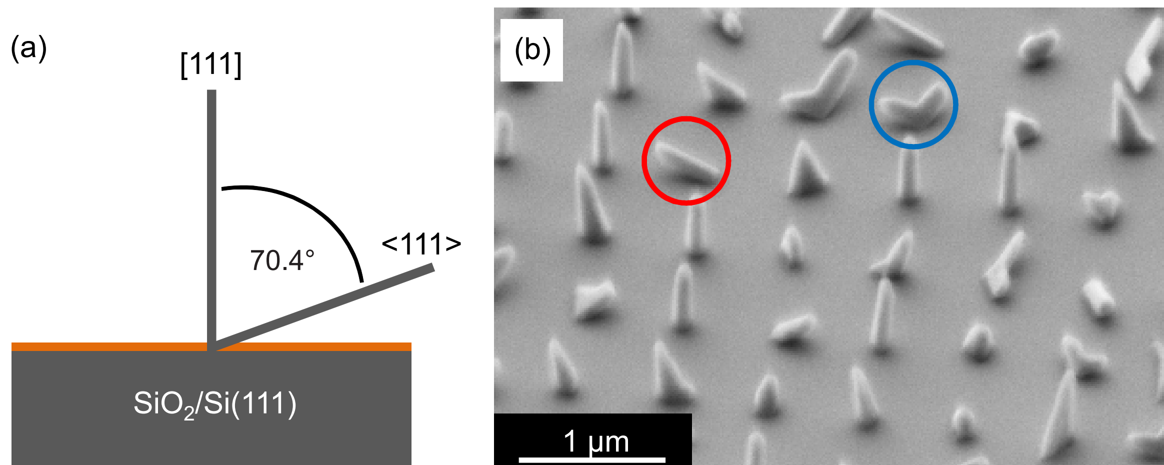

Figure 5.11. (a) Schematic of possible nanowire growth directions on a Si(111) substrate. Three equivalent <111> directions inclined by 70.4° with respect to the surface normal are in coexistence with the vertically aligned [111] growth direction. In (b) a SEM micrograph shows InAs nanowires grown on a patterned wafer with a hole depth of 30 nm, i.e., 20 nm in the SiO_2 layer and additional 10 nm in the Si substrate. An optimized etching technique without harming the Si wafer can suppress inclined nanowire growth.

distance and corresponding surface diffusion kinetics.

On the other hand, one needs to stress the importance of optimized pattern processing. In fact, a threefold increase in vertical nanowire growth yield from initially $\sim$30 % to finally $\sim$90 % was achieved by careful etching of the predefined holes. RIE etching with depths exceeding those of the SiO_2/Si(111) interface (i.e., etching into the Si substrate) resulted in poor vertical nanowire growth yields as evident in Fig. 5.11b. The SEM micrograph shows InAs nanowires grown on a patterned substrate with a hole depth of 30 nm, i.e., 20 nm in the SiO_2 layer and additional 10 nm in the Si substrate. Several nanowires are tilted by 70.4° with respect to the surface normal, growing along one of the three equivalent <111> directions (see nanowire marked by red circle), as also observed by Tomioka. In addition, some of the nanowires start to grow in two of the three <111> directions (marked by blue circle) leading to short V-shaped structures. The overall nanowire yield was decreased to only 30 % for this sample.

Furthermore, it has to be mentioned that remaining SiO_2 within the predefined holes leads to poor selectivity and very limited nanowire growth. As a conclusion, the optimized processing of a pattern for nanowire growth consists of reactive ion etching close to the Si substrate and subsequent HF etching of the final few nanometers of silicon oxide. This two-step technique combines the anisotropic etching characteristic of reactive ion plasma – resulting in straight cylindrical holes – with the harmlessness of HF with respect to silicon.

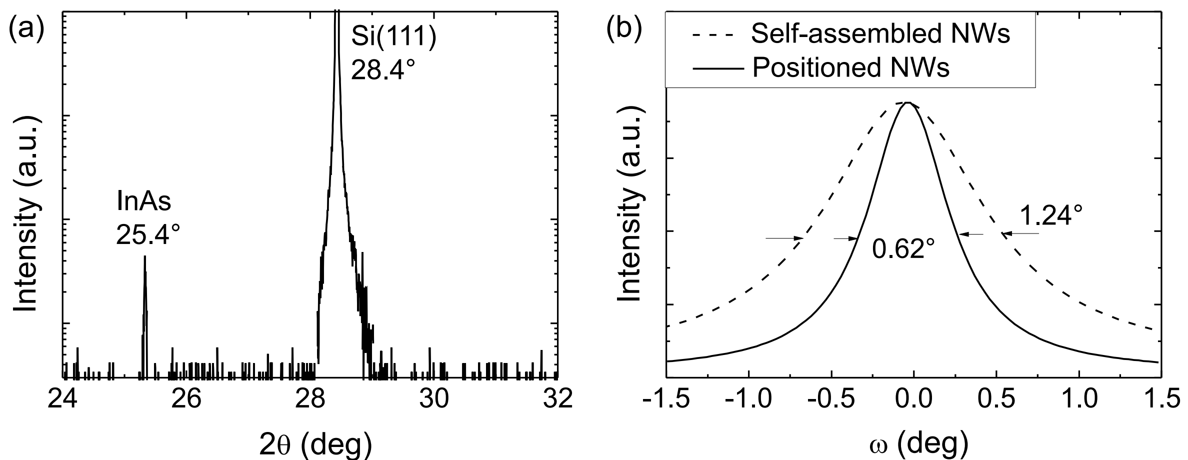

Figure 5.12. Double-crystal XRD 2θ–ω scan of the InAs nanowire array presented in Fig. 5.9b illustrating two peaks associated with InAs (25.4°) and the Si substrate (28.4°). (b) Normalized and fitted rocking curves (ω scans) of the InAs reflection (open detector) for the same site-selectively grown nanowire array in comparison with standard self-assembled nanowire arrays on sputter-deposited SiO_x/Si(111) substrate. Published in Ref. [Her10].

5.2.2 Vertical directionality and crystal tilt

To evaluate the epitaxial relationship and the large-scale directionality for the vertically aligned InAs nanowires with respect to the Si(111) substrate, XRD measurements were performed on the sample presented in Fig. 5.9b. The pattern of this sample was exposed over a large area of 5 mm $\times$ 5 mm to obtain a nanowire array large enough to provide a good signal intensity for X-ray measurements. A moderate pitch of 2 µm was selected to keep the e-beam exposure time reasonable. In Fig. 5.12a a representative XRD 2θ–ω scan is depicted, demonstrating that no other reflections than those associated with the InAs (i.e., 25.4°) and the Si orientations (i.e., 28.4°) are observed. This indicates the direct epitaxial relationship between the InAs nanowires and the Si(111) substrate reflecting the results for self-assembled InAs nanowires presented in Fig. 2.3. More importantly, the rocking curve peak width of the InAs reflection (ω scans) was measured with open detector, giving a full width at half maximum (FWHM) of 0.62° (Fig. 5.12b). This was compared with the rocking curve peak width of InAs nanowires grown by standard non-selective (i.e., self-assembled) technique on sputter-deposited SiO_x/Si(111) grown with identical parameters, which yielded a FWHM of 1.24°. Although the value measured for the non-selective technique is generally a good indication for well-oriented vertical nanowire arrays with low-crystal tilt, the lower FWHM (factor of 2) for the site-selective grown nanowire arrays proves even more effective suppression of crystal tilt by the present selective area

technique. The low FWHM value is further in good agreement with the state-of-the-art for the currently best-aligned semiconductor nanowire arrays [Par02, Han05]. Guaranteeing very low crystal tilt in the vertically well-oriented InAs nanowire arrays is essential for an unobscured analysis of the following growth kinetics effects.

5.3 Nanowire growth kinetics

5.3.1 Pitch and growth time dependent nanowire size

In the following, the morphologies and size variation of InAs nanowires grown at an As rate of 1.51 Å/s are investigated in more detail with respect to growth time and interwire (pitch) dependence. In Fig. 5.13 SEM images of positioned free-standing InAs nanowires are shown for different growth times of 10 min (a), 90 min (b, d), and 360 min (c) and variable pitches of 500 nm (a–c) and 2 µm (d). These different pitches correspond to nanowire densities ranging from 4×10^{8} cm^{-2} to 2.5×10^{7} cm^{-2}. Also the hole diameters were modified in the range 40–100 nm, however, the effect on nanowire diameter was insignificant. For instance, for a selected 1-µm-wide pitch only a slight increase in nanowire diameter from 133 nm to 143 nm was observed with increasing hole diameters in the range given above (not shown). The yield for this sample series presented in Fig. 5.13 was further found independent of growth time and pitch, as discussed earlier.

Fig. 5.13a provides further insight into the nanowire nucleation characteristics, as growth proceeded only for 10 min, resulting in small nanowires with lengths of 120 nm and diameters of 55 nm. The nanowires are obviously smaller than the holes, and the inset shows that they nucleated preferentially at the edge of each hole. This step-edge nucleation behavior is typical for preferential growth of site-selective nanostructures [Por07]. For longer growth times, the nanowires become longer and thicker and exhibit more whisker-like geometries, without deteriorating either the underlying hexagonal geometry nor altering the uniformity in diameter and morphology over the entire nanowire lengths (Fig. 5.13c).

To obtain further insight into the different growth kinetics effects, the size scaling behavior of the nanowires with growth time and as a function of pitch is shown in Fig. 5.14. It is found that the lengths of the nanowires scale linearly with time for the larger pitches, while for the smallest pitches, especially the 250-nm-wide pitch, the lengths decreased gradually for increased growth time (Fig. 5.14a). More specifically, for growth times of 10–90 min the length of the nanowires is nearly independent of pitch, whereas for growth times of 180 min and beyond significantly shorter nanowires are obtained for the smallest pitch, indicating a non-linear evolution of the growth rate as further shown below. Extrapolating the initial time

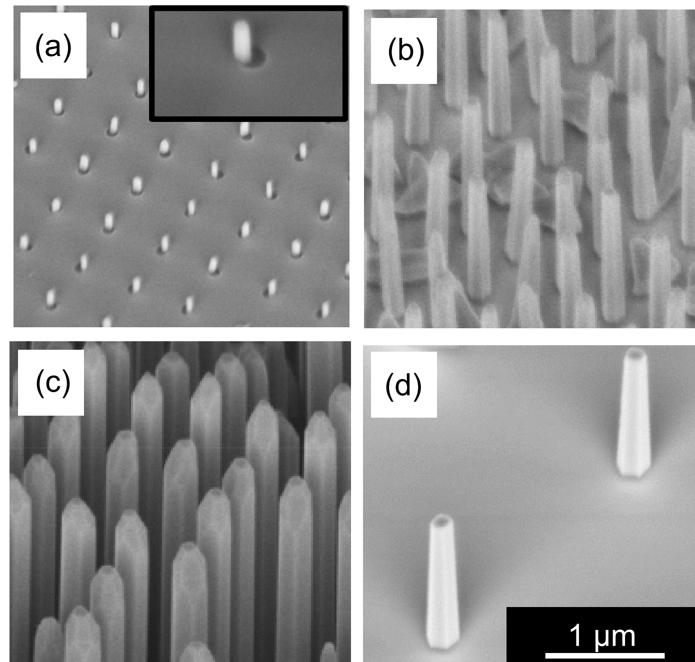

Figure 5.13. SEM images of positioned vertically grown InAs nanowires on Si(111) with an As rate of 1.51 Å/s and different growth times of 10 min (a), 90 min (b) and 360 min (c) are shown for a constant pitch of 500 nm. Furthermore, InAs nanowires grown for 90 min with a 2 µm pitch are presented in (d). The inset in (a) shows a close-up view of one hole with a diameter of 80 nm where a small nanowire nucleated at the edge of the hole. Published in Ref. [Her10].

evolution of the nanowire lengths to zero growth time suggests also that the nucleation time before nanowire growth was negligible. Along with the absence of metallic In droplets at the nanowire apex (see all previous SEM images), this gives further evidence for a non-catalytic nanowire growth mechanism as observed for self-assembled nanowire growth in chapter 3.

The size scaling effects are even more pronounced for the nanowire diameters (Fig. 5.14b), where a nearly linear increase in diameter is observed versus growth time for larger pitches (> 1 µm). The observation of increasing diameter with growth time is contrasting the typically negligible radial growth of catalytically-grown nanowires, where growth is restricted to adatom incorporation via the metallic droplet at the apex of the nanowire [Jen04]. For smaller pitches, however, the increase in diameter is only linear at the beginning of the growth, but saturates quickly after a certain time. For example, at 250 nm pitch the diameter saturates at $\sim$190 nm after 180 min and remains constant up to the longest analyzed growth time of 360 min. Although this diameter is very close to the interwire distance (pitch of 250 nm), the nanowires are still free-standing and entirely uncoalesced.

To understand these rate-limiting effects further the axial (Φ^{axial}) and radial (Φ^{radial}) growth rates were analyzed as a function of pitch and growth time more closely. The

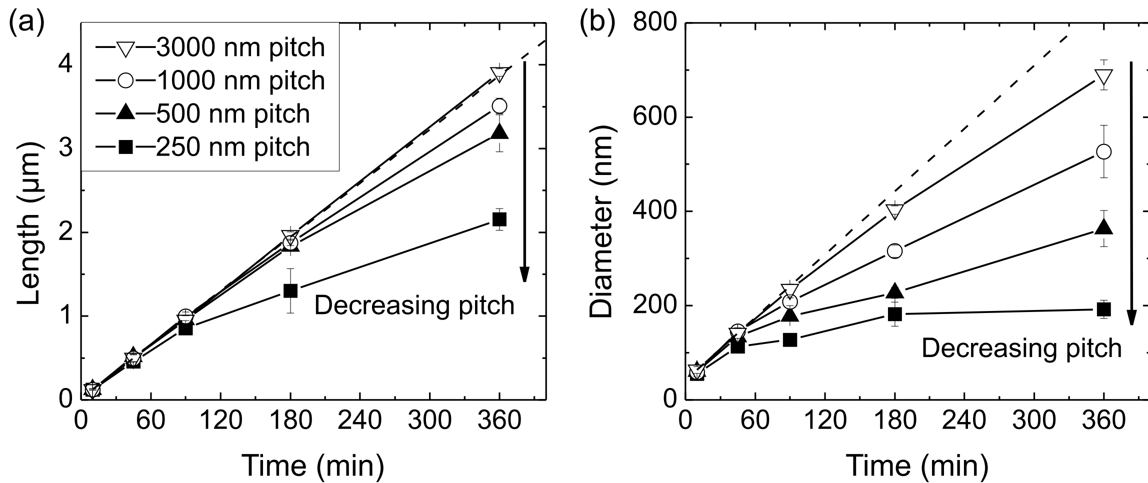

Figure 5.14. Analysis of length (a) and diameter (b) as a function of growth time for pitches ranging from 250 nm to 3 µm. Error bars were determined from averaging 20–30 nanowires per specific growth time and pitch. The dotted line is a guide to the eye and represents linear growth deduced from the points for 10 min and 45 min. Published in Ref. [Her10].

evolution of the growth rates over time, as illustrated in Fig. 5.15 for a wider range of pitches, shows clearly that nanowire growth was initiated at higher growth rates before reaching steady-state growth. Higher initial growth rates have been observed also for InAs nanowires grown by other methods [Day09, Jen04] and were associated with the different surface diffusion kinetics on the substrate and nanowire sidewalls. In particular, when the nanowire length (L) was shorter than the In adatom diffusion length along the nanowire sidewalls (λ_{NW}), then the capture area of impinging In adatoms on the nanowire sidewalls increases continuously with time, leading to fast superlinear growth. However, for longer growth times where $L > \lambda_{\mathrm{NW}}$, the capture area for In adatoms becomes rather constant leading to steady-state growth rates [Day09]. In addition, it can be suggested that the high initial growth rate may also stem from the underlying 3D island nucleation characteristics which often show typical power-law growth behavior, as observed for the self-assembled nanowires discussed in chapter 2.2.3. Nevertheless, upon transition to steady-state growth, the rates depend significantly on the pitch – i.e., the steady-state growth rates are completely identical for pitches above $\sim$2 µm (with constant Φ^{axial} and Φ^{radial} of $\sim$1.8 Å/s and $\sim$0.15 Å/s, respectively), while they are less and decrease gradually for lower pitches.

This interesting pitch dependence is a clear evidence of two particular growth regimes defined by the complex interplay between diffusion lengths of In adatoms on SiO_2 ($\lambda_{\mathrm{SiO_2}}$) and the adatom capture area with respect to selected pitch. Apparently, if the mean diffusion

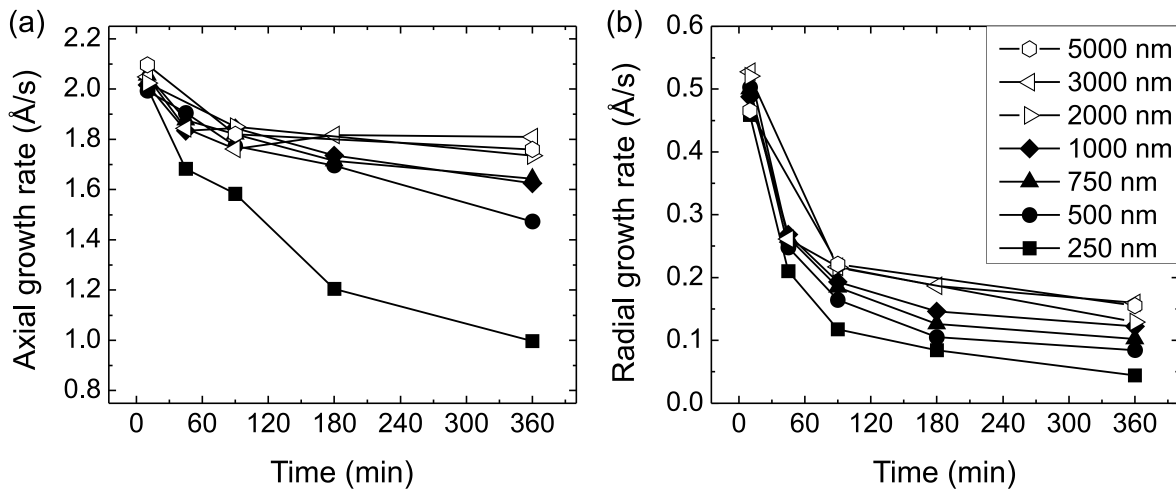

Figure 5.15. Time evolution of the (a) axial and (b) radial nanowire growth rates as derived from Fig. 5.14, indicating the initially higher growth rates during early nucleation and transition to steady-state growth. Published in Ref. [Her10].

length λ_{SiO_2} is on the order of or larger than half of the pitch, neighboring nanowires compete for adatoms to redistribute equally over the given nanowire density, which leads to a decrease in both vertical and radial growth rate. This rate-limiting **materials competition regime**, as previously examined also for GaP-based nanowires [Bor07], describes clearly the materials distribution under mass conservation over a fixed number of growing nanowires. According to this, increasing pitch corresponds to increased capture area for surface diffusing adatoms per individual nanowire which leads to increased growth rates.

On the other hand, when the surface diffusion length λ_{SiO_2} becomes less than one half of the pitch, the nanowires can be treated as independent isolated islands and growth is limited by the collection of the surface diffusing In adatoms. In this **diffusion-limited regime**, the growth rate therefore becomes independent of the pitch, resulting in completely identical rates, as confirmed here for pitches ranging from 2000–5000 nm. In this case, In adatoms which are not able to migrate further than the typical surface diffusion length cannot contribute to nanowire growth and either desorb or form clusters on the SiO_2 surface. Indeed, in selected SEM images traces of clusters are observed on the SiO_2 surface for pitches larger than $\sim$1500 nm (see for example Fig. 5.9b).

From the cross-over between the materials competition regime and the diffusion-limited growth regime one can determine the surface diffusion length of In adatoms λ_{SiO_2} under the given growth conditions. Since this cross-over occurred at a pitch of $\sim$1.5 µm, λ_{SiO_2} amounts therefore to $\sim$750 nm at the given growth temperature of 480 °C. This is further

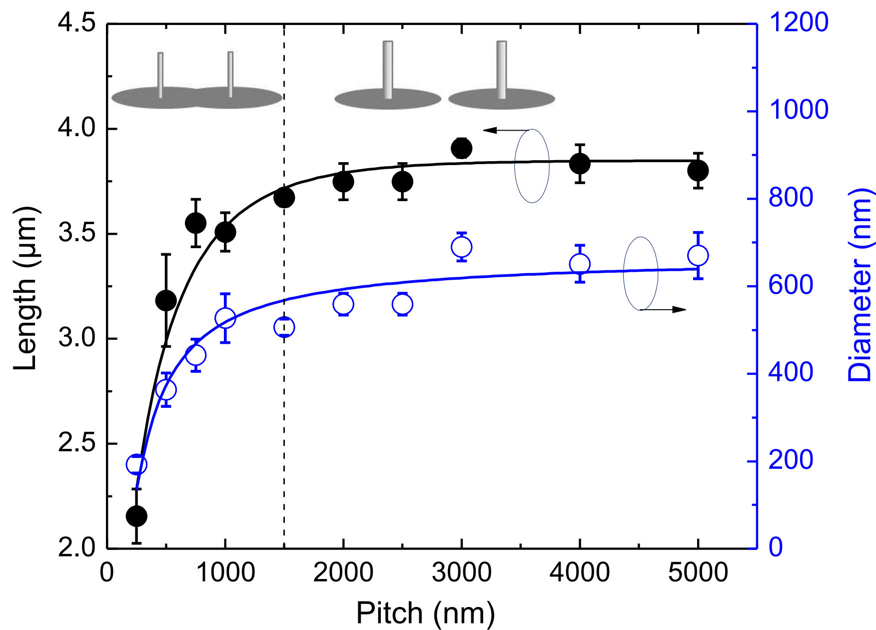

Figure 5.16. Dependence of nanowire length and diameter as a function of pitch for a fixed growth time (360 min). The transition to saturation in both length and diameter (as deduced from best fits to the data) indicates the cross-over from a competitive growth regime to a diffusion-limited growth regime (illustrated by dotted line). The inset illustrates nanowire growth in the competitive regime (left image) for pitches < $2\lambda_{SiO_2}$ and in the diffusion-limited regime (right image) for pitches > $2\lambda_{SiO_2}$. Published in Ref. [Her10].

corroborated in Fig. 5.16, showing the nanowire length and diameter dependence over a wide range of pitches resulting from a fixed growth time of 360 min. Clearly, both the nanowire length and diameter saturate at a pitch of around ~1.5 µm, in consistence with the previous growth rate analysis. Note that the nanowire diameter is neglected for this calculation and that its consideration would shift λ_{SiO_2} to lower values.

Moreover, despite the fact that the nanowires grown at the smallest pitches turned out to be the shortest in length, they simultaneously exhibited the largest aspect ratios (length/diameter), which even increased with growth time. This indicates that within the competitive growth regime direct impingement contributes significantly to vertical nanowire growth. This slows down the radial growth rate with increasing time, leading further to shadowing effects where less and less impinging adatoms can arrive and diffuse from the substrate surface. In contrast, in the diffusion-limited growth regime the aspect ratios were found constant and independent of the selected pitch, meaning that here direct impingement plays no role.

5.3.2 Effect of the As flux on the nanowire growth rates and tapering

The influence of As flux on the growth kinetics was discussed in section 2.2.4 for self-assembled InAs nanowire growth. However, the average nanowire distance was in the range of $\sim$200 nm and could not be controlled, i.e., the influence of the pitch could not be studied. The selective area epitaxy technique facilitates pitch dependent investigation of nanowire growth rates and tapering. In Fig. 5.17 the axial nanowire growth rate (a) and the nanowire diameter (b) are plotted for 2D equivalent As rates between 0.5 Å/s and 9.1 Å/s. Other parameters were fixed, i.e., growth temperature of 480 ℃, In flux of 0.24 Å/s and growth time of 90 min. The pitches of the investigated nanowire arrays were between 250 nm and 5 µm. Data analysis presented in this graph revealed findings that are in good agreement to the results on self-assembled InAs nanowire growth. First, for the investigated pitches a linear increase of axial growth rate (Φ^{axial}) is observed for As rates < 6 Å/s, whereas Φ^{axial} saturates for higher As fluxes beyond 6 Å/s. A similar behavior was found for self-assembled nanowire growth (see Fig. 2.10) where this distinctive transition was attributed to the change of effective As/In ratio from In-rich to As-rich conditions at the nanowire growth front.

Furthermore the axial nanowire growth rate is analyzed for different pitches, namely 250 nm, 1000 nm and 5000 nm. In the In-rich regime (low As fluxes) Φ^{axial} increases almost uniformly with As rate consistent with the findings in Fig. 5.9 for identical growth time (90 min). For higher As fluxes > 6 Å/s the nanowires grown with larger pitches of 1000 nm and 5000 nm exhibit slightly higher growth rates of 8.9 Å/s compared to 6.5 Å/s for the 250 nm pitch. The independence of Φ^{axial} from the pitch for lower As fluxes further corroborates the existence of an In-rich growth regime since changes of the effective In flux (as generated by varying the pitch) are not expected to influence the nanowire growth. Interestingly, in the As-rich regime (As rate > 6 Å/s) the pitch dependence is still not very pronounced and the transition point appears not to depend on the pitch. However, a larger In adatom collection area for larger pitches should shift the transition point toward higher As rates. An explanation of this counterintuitive behavior could be the notable number of InAs clusters and additional nanowires nucleated even in the absence of pre-patterned holes – as observed on the SiO_2 surface by SEM investigation (see Figs. 5.17c–e). The relatively low growth temperature of 480 ℃ is obviously insufficient to guarantee high enough In adatom diffusion under these excess As flux conditions. This results in an effective materials density (nanowires + cluster) much higher than the number of pre-patterned holes obscuring the pitch dependence of those nanowires. Increased growth temperatures will be necessary to grow InAs nanowires with good selectivity under excess As fluxes which is demonstrated in chapter 6.

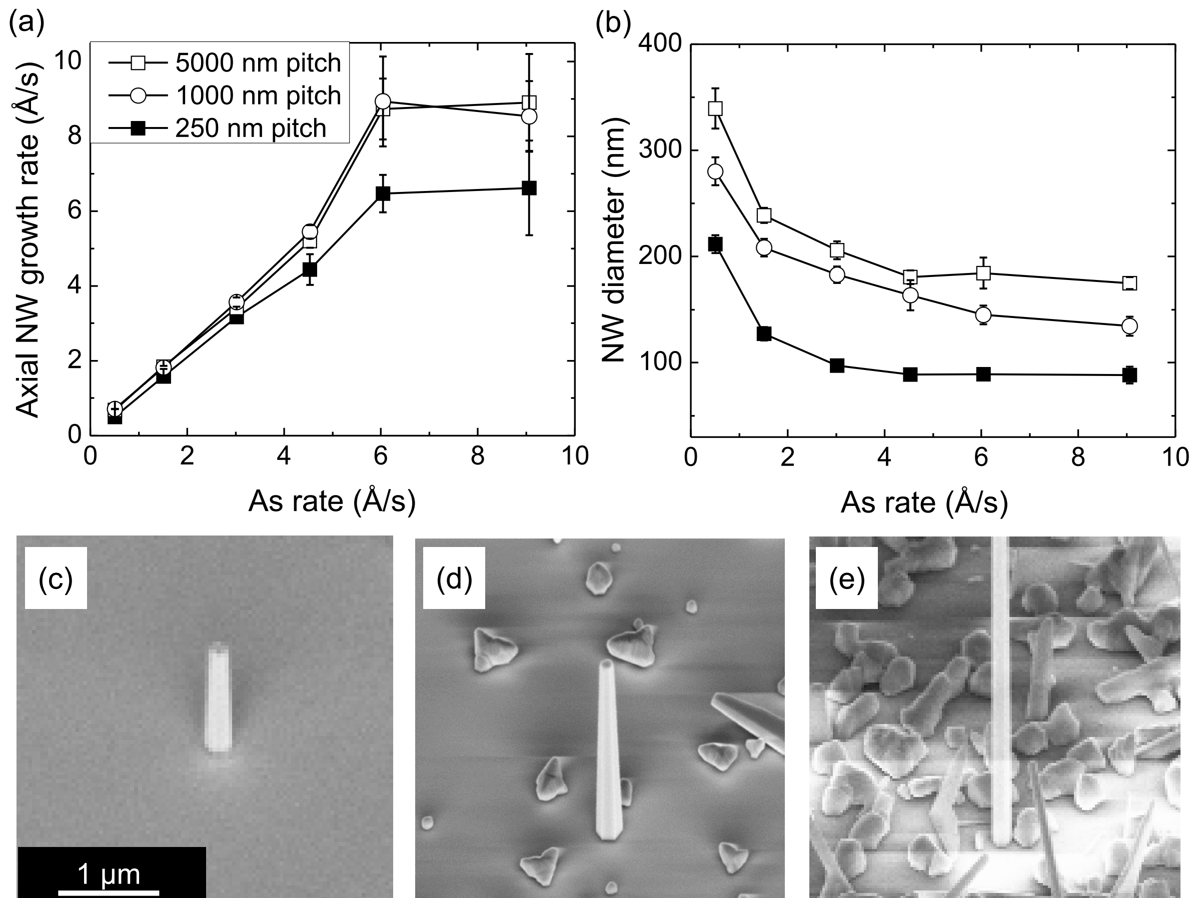

Figure 5.17. Axial nanowire growth rate (a) and diameter (b) plotted as a function of supplied As flux for fixed growth temperature (T = 480 °C), In flux (0.24 Å/s) and growth time (t = 90 min). Three curves reflecting different pitches (250 nm, 1000 nm and 5000 nm) are depicted and show a similar transition from linearly increasing growth rates to constant growth rates, similar to the findings for self-assembled InAs nanowire growth. Furthermore, three SEM images of the samples with 5 µm pitch are depicted for As rates of 1.5 Å/s (c), 3.0 Å/s (d) and 9.1 Å/s (e) revealing increased cluster formation for higher As fluxes. The cluster accumulation obscured the pitch dependence of nanowire length and diameter.

The analysis of the nanowire diameter further confirms the findings for self-assembled nanowire growth, i.e., a decreasing diameter for higher As fluxes in the In-rich growth regime and a constant diameter in the As-rich regime. This decrease is attributed to an enhanced InAs nanowire sidewall diffusion of In adatoms under higher effective As/In ratios as further discussed in section 2.2.4. Moreover, for high As fluxes low nanowire diameters of $\sim$90 nm were observed for the smallest pitch of 250 nm. Note that hole diameter dependent studies (not shown) using high As fluxes of 6.04 Å/s revealed identical nanowire diameters of $\sim$90 nm also for smaller holes, indicating a growth kinetics limit of the minimum nanowire

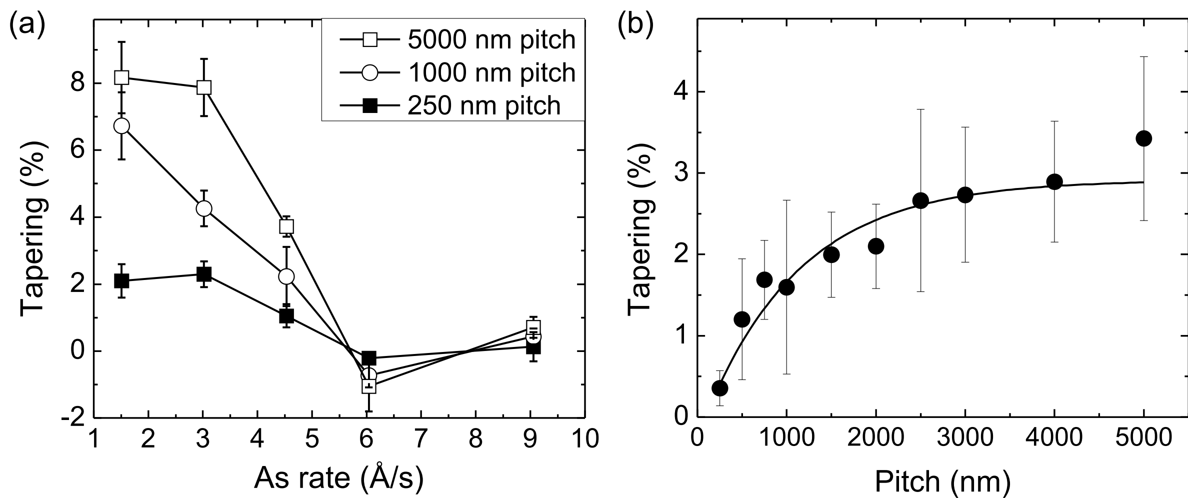

Figure 5.18. (a) InAs nanowire tapering as a function of As flux for pitches between 250 nm and 5000 nm. The nanowires were grown with fixed growth temperature (T = 480 ℃), In flux (0.24 Å/s) and growth time (t = 90 min). In (b) the tapering is plotted as a function of pitch for nanowires grown at T = 480 ℃ for 6 hours using In and As fluxes of 0.24 Å/s and 1.51 Å/s, respectively. The tapering factors for all investigated samples (typically 0–8 %) decreased for higher As fluxes and lower pitches. Inverse (negative) tapering has never been observed.

diameter. The larger pitches of 1000 nm and 5000 nm exhibited higher nanowire diameters of 135 nm and 175 nm, respectively.

Furthermore, the nanowire tapering of these samples was analyzed and is depicted in Fig. 5.18a where the tapering factors are plotted as a function of As flux for three different pitches of 250 nm, 1000 nm and 2000 nm. The tapering factors decrease with increasing As fluxes from $\sim$2–8 % for As rates of 0.5 Å/s to $\sim$0 % for As rates $\geq \sim$6 Å/s. This stems from the above mentioned enhanced In adatom diffusion, suppressing an incorporation at the $\{110\}$ facets of the nanowire. Moreover, under low As flux conditions, smaller pitches yielded much less tapered nanowires ($\sim$2 % for the 250 nm pitch) compared to larger pitches ($\sim$8 % for the 5000 nm pitch). For larger pitches more In adatoms impinge far away from a nanowire making a long diffusion on the SiO_2 surface necessary to reach the bottom of the wire. As a result enhanced sidewall incorporation reduces the probability for In adatoms to diffuse all the way up toward the nanowire tip. This leads to In incorporation gradients along the nanowire resulting in tapered wires. To further illustrate this effect the tapering factors are plotted vs. pitch (Fig. 5.18b) for nanowires grown for 6 h at an As rate of 1.51 Å/s. The tapering increased from the smallest pitch of 250 nm (tapering $\sim$0.3 %) to a saturated value of $\sim$2.9 % for pitches larger than 2 µm.

Overall, the tapering factors are between 0 % and 8 % with the highest tapering for the

lowest As flux and largest pitch. For As fluxes $\geq \sim$6 Å/s the tapering equals zero, i.e., the nanowires grow straight for all investigated pitches. Interestingly, in contrast to VLS grown III–As nanowires [Col08], inverse tapering was never observed. To summarize, changing of the V/III ratio highly influences the nanowire dimensions and can be utilized to readily design selected nanowire geometries. High As fluxes and low pitches yield long, untapered and rather thin nanowires.

5.4 Conclusion

In summary, catalyst-free site-selective growth of vertically well-oriented, high yield InAs nanowire arrays on Si(111) was established by solid-source molecular beam epitaxy. Important advantages of this growth approach were found in the independence of the vertical nanowire growth yield from pre-wetting conditions and the selected pitch (interwire distance), resulting in consistently high yields of $\sim$90 %. The excellent control of the vertical growth directionality was confirmed by very low crystal tilt in X-ray rocking curve measurements. Systematic investigations of the size scaling behavior as a function of the interwire distance highlighted the existence of two growth regimes within the non-catalytic growth processes: (i) a competitive growth regime for low interwire distances governed by redistribution of In adatoms over multiple nanowires as well as direct impingement, and (ii) a diffusion-limited growth regime, where growth is limited by the surface diffusion length of In adatoms on the SiO_2 surface ($\sim$750 nm at the given growth conditions). Here the radial and axial nanowire growth rates were found completely independent of the interwire distance, resulting in identical lengths and diameters. In good agreement to previous results on self-assembled nanowires an increase in As flux resulted in longer and thinner nanowires for effective As/In ratios < 1. For higher effective As/In ratios > 1 constant axial nanowire growth rates and nanowire diameters were found, meaning that the aspect ratio remains fixed for different As fluxes. Finally, the nanowire tapering was investigated where decreased tapering factors for higher As fluxes and lower pitches were observed. Inverse (negative) tapering was not observed evidencing a droplet-free non VLS growth mode, corroborating the results of chapter 3.

6

InGaAs nanowire growth and related optical properties

In this chapter ternary $In_{1-x}Ga_xAs$ nanowire growth is investigated over almost the entire composition region. The nanowires are grown both in self-assembled manner on sputter-deposited SiO_x/Si(111) and site-selectively on a SiO_2/Si(111) substrate patterned by nanoimprint lithography. The large-scale nanowire arrays facilitate straightforward investigation of the nanowire composition via X-ray diffraction. Furthermore, optical analysis by means of Raman and photoluminescence spectroscopy are provided. In particular, a comparison of the two different growth strategies with respect to homogeneity in composition is elaborated and discussed. The results presented in this chapter are published in Ref. [Her12b].

6.1 Growth of InGaAs nanowires on Si

$In_{1-x}Ga_xAs$ nanowire growth was performed under As-rich conditions with Φ^{As} = 20.3 Å/s and a fixed total group-III flux Φ^{Ga} + Φ^{In} = 0.36 Å/s [As/(Ga+In) ratio = 56.5]. To achieve composition tuning of the $In_{1-x}Ga_xAs$ nanowires with variable Ga content x(Ga), the $\Phi^{Ga}/(\Phi^{In}+\Phi^{Ga})$ ratio was adjusted while fixing the total group-III flux. Growth temperature and time were also fixed at T = 550 °C and t = 1 hour, unless otherwise noted. These growth conditions are adapted from previous studies of InAs nanowire growth on Si(111) as reported in section 2.2.2, where optimized As/In ratio provided access to high-T growth regimes necessary for sufficient Ga diffusion and incorporation in ternary (111)-oriented InGaAs nanowires. InGaAs nanowire growth is initiated by simultaneously opening the In and Ga shutter while the As shutter has already been open for a few minutes for flux stabilization. Two different growth strategies are investigated, i.e., self-assembled nanowire growth on sputter-deposited SiO_x/Si(111) and site-selective growth on a SiO_2/Si(111) substrate patterned by nanoimprint lithography (NIL). For details on the substrate preparation for self-assembled and site-selective (by NIL) nanowire growth see sections 2.1 and 5.1.2.

Fig. 6.1 shows representative images of site-selectively grown $In_{1-x}Ga_xAs$ nanowire arrays on NIL-SiO_2/Si(111) substrates for various different $\Phi^{Ga}/(\Phi^{In}+\Phi^{Ga})$ ratios. The upper panel of Fig. 6.1a shows a photograph of the corner region between the imprinted/regrown area (in black) and the surrounding unpatterned SiO_2 area (in gray), demonstrating the excellent NIL fabrication and InGaAs nanowire growth selectivity. The lower panel shows a magnified top-view SEM image of the same InGaAs nanowire array, which was grown with a $\Phi^{Ga}/(\Phi^{In}+\Phi^{Ga})$ ratio of 0.1. This image evidences very high periodicity and high vertical, i.e., (111)-oriented growth yield of the as-grown InGaAs nanowires, confirming the direct epitaxial relationship between the nanowires and the Si(111) substrate.

A more direct, i.e., bird's eye view of the InGaAs nanowire arrays is shown in the corresponding SEM images of Figs. 6.1b–d for different $\Phi^{Ga}/(\Phi^{In}+\Phi^{Ga})$ ratios of 0.1 (b), 0.3 (c) and 0.5 (d). Note that under the optimized imaging conditions (without tilt correction), the nanowires appear much shorter (factor of $\sim$3) than their actual lengths, i.e., the latter ranging from $\sim$1.3 µm for $\Phi^{Ga}/(\Phi^{In}+\Phi^{Ga})$ ratio = 0.1 (Fig. 6.1b) to $\sim$1.0 µm for $\Phi^{Ga}/(\Phi^{In}+\Phi^{Ga})$ ratio = 0.5 (Fig. 6.1d). Interestingly, the as-grown nanowires show a completely non-tapered morphology independent of the supplied $\Phi^{Ga}/(\Phi^{In}+\Phi^{Ga})$ ratio as was already observed for In flux dependent studies for binary InAs nanowire growth (see section 2.2.4). This observation, together with the absence of any macroscopic group-III elemental droplet (self-catalyst), mimics the VLS-free growth characteristics as verified for binary InAs and GaAs nanowires on SiO_2/Si(111) under these conditions (see chapter 3

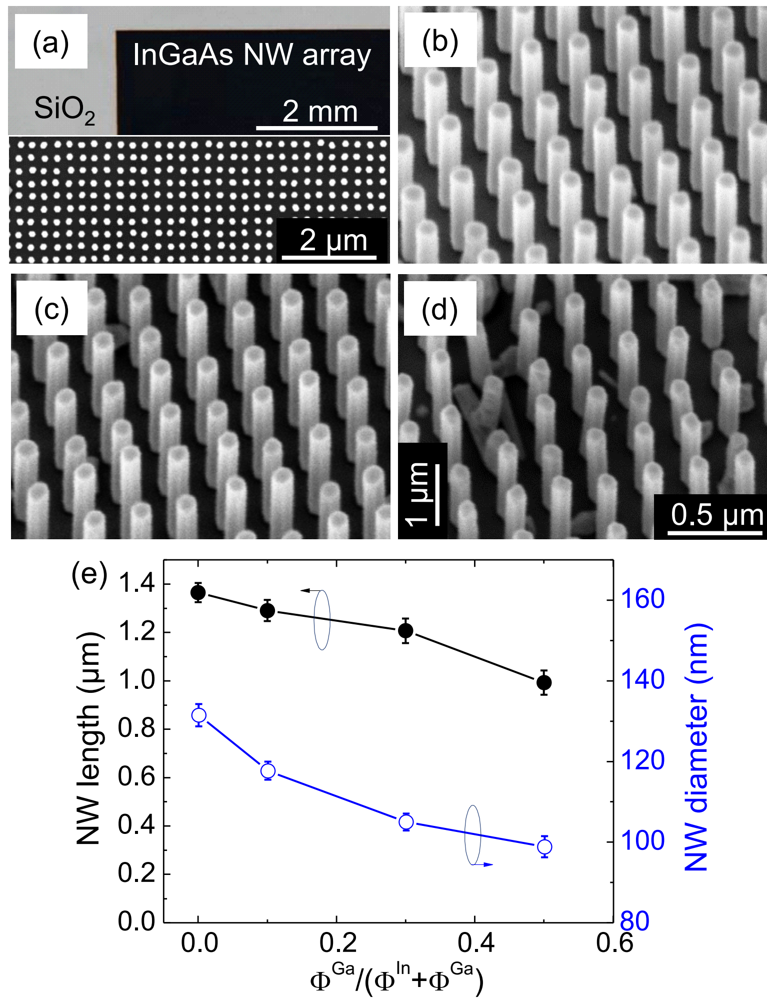

Figure 6.1. (a) Photograph (upper panel) and corresponding top-view SEM image (lower panel) of a site-selectively grown $In_{1-x}Ga_xAs$ nanowire array on NIL-SiO_2/Si(111) using a $\Phi^{Ga}/(\Phi^{In}+\Phi^{Ga})$ ratio of 0.1. (b–d) Close-up SEM images in bird's eye view (tilt angle 20° to the surface normal) of (b) the same $In_{1-x}Ga_xAs$ nanowire array as viewed in (a), and $In_{1-x}Ga_xAs$ nanowire arrays grown under different $\Phi^{Ga}/(\Phi^{In}+\Phi^{Ga})$ ratios of 0.3 (c) and 0.5 (d). Note the different length scales laterally and vertically as resulting from optimized imaging conditions (without tilt correction). (e) Averaged length and diameter of binary InAs nanowires and the three nanowire samples shown in (b–d). Published in Ref. [Her12b].

and Ref. [Rud11]). Concurrent with the decreasing nanowire length, the nanowire diameter also decreases slightly with increasing $\Phi^{Ga}/(\Phi^{In}+\Phi^{Ga})$ ratio as shown in Fig. 6.1e. This slight decrease in nanowire volume could arise from: (i) limited diffusivity and/or enhanced desorption of In in the presence of Ga adatoms at the nanowire sidewall and top surfaces, as well as (ii) onset of parasitic InGaAs growth on the SiO_2, which however becomes only effective at the highest $\Phi^{Ga}/(\Phi^{In}+\Phi^{Ga})$ ratio of 0.5 (see Fig. 6.1d). Hence, the former is anticipated as the most likely rate limiting mechanism.

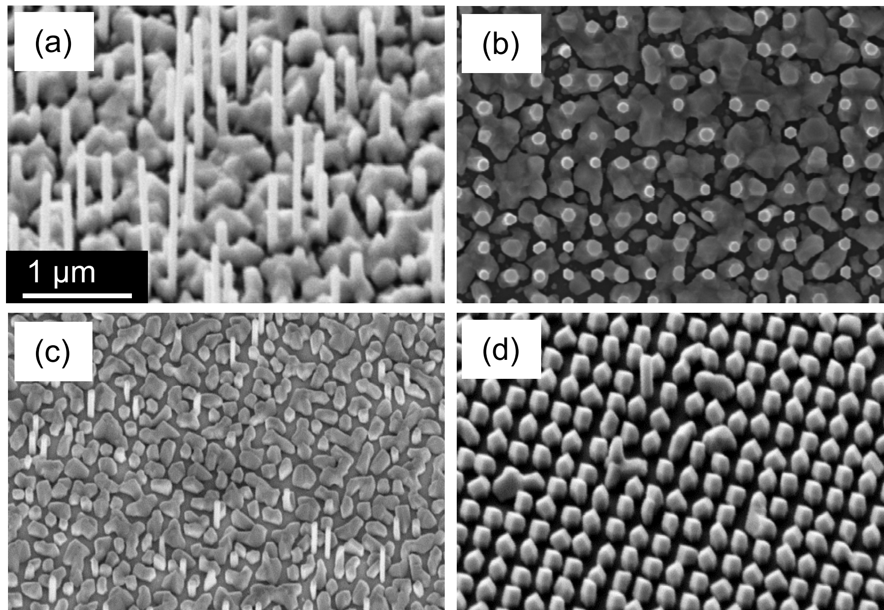

Figure 6.2. SEM images in tilted (a) and top-view (b) perspective of $In_{1-x}Ga_xAs$ nanowire arrays using a high $\Phi^{Ga}/(\Phi^{In}+\Phi^{Ga})$ ratio of 0.7 at a growth temperature of 550 ℃. For additional experiments using a $\Phi^{Ga}/(\Phi^{In}+\Phi^{Ga})$ ratio of 0.85 the growth temperature was increased to 580 ℃ (c) and 590 ℃ (d) to reduce heavy parasitic growth. The growth temperature of 590 ℃ (d) results in locally well-defined hexagonal-shaped crystal growth rather than in nanowire growth. Note that the growth selectivity is excellent, i.e., parasitic growth is completely suppressed.

In addition, Fig. 6.2 shows tilted (a) and top-view (b) SEM micrographs of growths with higher $\Phi^{Ga}/(\Phi^{In}+\Phi^{Ga})$ ratio of 0.7 for otherwise identical growth parameters (T = 550 ℃). This growth resulted in the successful formation of nanowires, although with much lower growth yield and nanowire volume due to significant parasitic growth under the given growth conditions. As a consequence of the heavy parasitic growth, the nanowire lengths fluctuate significantly yielding an average length of L = 879 nm $\pm$ 236 nm. For InGaAs nanowire growth with even higher $\Phi^{Ga}/(\Phi^{In}+\Phi^{Ga})$ increased growth temperature is expected to bypass the cluster formation. The Figs. 6.2c and 6.2d show InGaAs nanowires grown with a $\Phi^{Ga}/(\Phi^{In}+\Phi^{Ga})$ ratio of 0.85 at temperatures of 580 ℃ and 590 ℃, respectively. The increased temperature of 580 ℃ results in short nanowires ($\sim$500 nm) with poor growth yield while a further increase of growth temperature to 590 ℃ led to well-defined hexagonal-shaped crystals with good selectivity which appear with large diameter but very short length. The extreme reduction in nanowire length can be explained by increased In and Ga adatom desorption for increased growth temperature as well as limited group-III element supply. Optimization of growth temperature and supplied fluxes is expected to improve the quality of InGaAs nanowire growth for $\Phi^{Ga}/(\Phi^{In}+\Phi^{Ga})$ ratios larger than 0.5.

6.2 X-ray diffraction of InGaAs nanowires

To determine the actual composition of the $In_{1-x}Ga_xAs$ nanowire arrays grown under the different $\Phi^{Ga}/(\Phi^{In}+\Phi^{Ga})$ ratios, 2θ–ω HRXRD scans were recorded and the Ga content x(Ga) determined using Vegard's law under the assumption that the nanowires are completely relaxed. Here, the as-measured peak reflections of InAs (2θ = 25.33°) and GaAs (2θ = 27.32°) were taken as the binary boundary conditions from which the alloy composition was linearly interpolated for the different $In_{1-x}Ga_xAs$ nanowire samples via shifts in 2θ peak position (and respective lattice constant). Fig. 6.3a shows the 2θ–ω HRXRD scans of $In_{1-x}Ga_xAs$ nanowire arrays normalized with respect to the peak intensity of binary InAs nanowires, yielding x(Ga) of 0.07, 0.19, 0.36 and 0.59 for supplied $\Phi^{Ga}/(\Phi^{In}+\Phi^{Ga})$ ratios of 0.1, 0.3, 0.5 and 0.7, respectively. Note that besides the Si(111) substrate peak at 2θ = 28.44° and the composition-dependent $In_{1-x}Ga_xAs$ nanowire 2θ-peaks no other reflections are observed over a large 2θ range of 0–60°. In addition, the XRD-measured Ga content x(Ga) was verified independently via chemical analysis using EDX on selected samples. The Ga content was determined via intensity ratios of the respective K_α transitions (In/As and Ga/As). The Ga contents as measured by HRXRD and EDX mapping were found to be in very good agreement. For example, the $In_{1-x}Ga_xAs$ nanowire sample grown with $\Phi^{Ga}/(\Phi^{In}+\Phi^{Ga})$ ratio of 0.3 yielded x(Ga) = 0.19 by HRXRD and x(Ga) = 0.20 $\pm$ 0.02 (experimental error) by EDX measured at 4 nanowires.

The full width at half maximum (FWHM) values of the $In_{1-x}Ga_xAs$ nanowire-related HRXRD-2θ peak widths were determined to evaluate whether significant composition inhomogeneities and phase separation are present across the entire arrays. For this analysis, all $In_{1-x}Ga_xAs$ peaks with x(Ga) $\leq$ 0.19 were best fitted by a single Voigt function, while the $In_{1-x}Ga_xAs$ peak with x(Ga) = 0.36 and 0.59 – which exhibit some asymmetry – were best fitted by two Voigt functions indicated in gray. The peak maxima are at 2θ = 26.037° and 26.065° for x(Ga) = 0.36 and 2θ = 26.484° and 26.552° for x(Ga) = 0.59. Note that the peaks which fit the asymmetric shoulder at 2θ = 26.065° and 2θ = 26.552°, respectively, are related to the zincblende (111) reflection and stem from parasitic clusters formed in between the nanowires for these particular growths (see also section 4.1.2). On the other hand, the major peaks at 2θ = 26.037° and 2θ = 26.484° are associated with the nanowire-based wurtzite (002) reflection, in similarity to the single (002) peak reflection observed for all other cluster-free $In_{1-x}Ga_xAs$ nanowire arrays grown with lower x(Ga). The dominant wurtzite-type crystal structure has been also verified by TEM for this composition-dependent series. Further details on the crystal structure as measured by complementary HRXRD and TEM are given in section 4.1. Most interestingly, comparison

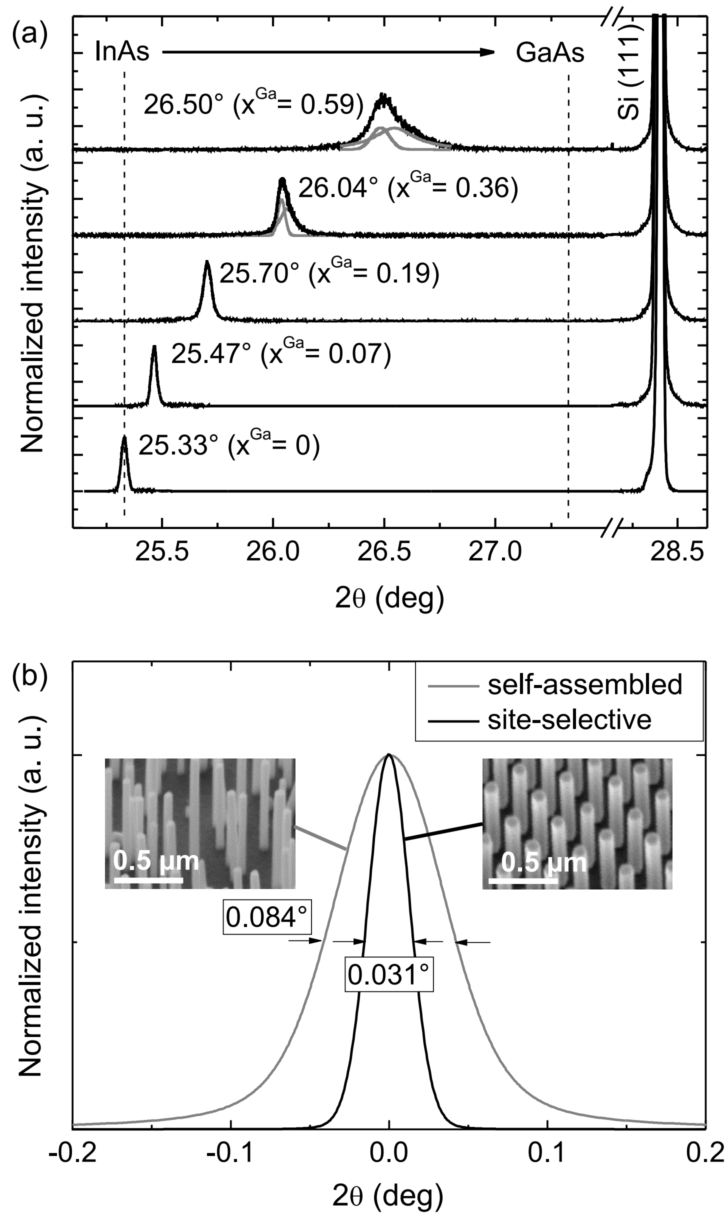

Figure 6.3. HRXRD 2θ–ω scans of several site-selective $In_{1-x}Ga_xAs$ nanowire arrays on NIL-SiO_2/Si(111) grown under the different $\Phi^{Ga}/(\Phi^{In}+\Phi^{Ga})$ ratios as given in Table 6.1. Dashed lines indicate the 2θ peak positions of binary InAs and GaAs (as measured), facilitating linear interpolation of the actual Ga content x(Ga) from the respective 2θ peak positions (i.e., lattice constants) of the $In_{1-x}Ga_xAs$ nanowire arrays via Vegard's law. The two upper scans [x(Ga) = 0.36 and 0.59] show two fitted curves (Voigt functions, in gray), corresponding to wurtzite-based nanowire and zincblende-based cluster signatures, respectively. (b) Normalized intensity of the 2θ-InGaAs peak position after Voigt fitting (fixed at 2θ = 0°) comparing similarly grown site-selective $In_{1-x}Ga_xAs$ nanowires [x(Ga) = 0.07, black] and self-assembled $In_{1-x}Ga_xAs$ nanowires [x(Ga) = 0.08, gray]. Insets illustrate representative SEM images of the two different types of nanowires. HRXRD 2θ–ω scans are performed with beam size of $\sim$3x4 mm^2 and a 1/8° aperture at the detector. Published in Ref. [Her12b].

of all fitted nanowire-related peak widths for x(Ga) = 0–0.36 gives very similar FWHM values between 0.031–0.039°. This indicates rather low degree of composition inhomogeneity for the site-selectively grown $In_{1-x}Ga_xAs$ nanowire arrays (see Table 6.1), much lower than recently reported for self-assembled $In_{1-x}Ga_xAs$ nanowires on Si [Shi11].

Table 6.1. Summarized data of nanowire length (L) and diameter (D) dispersion, HRXRD measured Ga content x(Ga) and FWHM of the InGaAs-related 2θ-peak reflection for several $In_{1-x}Ga_xAs$ nanowire arrays grown under different $\Phi^{Ga}/(\Phi^{In}+\Phi^{Ga})$ ratios. The data compares selective area grown (SAG) nanowires on NIL-SiO_2/Si(111) (growth time of 60 min) with self-assembled nanowires on non-lithographically prepared SiO_x/Si(111) (growth time of 24 min). Data labeled with an asterisk (*) refers to the nanowire-based signature in the 2θ–ω scan of Fig. 6.3a as derived from peak fitting analysis (Voigt function).

growth type	$\Phi^{Ga}/(\Phi^{In}+\Phi^{Ga})$	L (nm)	D (nm)	x(Ga)[XRD]	2θ-FWHM (°)
SAG	0	1365 ± 40	131 ± 2.7	0	0.031
	0.1	1290 ± 44	118 ± 2.2	0.07	0.031
	0.3	1207 ± 50	105 ± 2.1	0.19	0.039
	0.5	993 ± 50	99 ± 2.6	0.36	0.039*
Self-assembly	0	860 ± 88	83 ± 7	0	0.031
	0.1	645 ± 124	65 ± 7	0.08	0.084
	0.2	681 ± 68	81 ± 5	0.15	0.084
	0.3	423 ± 80	73 ± 9	0.19	0.091

Significantly broader FWHM values are determined under identical measurement conditions for $In_{1-x}Ga_xAs$ nanowire arrays grown in a self-assembled manner on non-lithographic SiO_x/Si(111) templates. Fig. 6.3b provides a direct comparison between the 2θ-(InGaAs)-FWHM values of a site-selective $In_{1-x}Ga_xAs$ nanowire array [x(Ga) = 0.07] and a self-assembled $In_{1-x}Ga_xAs$ nanowire array [x(Ga) = 0.08], which were grown under similar conditions. While the FWHM value for the site-selectively grown nanowire array is as small as 0.031°, the respective value for the self-assembled array is more than a factor of 2 larger (FWHM = 0.084°). Interestingly, the FWHM values of site-selective and self-assembled binary InAs nanowire arrays are completely identical (0.031°, see Table 6.1). This observation suggests that the broadened 2θ-peak width for the self-assembled $In_{1-x}Ga_xAs$ nanowires is related to inhomogeneities caused by composition fluctuations across the nanowire array. Such phenomena can be readily understood in terms of the spatially random distribution of self-assembled nanowires (as exemplified in the left SEM image of Fig. 6.3b), where differences in the interwire distance may lead to variable collection and incorporation efficiencies of the group-III species between different nanowires via competitive processes (see section 5.3). Hence, not only larger composition inhomogeneities but also much larger dispersion in nanowire length and diameter are observed, although the nanowire densities

are comparable between the two samples ($\rho^{NW} \sim 2 \times 10^9$ cm^{-2}). It should be emphasized that this tendency for broadened 2θ-peak widths for self-assembled $In_{1-x}Ga_xAs$ nanowires appears to be consistent also for other x(Ga) with FWHM values generally larger than 0.084° (see Table 6.1). This limitation to relatively large size and composition dispersion mimics previous findings obtained for InGaAs quantum dot systems grown in self-assembled fashion [How06].

It has to be mentioned that the sample grown on the NIL-patterned substrate using the highest $\Phi^{Ga}/(\Phi^{In}+\Phi^{Ga})$ ratio of 0.7 [x(Ga) = 0.59] exhibits a 2θ-peak FWHM of 0.099°, similar to the samples grown in a self-assembled manner. This is obviously due to heavy parasitic growth and poor growth yield, which naturally leads to much larger dispersion in aspect ratio and hence composition across the arrays.

6.3 Optical analysis by Raman and PL spectroscopy

To confirm the larger disorder and dispersion in the self-assembled nanowires with respect to the site-selective nanowires, µ-Raman spectroscopy was performed in backscattering geometry on nanowire ensembles dispersed onto a Si substrate. The laser was operated with an excitation power of 2.41 eV and a laser spot size of $\sim$2 µm (NA = 0.4). Since the nanowires lay randomly oriented on the substrate, the measurements represent the average of two orthogonal polarization configurations with no polarization selection for the scattered light. Representative Raman spectra are presented in Fig. 6.4 as obtained from measurements on self-assembled and site-selective $In_{1-x}Ga_xAs$ nanowire ensembles grown with completely identical Ga content x(Ga) = 0.19. Note that Raman intensities are normalized to the TO phonon mode, where the $In_{1-x}Ga_xAs$ related TO and LO phonon modes are found at 219 $\pm$ 1 cm^{-1} (InAs-like TO), 232 $\pm$ 2 cm^{-1} (InAs-like LO), 245 $\pm$ 1 cm^{-1} (GaAs-like TO) and 256 $\pm$ 1 cm^{-1} (GaAs-like LO), respectively. The broad spectral feature centered around 150 cm^{-1} is attributed to second order and disorder activated acoustical modes. Since disorder-induced effects are, however, mainly seen in the activation of the LO phonon modes [Hoe11], specific focus on these signatures is addressed. Although both the InAs-like LO and GaAs-like LO modes are of finite intensity, important differences between the two investigated samples can be derived from the relative (LO/TO) intensities.

As can clearly be seen from Fig. 6.4, the LO modes broaden and are higher in relative intensity (increased LO/TO ratio) for the self-assembled nanowires. For a more quantitative analysis, Lorentzian peak fitting of the LO and TO phonon modes was conducted (fitted curves indicated as solid lines) and the individual fits of the important disorder-sensitive InAs-like and GaAs-like LO modes are shown as dashed lines (displayed by offsets). The

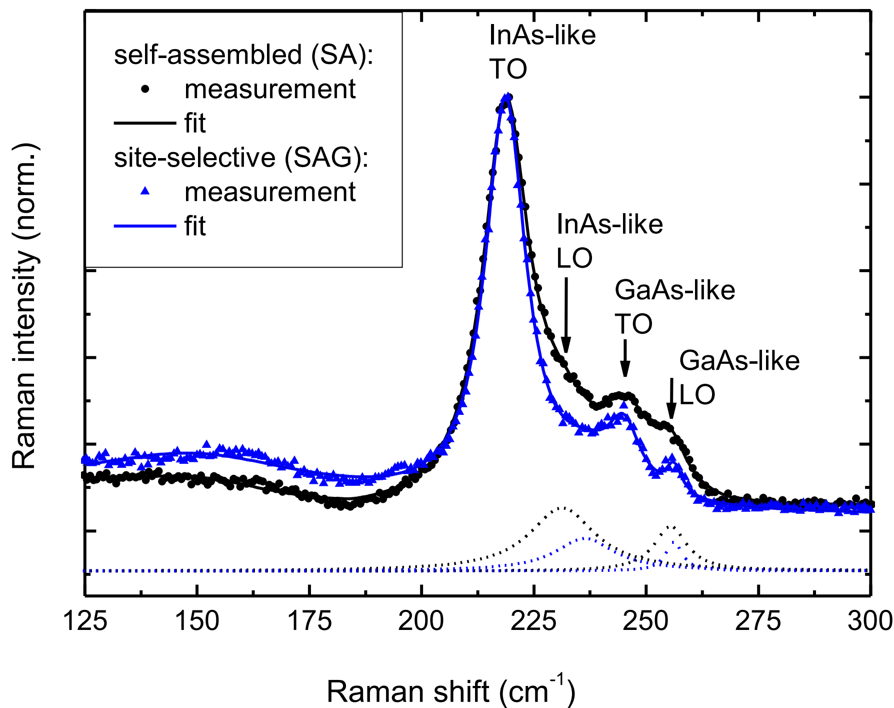

Figure 6.4. Raman spectra of site-selective (SAG, in blue) and self-assembled (SA, in black) $In_{1-x}Ga_xAs$ nanowires with identical x(Ga) = 0.19, measured under identical conditions. Spectra are normalized to the InAs-like TO phonon peak and a multiple-Lorentzian fitting was conducted (solid lines). Fits of the disorder-sensitive LO modes (InAs- and GaAs-like) are shown as dashed lines (offset for visibility). Note the obvious increase in LO/TO ratio and LO-FWHM for both the InAs- and GaAs-like LO modes in the case of self-assembled nanowires. Published in Ref. [Her12b].

fits for the LO modes directly evidence increased relative LO/TO intensity and increased LO-FWHM for both the InAs-like and GaAs-like LO modes in the case of self-assembled growth. Interestingly, the described differences were absent when comparing binary self-assembled and site-selective nanowires, i.e., pure InAs NWs [x(Ga) = 0]. This supports the conclusion that the disorder-mediated effects are mainly caused by composition inhomogeneities across arrays of self-assembled $In_{1-x}Ga_xAs$ nanowires.

To further substantiate the higher uniformity for the site-selectively grown $In_{1-x}Ga_xAs$ nanowire arrays, additional low-temperature PL spectroscopy (at 20 K) was performed on these types of nanowires. Interestingly, due to the excellent periodicity of the vertically aligned nanowire arrays no PL emission was observed by excitation under normal incidence to the sample surface. This unique behavior can be traced to the formation of 2D photonic bands, where emission is preferentially guided into photonic bands in the plane and not perpendicular to the sample surface, such that the emitted light cannot effectively reach the detector. Hence, for successful probing of the PL emission, the free-standing $In_{1-x}Ga_xAs$

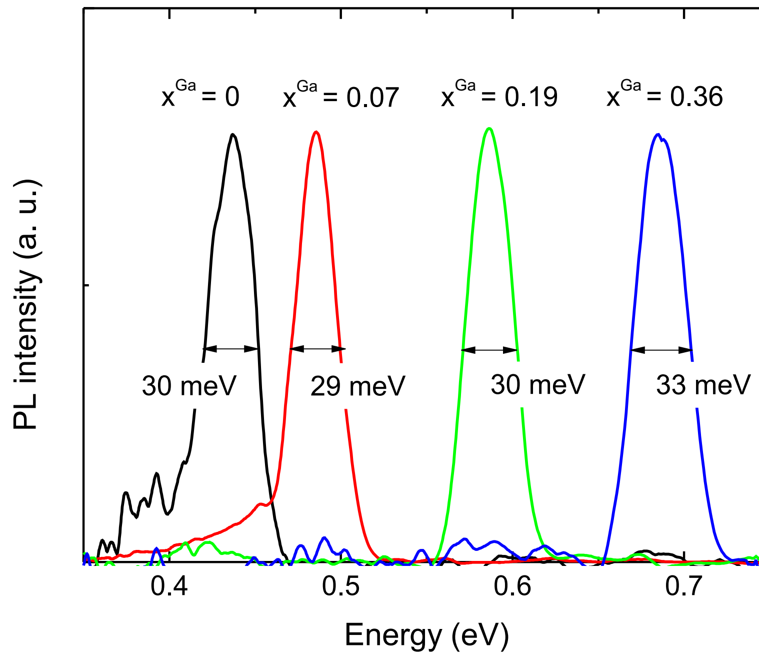

Figure 6.5. Low-T (20 K) PL spectra of several composition-tuned site-selective $In_{1-x}Ga_xAs$ nanowire arrays on NIL-SiO_2/Si(111), as measured from nanowire ensembles (dispersed onto Si substrate) with the nanowire axis lying perpendicular to the laser excitation (excitation power = 156 mW). PL spectra are normalized to the respective spectrum of binary InAs NWs [x(Ga) = 0] with x(Ga) values as quantified by HRXRD. Note that the PL linewidths are independent of x(Ga). Published in Ref. [Her12b].

nanowire arrays were mechanically transferred onto a Si substrate (nearly 1:1 transfer ratio) facilitating laser excitation perpendicular to the nanowire axis. Note that the excitation laser spot as focused to the sample had a spot diameter of ∼50 µm, corresponding to the excitation of an ensemble volume of > 10^3 nanowires. For more technical details on the PL setup see section 4.2.

The characteristic PL spectra of all $In_{1-x}Ga_xAs$ nanowire samples normalized to the intensity of the binary InAs nanowire reference sample [x(Ga) = 0] are presented in Fig. 6.5. The PL spectra show the expected trend of increasing PL peak emission energy with x(Ga) [x(Ga) given in HRXRD measured quantities]. To translate the PL peak emission energies to Ga contents x(Ga), the quadratic band gap dependence versus x(Ga) for bulk $In_{1-x}Ga_xAs$ with bowing factor of -0.475 [Goe83] is utilized. Taking further the InAs peak from this study (0.435 eV) and the ZB GaAs peak from Ref. [Spi09] (1.515 eV) as boundary conditions yields x(Ga) = 0.078, 0.215 and 0.331 for the three investigated $In_{1-x}Ga_xAs$ nanowire samples. Most strikingly, the PL linewidths (FWHM) are found as narrow as ∼29–33 meV and independent of Ga content x(Ga). Despite the huge amount of nanowires probed,

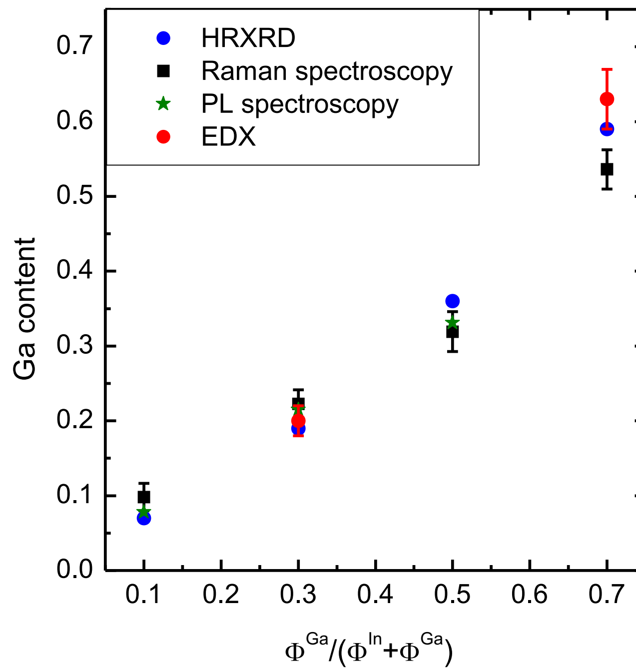

Figure 6.6. Comparison of the effective Ga content for the different $In_{1-x}Ga_xAs$ nanowire sample series as measured by various techniques such as HRXRD, Raman and PL spectroscopy and EDX. The PL emission wavelength of the sample grown with the highest $\Phi^{Ga}/(\Phi^{In}+\Phi^{Ga})$ ratio of 0.7 is out of the detection range for the used setup.

these linewidths are comparable to the state of the art of the narrowest reported low-T linewidths obtained for single [Moe09] or few InGaAs nanowires (< 15 nanowires) [Yos10]. This striking observation, together with the independence in PL linewidth under variable x(Ga), underlines the low disorder and overall uniform composition for the investigated $In_{1-x}Ga_xAs$ nanowire arrays.

Finally, in Fig. 6.6 an overview of the supplied $\Phi^{Ga}/(\Phi^{In}+\Phi^{Ga})$ ratios and the resulting effective Ga contents in the nanowires is given for the data determined by HRXRD, Raman spectroscopy, PL spectroscopy and EDX. The determination of Ga contents via HRXRD, PL spectroscopy and EDX was conducted as reported above. For Raman spectroscopy the effective Ga content was estimated based on an analysis of the GaAs-like LO peak which displays the highest dispersion with Ga content [Emu88] and is not subjected to additional contributions due to the mixed crystal nature as for instance the InAs-like TO peak [Hoe11]. The frequencies were then compared with common literature [Emu88] to estimate the Ga content. Here, the absolute error arises from the calibration of the spectrometer which is $\sim$1 cm^{-1}. It has to be pointed out that references in literature [Emu88] were commonly measured on InGaAs grown on InP that is assumed to be strained, which could lead to a

systematic error in the measurement and deviations to the data derived by the other three methods. In summary, the values for the Ga content determined by the various techniques are overall in good agreement within the experimental error.

6.4 Conclusion

In conclusion, the growth of ternary InGaAs nanowires on sputter-deposited SiO_x/Si(111) and large-scale NIL-patterned SiO_2/Si(111) substrates was investigated. High growth temperatures of 550 ℃ provided sufficient Ga and In diffusion for their effective incorporation in the composition-tuned nanowires. The composition was determined by analyzing the lattice constant shift via HRXRD for the entire sample series [i.e., $\Phi^{Ga}/(\Phi^{In}+\Phi^{Ga})$ = 0.1, 0.3, 0.5 and 0.7] and additionally via EDX for selected samples. Furthermore, the two different growth strategies were compared yielding a significantly lower FWHM of the 2θ-HRXRD-peak in the case of NIL-patterned substrates as compared to self-assembled grown nanowires. This finding was further supported by Raman spectroscopy showing lower LO/TO intensity ratios and lower LO-FWHM for both the InAs-like and GaAs-like LO modes in the case of NIL-patterned nanowire growth. This suggests better growth quality – i.e., less inhomogeneities caused by composition fluctuations across the nanowire array in the case of site-selectively grown nanowires. Finally, low-T PL measurements were presented showing that the PL emission energies vary with Ga content for the nanowire arrays. In particular, nanowire band gap tuning was shown over a significant range from $\sim$1800–2850 nm where very narrow PL peak FWHM ($\sim$30 meV) underline once again the good composition homogeneity of these growths.

Conclusion and outlook

In this thesis good control about In(Ga)As nanowire growth on Si is presented and details on the growth physics and basic structural and optical properties are elucidated. First, the main experimental growth technique molecular beam epitaxy (MBE) and associated methods such as *in-situ* reflection high-energy electron diffraction (RHEED) and quadrupole mass spectrometry (QMS) were discussed. Then, self-assembled (spatially unordered) InAs nanowire growth on SiO_x-masked Si(111) was presented as the most simple routine to achieve epitaxial nanowire growth on Si(111). Basic investigations of the nanowires by means of SEM, TEM and XRD revealed vertically aligned, untapered and droplet-free nanowires with hexagonal cross section. Furthermore, the entire growth parameter space for these InAs nanowires was delineated. Surprisingly huge growth temperature ranges were obtained with maximum temperatures up to 580 ℃ under increased V/III ratio, surpassing significantly the typical growth temperature range for catalyst-assisted, VLS-grown InAs nanowires. These conditions further highlight remarkable growth rate enhancement of axial growth rates to more than 6 µm/h. Systematic studies of the group-III and group-V flux dependencies on growth rate revealed two apparent growth regimes, an In-rich (As-limited) regime and an As-rich (In-limited) regime defined by the effective As/In flux ratio at the nanowire growth front. Further fundamental knowledge of the growth physics in high-temperature InAs nanowire growth was obtained by fully quantitative *in-situ* line-of-sight QMS, allowing direct determination of the critical desorption and thermal decomposition processes of InAs nanowires at elevated temperatures. Both under dynamic (i.e., growth) and static (no growth, ultra-high vacuum) conditions the (111)-oriented InAs nanowires were found to be thermally extremely stable. Decreased nanowire growth rate at very high-temperature growth is thus primarily limited by excess In desorption from the SiO_x-masked Si(111) surface under In-limited conditions. The remarkable capability of high-temperature growth combined with excellent thermal stability is opening up unique possibilities to process and operate InAs-based nanowire devices even at elevated temperatures (> 500 ℃).

Furthermore, various nanowire growth modes were discussed in detail, such as vapor-

liquid-solid growth (with liquid catalyst) and vapor-solid growth (without catalyst), and the dominant growth mechanism was derived for InAs nanowires. In particular, a VLS-free growth mechanism for self-induced InAs nanowires on Si(111) was demonstrated using a combination of *in-situ* RHEED and *ex-situ* SEM and TEM investigations. Both the abrupt increase in RHEED intensity and strain relaxation evidence the absence of self-formation of liquid In droplets prior to nanowire growth, independent of the supplied As/In flux ratio. A direct comparison with RHEED data of self-catalyzed (VLS) GaAs nanowires grown on Si support this finding. The catalyst-free growth mode for InAs nanowires was further confirmed by the absence of residual In droplets at the nanowire tip even for different growth termination procedures. Further evidence was provided by the non-tapered nanowire geometries over the full range of investigated As/In ratios and growth-time dependent studies with no measurable delay in nanowire growth. Moreover, In supply interruptions under remaining As pressure showed no effects on the nanowire lengths, in contrast to VLS grown nanowires.

In addition, catalyst-free site-selective growth of vertically well-oriented, high yield InAs nanowire arrays on Si(111) was established. Important advantages of this growth approach were found in the independence of the vertical nanowire growth yield from pre-wetting conditions and the selected pitch (interwire distance), resulting in consistently high yields of $\sim$90 %. The excellent control of the vertical growth directionality was confirmed by very low crystal tilt in X-ray rocking curve measurements (FWHM = 0.6°). Systematic investigations of the size scaling behavior as a function of the pitch highlighted the existence of two growth regimes within the non-catalytic growth processes: (i) a competitive growth regime for low interwire distances governed by redistribution of In adatoms over multiple nanowires as well as direct impingement, and (ii) a diffusion-limited growth regime, where growth is limited by the surface diffusion length of In adatoms on the SiO_2 surface. The surface diffusion length λ_{SiO_2} could be estimated to $\sim$750 nm at T = 480 °C. In the diffusion-limited growth regime, the radial and axial nanowire growth rates were found completely independent of the pitch, resulting in identical lengths and diameters. In good agreement with the results obtained for self-assembled nanowires, an increase in As flux resulted in longer and thinner nanowires for effective As/In ratios < 1. For higher effective As/In ratios > 1 constant axial nanowire growth rates and nanowire diameters were found, meaning that the aspect ratio remains fixed for different As fluxes. Furthermore, the nanowire tapering was investigated where decreased tapering factors for higher As fluxes and lower pitches were observed. Inverse (negative) tapering was not observed supporting the droplet-free non-VLS growth mode. These findings facilitate excellent control over nanowire formation with the possibility to tailor the nanowires to all kinds of lengths, diameters and aspect ratios

for various nanowire pitches. This knowledge is currently implemented for the growth of complex nanowire-based devices such as photodetectors, solar cells and vertically aligned wrap-around gate field-effect transistors.

Moreover, the growth of ternary InGaAs nanowires on sputter-deposited SiO_x/Si(111) and large scale nanoimprint lithography (NIL)-patterned SiO_2/Si(111) substrates was investigated. High growth temperatures of 550 °C provided sufficient Ga and In diffusion for their effective incorporation in the composition-tuned nanowires. The composition was determined by analyzing the lattice constant shift via HRXRD and additionally via EDX. Furthermore, the two different growth strategies were compared yielding a significantly lower FWHM of the 2θ-HRXRD-peak in the case of NIL-patterned substrates as compared to self-assembled grown nanowires. This finding was further supported by Raman spectroscopy showing lower LO/TO intensity ratios and lower LO-FWHM for both the InAs-like and GaAs-like LO modes in the case of NIL-patterned nanowire growth. This suggests better growth quality – i.e., less inhomogeneities caused by composition fluctuations across the nanowire array in the case of site-selectively grown nanowires. Finally, low-T photoluminescence (PL) measurements were presented showing band gap tuning over a wavelength range from $\sim$1800–2850 nm where narrow PL peak FWHM of $\sim$30 meV independent of the Ga content underlined the good quality of the growth. Future work should be conducted toward high-quality InGaAs nanowire growth with higher Ga contents (> 50 %) which is expected to be realized for growth temperatures beyond 550 °C under optimized As/In ratios. The know-how gained within this work should further facilitate the growth of nanowire heterostructures with sharp heterojunctions due to the droplet-free growth mechanism. The integration of small InAs segments or quantum dots in GaAs nanowires is long sought-after and is very interesting for basic research and photonic devices.

The microstructure of a variety of nanowire samples grown with different As/In ratios and growth temperatures were further investigated by TEM and HRXRD. TEM analysis revealed heavily disordered WZ structure with stacking faults occurring every few monolayers for InAs nanowires grown with As/In ratios of 24–81. No significant dependence of the crystal structure on the As/In ratio was observed. However, the nanowire growth temperature was found to influence the crystal structure more substantially such that longer phase pure WZ segments up to lengths of 10 nm were observed for elevated growth temperatures of 530 °C. The nanowire samples grown with different As fluxes were further analyzed by HRXRD where a significant InAs WZ h(002) reflection peak at 2θ = 25.37° was found for all investigated samples. An additional peak at 2θ = 25.45° could be attributed to InAs ZB c(111) stemming directly from cluster formation under very high As/In ratios. It will be very interesting in the future to gain perfect control over the nanowire crystal structure,

opening up the possibility to grow phase-pure WZ or ZB crystal phase, respectively, which suppresses defect-related electron scattering and is expected to enhance carrier transport of nanowire-based electrical devices such as field-effect transistors.

In addition, low-temperature photoluminescence spectroscopy was performed on InAs nanowire ensembles with similar density, length and crystal structure (wurtzite-phase with stacking faults), but substantially different nanowire diameter (40–135 nm) and the role of diameter on band-edge emission elucidated. The unpassivated nanowires showed relatively strong emission efficiency with emission up to >130 K, characteristic red-shift with temperature and low-temperature band-edge energy position of $\sim$0.41 eV identical to bulk ZB InAs, particularly for thick nanowires. Reduction in nanowire diameter gave a characteristic blue-shift ($\sim$0.435 eV for 40-nm-thin nanowires) which is related to quantum confinement effects as supported by simulations.

The findings presented in this thesis facilitate high-quality MBE growth of precisely tailorable In(Ga)As nanowires directly on Si substrate. Important prerequisites for the fabrication of nanowire-based devices are achieved, such as reproducible large scale position-controlled growth and bandgap tuning via Ga incorporation in the InAs nanowires. The latter will be particularly important for nanowire-based optical devices such as photodetectors or solar cells.

Fabrication of a Si stamp for nanoimprint lithography

To bypass the extremely long e-beam lithography writing times for processing large-scale patterned substrates for nanowire growth, nanoimprint lithography (NIL) was used offering high throughput fabrication of patterned structures with excellent quality. The basic principles of NIL have already been discussed in detail in section 5.1.2. In short, a Si stamp which exhibits the designated pattern in form of Si pillars is pressed into an imprint polymer spin-coated onto a standard SiO_2/Si(111) wafer. During this process a hole pattern is imprinted into the resist which is subsequently transferred into the SiO_2 layer by reactive ion etching. The Si stamps used to imprint substrates for growth experiments in this thesis – such as presented in chapter 5 – were commercially acquired. However, prior to this acquisition the fabrication process of home-made stamps was developed and will be reported in this chapter. In Fig. A.1 the fabrication steps are depicted in detail utilizing six schematical drawings. A Si(111) wafer – typically covered with a thin layer of native oxide (schematic 1) – was used as stamp material. In a first step, the 2-inch Si wafer is cleaved to 10 mm $\times$ 10 mm pieces. For better adherence properties of the resist the native oxide of the substrate is removed with HF followed by an annealing step to dry the surface (schematic 2). The negative e-beam resist Allresist *AR-N 7520* is then spin-coated onto the Si wafer and later

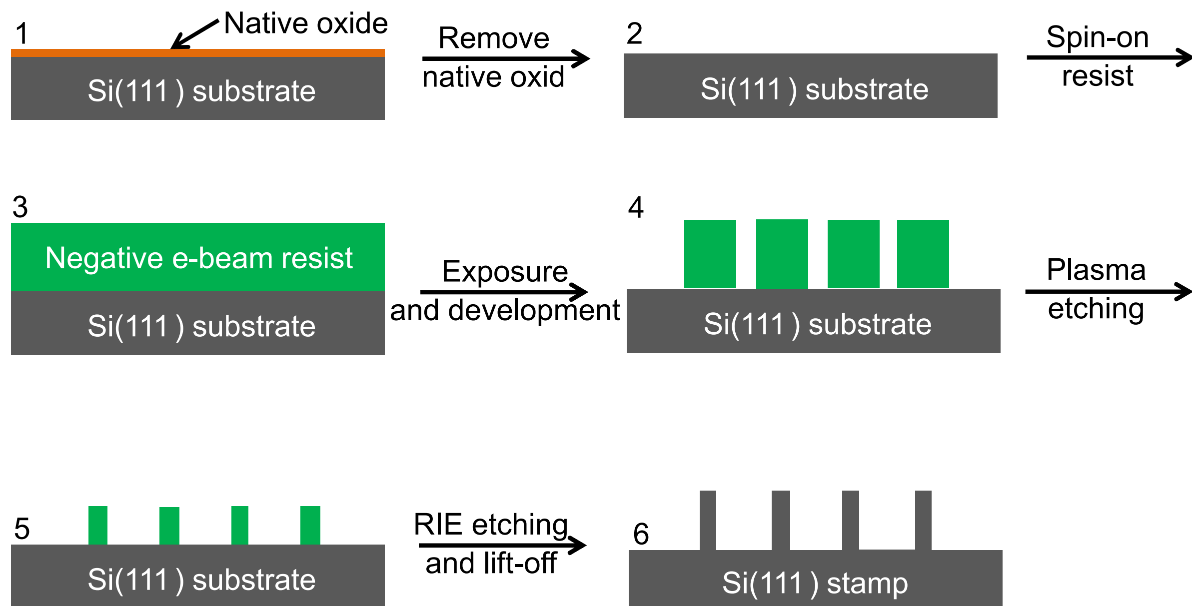

Figure A.1. Six-step illustration of the nanoimprint stamp fabrication. In a first step the native oxide of a commercial Si(111) wafer is removed in HF. Subsequently, a negative e-beam resist is spin-coated onto the wafer surface. After e-beam exposure and development, resist pillars remain on the wafer. Pillar diameters could not directly be achieved with less than 100 nm, i.e., the pillar size needs to be further reduced by O_2 plasma etching to achieve the optimum diameter of 60–80 nm. Finally, the pillar pattern is transferred into the Si wafer by plasma etching (RIE) and the remnant resist is removed with acetone.

exposed by e-beam lithography (schematic 3). When developing the resist the exposed area remains on the wafer as pillars (schematic 4). Here, it is aimed for a pillar diameter of 60 nm since nanowire growth was optimized for final hole diameters of 60–80 nm in the SiO_2 layer. However, in all cases the pillar diameter revealed to be larger than 100 nm which is a typical hint for too high exposure doses, but lower doses resulted in insufficient sticking properties at the pillar/wafer interface. A straightforward solution was found by etching the pillars in O_2 plasma to the final diameter of 60 nm (schematic 5) before transferring the pattern into the Si wafer via a second reactive ion etching step using C_4F_8/SF_6 plasma (schematic 6). The optimum pillar height is in the range of the imprint-resist thickness, i.e., $\sim$100 nm.

There are some crucial processing steps demanding additional investigation. To begin with, removing of the native oxide is very important for the sticking properties of the resist on the Si wafer. In Fig. A.2a,b AFM images are depicted to compare the pillars after resist development. Two different scenarios were investigated, i.e., the resist was spin-coated onto (i) an as-received Si wafer (with native oxide) and (ii) a wafer with removed oxide. In the first

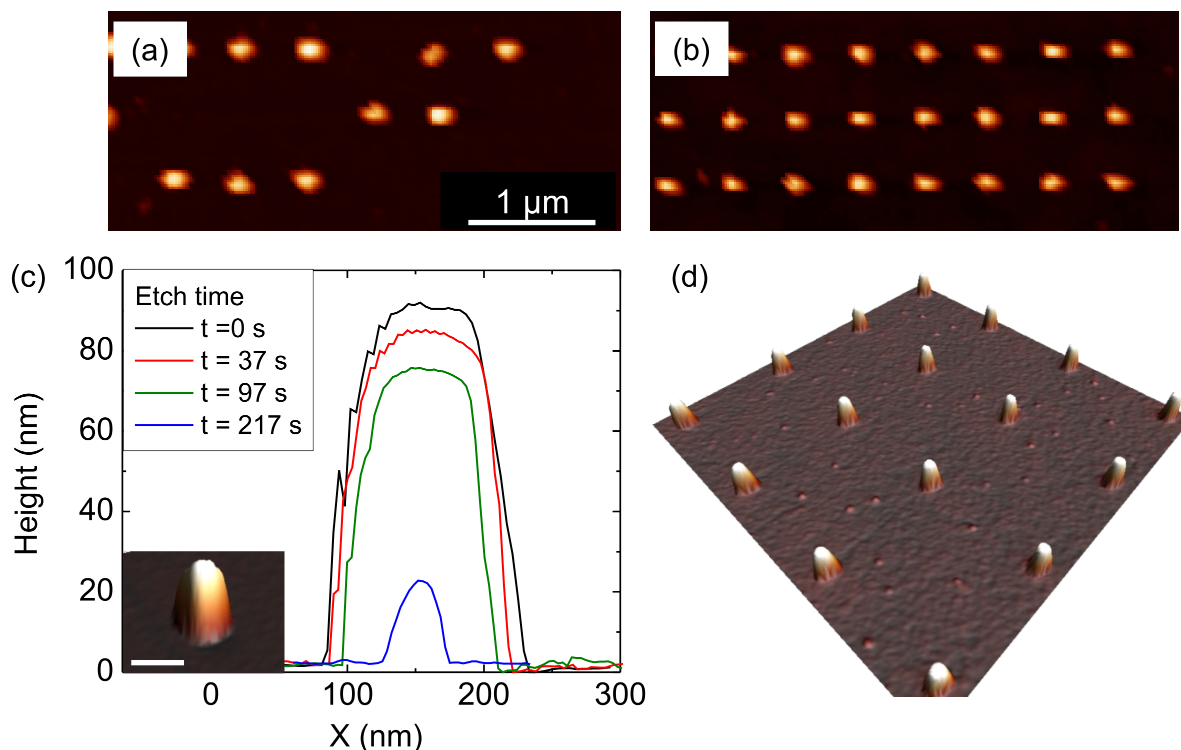

Figure A.2. (a, b) AFM micrographs of resist-pillars after development revealed the crucial role of an oxide-free and dry Si surface prior to spin-coating. The pillar yield was in the range of ∼50 % in case of spin-coating the resist onto an unprepared wafer as-received (a), whereas a perfect pillar yield without vacancies was achieved by HF oxide-removing prior to spin-coating (b). (c) AFM line scans across a single resist-pillar for different O_2 plasma treatment durations. The inset (scale bar is 100 nm) shows a 3D AFM micrograph of the pillar after 97 s plasma etching. (d) 3D AFM image of the completed Si stamp with pillar diameters of 60 nm and a pitch of 500 nm.

scenario (i), Fig. A.2a reveals several vacancies whereas Fig. A.2b representing scenario (ii) – with removed oxide – shows a perfect pattern with 100 % yield for the investigated area. It can be concluded that the resist sticks best to a dry and oxide-free wafer surface. Although oxide removal prior to spin-coating is not important for the standard e-beam process when small holes are developed in a large area of resist (see section 5.1.1), it is mandatory for the stamp fabrication – when small resist-pillars need to stick to the Si substrate.

Furthermore, the reduction of the pillar size during O_2 plasma etching was analyzed in more detail. In Fig. A.2c AFM line scans are depicted across a resist-pillar after development (t = 0 s) and for different O_2 plasma treatment durations (37–217 s). Directly after development the pillar was ∼120 nm in diameter and ∼90 nm high. The pillar size was reduced during plasma treatment in axial and radial direction with according etching

rates of 0.34 nm/s and 0.24 nm/s, respectively. After 217 s the pillar diameter was reduced to only $\sim$40 nm with a remaining height of $\sim$20 nm. Further RIE experiments revealed a high plasma stability of the resist for the Si etching in C_4F_8/SF_6 gas, i.e., a hardbake was not necessary even for very small pillar dimensions. The inset of Fig. A.2c shows a 3D AFM micrograph of one single resist-pillar after 97 s O_2 treatment (scale bar is 100 nm). The pillar exhibits a homogeneous, almost cylindrical shape with steep sidewalls enhancing the transfer quality of the pattern into the Si substrate. Finally, a 3D AFM image of the completed Si stamp is depicted in Fig. A.2d demonstrating the overall processing quality of Si pillars etched into a Si(111) substrate. The stamp exhibits a perfect yield of pillars with diameters of 60 nm and a pitch of 500 nm. Nanowire growth on substrates patterned with this particular stamp were successfully demonstrated in Fig. 5.9e with high nanowire yield of 90 %. It has to be mentioned that various pitches could be fabricated between 250 nm and several micrometer. The total size of the pattern was in the mm range – typically 3 mm $\times$ 3 mm – demanding long overnight exposures with the e-beam lithography system. As a consequence, for very large-scale patterned nanowire growth (8 mm $\times$ 8 mm) – as investigated in chapter 6 – commercially acquired, custom-made stamps were used.

A detailed step-by-step manual for the fabrication of Si stamps for nanoimprint as discussed in this chapter will be presented in appendix C.

B

Manual 1: Substrate preparation

B.1 Substrate preparation for unordered nanowire growth

Sputter deposition of a 30 nm silicon oxide mask layer

Load 2-inch wafer into the Materials Research Corporation *8620* sputter system and start a 15 min rf sputtering with the following parameters:

1. Output Power = 0.05
2. Forward RF Power = 50 W ($\Rightarrow$ RF Peak Voltage $\sim$600 V)
3. Reflected RF Power = 0 W ($\Rightarrow$ Load tuning = 522.5)

HF etching of the sputtered wafer

1. Fill one bowl with the Honeywell *ammonium fluoride etching mixture 98–2* (1 % HF).
2. Fill two bowls with deionized (DI) water and one with isopropanol (IP).
3. Submerge wafer in Honeywell *98–2* solution for 35 s and clean in water and IP.
4. Blow dry with nitrogen and check thickness of SiO_x by ellipsometry.
5. Deduce etching rate and hence the remaining etching time for a final oxide thickness of 2–5 nm.
6. Repeat the etching procedure with the calculated time and recheck the thickness.

B.2 Substrate preparation for ordered nanowire growth

Spin-coating of PMMA

1. Take a Si(111) wafer coated with ∼20 nm SiO_2.
2. Measure the exact oxide thickness with ellipsometry and note this value.
3. Use polymethyl methacrylate (PMMA) Allresist *950K 679.02* diluted in ethyl acetat.
4. Fill two bowls with acetone and one bowl IP.
5. Clean wafer in both acetone baths by applying ultrasound for 3 min.
6. Wash wafer with IP and blow dry with nitrogen.
7. Clean spinner and chuck with acetone and IP. Put wafer on chuck and start rotation. Rinse with acetone, then IP, then blow dry with nitrogen.
8. Give 3–5 droplets PMMA with pipette on the 2-inch wafer.
9. Wait 10 s and start rotation applying 6000 RPM for 40 s (no ramp).
10. Prebake wafer directly on hotplate at 180 ℃ for 5 min.

Electron beam lithography

1. Design a hole pattern with e-beam software. A circle will define a hole in the SiO_2/Si substrate.
2. Scratch a line from the middle of the wafer towards the flat for marking purposes.
3. Load the wafer into an e-beam lithography system (Raith *Eline*) and use the scratch to find the center of the wafer as well as for optics adjustments.
4. Expose the desired pattern with the following parameters:
   (a) Voltage = 10 kV, aperture = 10 µm
   (b) Writefield = 50 µm
   (c) Area: stepsize 0.02 µm, dose = 100 µC/cm^2
   (d) Single pixel line: stepsize = 0.01 µm, dose = 300 pC/cm^2
   (e) Dot: stepsize = 0.01 µm, dose = 0.1 fC/cm^2
   (f) Curved elements: stepsize = 0.005 µm, dose = 150 µC/cm^2

Development

1. Develop 60 s in a 1:3 mixture of methyl isobutyl keton (MIBK) with IP.
2. Stop development by submerging the wafer in IP for 30 s.
3. Do a first check of the structure under an optical microscope.
4. Improve the shape of the pattern by a 15 s O_2 plasma etch at 200 W.

Reactive ion etching

In the next step the pattern will be transferred into the SiO_2 layer such that 2 nm oxide will be left. Therefor, the wafer is loaded into the RIE system (Oxford *Plasmalab 80 Plus*) using the *Si-OPT4-1* etch protocol with the following parameters:

1. Gases: C_4F_8/SF_6
2. Temperature = 25 °C
3. The etching time needs to be calculated with the formula $t = \frac{d-2\text{nm}}{0.61\text{nm/s}} + 2\text{s}$, where d is the SiO_2 thickness.

Lift-off

1. 5 min acetone in ultrasound bath with subsequent wash in IP
2. 5 min O_2 plasma etching at 200 W

Final preparation prior to MBE loading

To make the wafer ready for growth a final HF dip is necessary to remove the remnant 2 nm oxide layer.

1. Use the Honeywell *98–2*.
2. Submerge the wafer for 30 s and check thickness with ellipsometry.
3. Aim for a final thickness of 5–10 nm less then the original thickness of the SiO_2 layer. Repeat etching if necessary.
4. The wafer should be loaded into the UHV environment of the MBE chamber as soon as possible (< 30–60 min).

Manual 2: Nanoimprint

C.1 Fabrication of a Si stamp for nanoimprint

Spin-coating of negative e-beam resist

1. Take a 10 mm × 10 mm Si wafer and submerge it in HF solution to remove native oxide. Clean with water.

2. Anneal wafer on hotplate at 180 °C for 10 min to ensure a dry surface.

3. Spin coat negative e-beam resist Allresist *AR-N 7520* following the procedure given in B.2. Use a lower rotation of 4000 RPM.

4. Prebake wafer directly on hotplate at 85 °C for 1 min.

Electron beam lithography

1. Design a pillar pattern with e-beam software. A circle will define a pillar in the Si stamp.

2. Avoid to scratch the wafer for durability purposes.

3. Load the wafer into the e-beam system using the parameters given in B.2 but with higher circular dose of 260 μC/cm^2.

4. 3-point alignment is necessary for larger patterns (> 1 mm^2).

Development

1. Develop 60 s in a 1:4 mixture of DI water with AR 300-47 developer.
2. Stop development by submerging the wafer in DI water for 30 s.
3. Do a first check of the structure under an optical microscope.

Oxygen plasma etching

1. Check pillar diameter with AFM.
2. Reduce pillar to the desired diameter utilizing 200 W O_2 plasma etch (lateral etching rate $\sim$0.24 nm/s).

Reactive ion etching

1. Etch 100 nm pillars into the Si wafer applying the same parameters given in B.2.
2. Etching rate of Si(111) is $\sim$3–5 nm/s (this value changes and should be calibrated prior to etching).

Lift-off

1. 5 min acetone without ultrasound, IP dip
2. 5 min O_2 plasma etching at 200 W

C.2 Imprint the stamp on a silicon wafer

All imprints were performed by Anandi Yadav (group of Prof. Lugli, TU Munich).

1. Take a 20 nm SiO_2/Si(111) wafer and spin-coat the thermal imprint polymer Microresist *mr-I 8010R* using 3000 RPM for 30 s.
2. Imprint 2 minutes at 30 bar pressure and a temperature of 165 °C. Demold temperature is 90 °C.
3. Remove residual polymer by 0_2 plasma etching using the recipe *Imprint-Simon*. The etching rate is 1.33 nm/s.
4. Transfer the pattern into the SiO_2 layer by RIE (parameters see B.2).
5. Standard lift-off.

List of acronyms

AFM Atomic force microscopy

EDX Energy dispersive x-ray spectroscopy

FET Field-effect transistor

FWHM Full width at half maximum

HRTEM High resolution transmission electron microscopy

HRXRD High resolution x-ray diffraction

IP Isopropanol

IV Current-voltage

LED Light emitting diode

MBE Molecular beam epitaxy

MIBK Methyl isobutyl ketone

ML Monolayer

MOCVD Metalorganic chemical vapour deposition

NIL Nanoimprint lithography

NW Nanowire

PL Photoluminescence

PMMA Polymethyl methacrylate

RHEED Reflection high-energy electron diffraction

RIE Reactive ion etching

SA Self-assembly

SAE Selective area epitaxy

SAG Selective area growth

SEM Scanning electron microscopy

TEM Transmission electron microscopy

UHV Ultra-high vacuum

VLS Vapor-liquid-solid

VS Vapor-solid

WZ Wurtzite

XRD X-ray diffraction

ZB Zincblende

List of Figures

1.1 Photograph and schematic of the Gen II MBE chamber 9
1.2 Photographs of the MBE substrate-ringholders 10
1.3 Calibration measurements of In, Ga and As effusion cells 11
1.4 Schematic of the RHEED technique 13
1.5 Illustration of 2D layer growth and according RHEED oscillations 14
1.6 Schematic and calibration of quadrupole mass spectrometry 16

2.1 AFM images of the SiO_x mask layer for nanowire growth 21
2.2 SEM micrograph of self-assembled InAs nanowires 23
2.3 Nanowire orientation XRD scan and nanowire/substrate interface TEM image 23
2.4 SEM images of InAs nanowires grown with varying temperature and V/III ratio 25
2.5 Axial growth rate and nanowire diameter as a function of substrate temperature 27
2.6 QMS measurements of desorbing In flux during high temperature nanowire growth 30
2.7 Nanowire volume evolution as a function of growth time 32
2.8 QMS measurements of desorbing In and As during thermal annealing of InAs nanowires 35
2.9 QMS measurements of desorbing In and As during thermal annealing of (100) and (111)B InAs substrates 36
2.10 Axial growth rate and nanowire diameter as a function of the As flux 38
2.11 Length vs. diameter plot for nanowires grown at different temperatures . . . 40
2.12 Axial growth rate and nanowire diameter as a function of the In flux 42

3.1 Schematic of different nanowire growth modes 46
3.2 Time evolution of the RHEED intensity and in-plane strain relaxation during InAs nanowire nucleation 48
3.3 SEM micrographs of the RHEED investigated InAs nanowires 50
3.4 Time evolution of the RHEED intensity during GaAs nanowire nucleation . . 51
3.5 Schematics of the RHEED experiments for VS and VLS nucleation 52
3.6 InAs nanowire length evolution over growth time 54
3.7 TEM images of the nanowire apex region after growth 56
3.8 Schematic of a growth interruption experiment 57

4.1 SEM micrographs of InAs nanowires taken for structural investigation 61
4.2 TEM micrographs and SAED patterns of single InAs nanowires grown with different As/In ratios 63

4.3 Indexed SAED pattern of InAs nanowires grown with As/In ratio of 24.2 . . . 64
4.4 TEM micrographs and SAED patterns of single InAs nanowires grown with different growth temperatures . . . 65
4.5 HRXRD 2θ–ω scans of three nanowire samples grown with different As/In ratios . . . 67
4.6 Temperature-dependent PL spectra of InAs nanowires and bulk InAs . . . 70
4.7 Excitation power dependent PL spectra for InAs nanowires with different diameters . . . 73
4.8 Nanowire diameter-dependent PL spectra and according theoretical calculation 75

5.1 AFM images for comparison of thermal and sputter-deposited Si oxide . . . 80
5.2 Schematic of substrate preparation for site-selective nanowire growth . . . 81
5.3 AFM line scans of a hole in the PMMA resist for varying development and O_2 plasma treatment durations . . . 83
5.4 Reactive ion etching rates for SiO_2 and Si(111) . . . 83
5.5 Exposure dose test for e-beam lithography . . . 84
5.6 Optical microscope and AFM image of a SAE pattern . . . 85
5.7 Schematic of the nanoimprint process for large-scale patterned substrates . 86
5.8 Positioned nanowire growth in dependence of substrate temperature . . . 88
5.9 AFM and SEM micrographs of positioned nanowire growth . . . 89
5.10 Schematic of different wetting strategies prior to nanowire growth . . . 91
5.11 Schematic and SEM micrograph of inclined nanowire growth along equivalent <111> directions on Si(111) . . . 92
5.12 XRD nanowire orientation measurements of positioned InAs nanowires . . . 93
5.13 SEM micrographs of nanowires grown with different durations . . . 95
5.14 Length and diameter as a function of growth time for different pitches . . . 96
5.15 Axial and radial growth rate as a function of growth time . . . 97
5.16 Nanowire length and diameter as a function of pitch . . . 98
5.17 Axial growth rate and nanowire diameter as a function of As flux for different hole pitches . . . 100
5.18 InAs nanowire tapering as a function of As flux and pitch . . . 101

6.1 Photograph and SEM images of site-selectively grown $In_{1-x}Ga_xAs$ nanowire arrays on nanoimprinted SiO_2/Si(111) . . . 105
6.2 SEM images of $In_{1-x}Ga_xAs$ nanowire arrays with high Ga content . . . 106
6.3 HRXRD 2θ–ω scans of several site-selective $In_{1-x}Ga_xAs$ nanowire arrays on nanoimprinted SiO_2/Si(111) . . . 108
6.4 Raman spectra of site-selective and self-assembled $In_{1-x}Ga_xAs$ nanowires . 111
6.5 Low-T (20 K) PL spectra of several composition-tuned site-selective $In_{1-x}Ga_xAs$ nanowires . . . 112
6.6 Comparison of the effective Ga content for the different $In_{1-x}Ga_xAs$ nanowire sample series . . . 113

A.1 Schematic of the nanoimprint stamp fabrication . . . 120
A.2 AFM micrographs of the nanoimprint stamp after certain processing steps . 121

List of Tables

2.1 Nanowire growth temperature range and maximum axial growth rates for varying V/III ratios 28

3.1 Nanowire length L, diameter D, and density ρ for three different As/In ratios (growth times) of 6.3–25.2 (45–12 min). 53

4.1 Growth parameters and dimensions of nanowire samples taken for structural investigation 60

6.1 Summarized data of nanowire length and diameter, HRXRD measured Ga content x(Ga) and FWHM of the InGaAs nanowire-related 2θ-peak reflection for several $In_{1-x}Ga_xAs$ nanowire arrays 109

Bibliography

[Aka94] T. Akazaki, J. Nitta, H. Takayanagi, T. Enoki, and K. Arai, Appl. Phys. Lett. **65**, 1263 (1994).

[All95] F. Allegretti, M. Inoue, and T. Nishinaga, J. Cryst. Growth **146**, 354 (1995).

[All08] J. E. Allen, E. R. Hemsath, D. E. Perea, J. L. Lensch-Falk, Z. Y. Li, F. Yin, M. H. Gass, P. Wang, A. L. Bleloch, R. E. Palmer, and L. J. Lauhon, Nat. Nanotechnol. **3**, 168 (2008).

[Art66] J. R. Arthur, J. Appl. Phys. **37**, 3057 (1966).

[Bak04] E. P. A. M. Bakkers, J. A.V. Dam, S. D. Franceschi, L. P. Kouwenhoven, M. Kaiser, M. Verheijen, H. Wondergem, and P. V. D. Sluis, Nat. Mater. **3**, 769 (2004).

[Bao08] J. Bao, D. C. Bell, F. Capasso, J. B. Wagner, T. Mårtensson, J. Trägårdh, and L. Samuelson, Nano Lett. **8**, 836 (2008).

[Bjo10] M. T. Björk, H. Schmid, C. D. Bessire, K. E. Moselund, H. Ghoneim, S. Karg, E. Lörtscher, and H. Riel, Appl. Phys. Lett. **97**, 163501 (2010).

[Bol94] C. R. Bolognesi, E. J. Caine, and H. Kroemer, IEEE Electron. Device Lett. **15**, 16 (1994).

[Bol11] J. Bolinsson, P. Caroff, B. Mandl, and K. A. Dick, Nanotechnology **22**, 265606 (2011).

[Bou08] A. I. Boukai, Y. Bunimovich, J. Tahir-Kheli, J. K. Yu, W. A. Goddard, and J. R. Heath, Nature **451**, 168 (2008).

[Bor07] M. T. Borgstroem, G. Immink, B. Ketelaars, R. Algra, and E. P. A. M. Bakkers, Nat. Nanotechnol. **2**, 541 (2007).

[Bre11] S. Breuer, C. Pfüller, T. Flissikowski, O. Brandt, H. T. Grahn, L. Geelhaar, and H. Riechert, Nano Lett. **11**, 1276 (2011).

[Bro80] S. D. Brotherton and J. E. Lowther, Phys. Rev. Lett. **44**, 606 (1980).

[Buk09] M. Bukala, M. Galicka, R. Buczko, P. Kacman, H. Shtrikman, R. Popovitz-Biro, A. Kretinin, and M. Heiblum, *29th Conference on the Physics of Semiconductors* (2009).

[Cal07a] R. Calarco, R. J. Meijers, R. K. Debnath, T. Stoica, E. Sutter, and H. Lüth, Nano Lett. **7**, 2248 (2007).

[Cal07b] E. Calleja, J. Grandal, M. A. Sanchez-Garcia, M. Niebelschutz, V. Cimalla, and O. Ambacher, Appl. Phys. Lett. **90**, 262110 (2007).

[Car08] P. Caroff, M. Jeppsson, D. Wheeler, M. Keplinger, B. Mandl, J. Stangl, A. Seabaugh, G. Bauer, L.-E. Wernersson, Journal of Physics: Conference Series **100**, 042017 (2008).

[Car11] S. D. Carnevale, J. Yang, P. J. Phillips, M. J. Mills, R. C. Myers, Nano Lett. **11**, 866 (2011).

[Che10] C. Chèze, L. Geelhaar, B. Jenichen, and H. Riechert, Appl. Phys. Lett. **97**, 153105 (2010).

[Che11] R. Chen, T.-T. D. Tran, K. W. Ng, W. S. Ko, L. C. Chuang, F. G. Sedgwick, and C. Chang-Hasnain, Nat. Photonics **5**, 170 (2011).

[Cha84] Y.-J. Chang and H. Kroemer, Appl. Phys. Lett. **45**, 449 (1984).

[Chu99] L. Chu, M. Arzberger, G. Böhm, and G. Abstreiter, J. Appl. Phys. **85**, 2355 (1999).

[Chu07] L. C. Chuang, M. Moewe, C. Chase, N. P. Kobayashi, C. Chang-Hasnain, and S. Crankshaw, Appl. Phys. Lett. **90**, 043115 (2007).

[Chu11] L. C. Chuang, F. G. Sedgwick, R. Chen, W. S. Ko, M. Moewe, K. W. Ng, T. T. D. Tran, and C. Chang-Hasnain, Nano Lett. **11**, 385 (2011).

[Cir99] G. E. Cirlin, N. K. Polyakov, V. N. Petrov, V. A. Egorov, Y. B. Samsonenko, D. V. Denisov, V. M. Busov, B. V. Volovik, V. M. Ustinov, Z. I. Alferov, N. N. Ledentsov, D. Bimberg, N. D. Zakharov, and P. Werner, Czechoslovak J. Phys. **49**, 1547 (1999).

[Cir09] G. E. Cirlin, V. G. Dubrovski, I. P. Soshnikov, N. V. Sibirev, Y. B. Samsonenko, A. D. Bouravleuv, J. C. Harmand, and F. Glas, Phys. stat. sol. (rrl) **3**, 112 (2009).

[Cir10] G. E. Cirlin, V. G. Dubrovskii, Y. B. Samsonenko, A. D. Bouravleuv, K. Durose, Y. Y. Proskurvakov, B. Mendes, L. Bowen, M .A. Kaliteevski, R. A. Abram, and D. Zeze, Phys. Rev. B **82**, 035302 (2010).

[Col08] C. Colombo, D. Spirkoska, M. Frimmer, G. Abstreiter, and A. Fontcuberta i Morral, Phys. Rev. B **77**, 155326 (2008).

[Col09] C. Colombo, M. Heiß, M. Grätzel, and A. Fontcuberta i Morral, Appl. Phys. Lett. **94**, 173108 (2009).

[Con10] V. Consonni, M. Knelangen, L. Geelhaar, A. Trampert, and H. Riechert, Phys. Rev. B **81**, 085310 (2010).

[Day07] S. A. Dayeh, E. T. Yu, and D. Wang, J. Phys. Chem. C **111**, 13331 (2007).

[Day09] S. A. Dayeh, E.T. Yu, and D. Wang, Nano Lett. **9**, 1967 (2009).

[Day10] S. A. Dayeh, Semicond. Sci. Technol. **25**, 024004 (2010).

[Deb07] R. K. Debnath, R. Meijers, T. Richter, T. Stoica, R. Calarco, and H. Lüth, Appl. Phys. Lett. **90**, 123117 (2007).

[Dic05] K. A. Dick, K. Deppert, T. Martensson, B. Mandl, L. Samuelson, and W. Seifert, Nano Lett. **5**, 761 (2005).

[Dic08] K. A. Dick, Progress in Crystal Growth and Characterization of Materials **54**, 138 (2008).

[Dic10] K. A. Dick, C. Thelander, L. Samuelson, and P. Caroff, Nano Lett. **10**, 3494 (2010).

[Dim11] E. Dimakis, J. Lähnemann, U. Jahn, S. Breuer, M. Hilse, L. Geelhaar, H. Riechert, Cryst. Growth Des. **11**, 4001 (2011).

[Din07] Y. Ding, J. Motohisa, B. Hua, S. Hara, and T. Fukui, Nano Lett. **7**, 3598 (2007).

[Dit60] W. Dittmar and K. Neumann, Z. Elektrochem. **64**, 207 (1960).

[Dua00] X. Duan and C. M. Lieber, Adv. Mater. **4**, 12 (2000).

[Dua01] X. Duan, Y. Huang, Y. Cui, J. Wang, and C. M. Lieber, Nature **409**, 66 (2001).

[Dub05] V. G. Dubrovskii, G. E. Cirlin, I. P. Soshnikov, A. A. Tonkikh, N. V. Sibirev, Yu. B. Samsonenko, and V. M. Ustinov, Phys. Rev. B **71**, 205325 (2005).

[Duf10] J. Dufouleur, C. Colombo, T. Garma, B. Ketterer, E. Uccelli, M. Nicotra, and A. Fontcuberta i Morral, Nano Lett. **10**, 1734 (2010).

[Emu88] S. Emura, S. Gonda, Y. Matsui, H. Hayashi, Phys. Rev. B **38**, 3280 (1988).

[Erc09] D. Ercolani, F. Rossi, A. Li, S. Roddaro, V. Grillo, G. Salviati, F. Beltram, L. Sorba, Nanotechnology **20**, 505605 (2009).

[Fan90] Z. M. Fang, K. Y. Ma, D. H. Jaw, R. M. Cohen, and G. B. Stringfellow, J. Appl. Phys. **67**, 7034 (1990).

[Fil87] A. S. Filipchenko, L. P. Bolshakov, and A. Naurizbaev, phys. stat. sol. (b) **87**, K1 (1987).

[Fon08a] A. Fontcuberta i Morral, C. Colombo, G. Abstreiter, J. Arbiol, and J. R. Morante, Appl. Phys. Lett. **92**, 063112 (2008).

[Fon08b] A. Fontcuberta i Morral, D. Spirkoska, J. Arbiol. M. Heigoldt, J. R. Morante, and G. Abstreiter, Small **4**, 899 (2008).

[For11] E. Forster, *Electrical characterization of InAs nanowires*, diploma thesis, Walter Schottky Insitute (2011).

[Gal07] C. S. Gallinat, G. Koblmüller, J. S. Brown, and J. S. Speck, J. Appl. Phys. **102**, 064907 (2007).

[Gao09] L. Gao, R. L. Woo, B. Liang, M. Pozuelo, S. Prikhodko, M. Jackson, N. Goel, M. K. Hudait, D. L. Huffaker, M. S. Goorsky, S. Kodambaka, and R. F. Hicks, Nano Lett. **9**, 2223 (2009).

[Gee07] L. Geelhaar, C. Cheze, W. M. Weber, R. Averbeck, H. Riechert, T. Kehagias, P. Komninou, G. P. Dimitrakopulos, and T. Karakostas, Appl. Phys. Lett. **91**, 093113 (2007).

[Ger63] D. Gerlich, J. Appl. Phys. **34**, 2915 (1963).

[Ges12] P. Geselbracht, *Charge transport in InAs nanowires*, diploma thesis, Walter Schottky Insitute (2012).

[Giv71] E. I. Givargizov, N. N. Shevtal , J. of Cryst. Growth **9**, 326 (1971).

[Giv75] E. I. Givargizov , J. of Cryst. Growth **31**, 20 (1975).

[Gla06] F. Glas, Phys. Rev B **74**, 121302 (2006).

[Gla07] F. Glas, J.C. Harmand, and G. Patriarche, Phys. Rev. Lett. **99**, 146101 (2007).

[Gob65] G. W. Gobeli and F. G. Allen, Phys. Rev. **137**, A245 (1965).

[Goe83] K.-H. Goetz, D. Bimberg, H. Jurgensen, J. Selders, A. V. Solomonov, G. F. Glinskii, and M. Razeghi, J. Appl. Phys. **54**, 4543 (1983).

[Gro89] R. D. Grober, H. D. Drew, J.-I. Chyi, S. Kalem, and H. Morkoc, J. Appl. Phys. **65**, 4079 (1989).

[Gud02] M. S. Gudiksen, L. J. Lauhon, J. Wang, D. C. Smith, and C. M. Lieber, Nature **415**, 617 (2002).

[Han05] X. Han, G. Wang, Q. Wang, L. Cao,R. Liu, B. Zou, and J. G. Hou, Appl. Phys. Lett. **86**, 223106 (2005).

[Hea96] R. L. Headrick, S. Kycia, and Y. K. Park, Phys. Rev. B **54**, 14686 (1996).

[Hei08] M. Heiß, E. Riedlberger, D. Spirkoska, M. Bichler, G. Abstreiter, and A. Fontcuberta i Morral, J. Cryst. Growth **310**, 1049 (2008).

[Hei11] M. Heiss, B. Ketterer, E. Uccelli, J. R. Morante, J. Arbiol, A. Fontcuberta i Morral, Nanotechnology **22**, 195601 (2011).

[Her96] M. A. Herman, H. Sitter, *Molecular beam epitaxy – Fundamentals and current status*, Springer-Verlag, Berlin, Heidelberg, New York (1996).

[Her10] S. Hertenberger, D. Rudolph, M. Bichler, J. J. Finley, G. Abstreiter, and G. Koblmüller, J. Appl. Phys. **108**, 114316 (2010).

[Her11] S. Hertenberger, D. Rudolph, S. Bolte, M. Döblinger, M. Bichler, D. Spirkoska, J. J. Finley, G. Abstreiter, and G. Koblmüller, Appl. Phys. Lett. **98**, 123114 (2011).

[Her12a] S. Hertenberger, D. Rudolph, J. Becker, M. Bichler, J. J. Finley, G. Abstreiter, and G. Koblmüller, Nanotechnology **23**, 235602 (2012).

[Her12b] S. Hertenberger, S. Funk, K. Vizbaras, A. Yadav, D. Rudolph, J. Becker, S. Bolte, M. Döblinger, I. Zardo, M. Bichler, G. Scarpa, P. Lugli, I. Zardo, J. J. Finley, M.-C. Amann, G. Abstreiter, and G. Koblmüller, Appl. Phys. Lett. **101**, 043116 (2012).

[Hey00] B. Heying, R. Averbeck, L. F. Chen, E. Haus, H. Riechert, J. S. Speck, J. Appl. Phys. **88**, 1855 (2000).

[Hin12] V. Hintermayr, *Electrical transport of InAs/Si heterojunction structures*, diploma thesis, Walter Schottky Insitute (2012).

[Hir95] K. Hiruma, M. Yazawa, T. Katsuyama, K. Ogawa, K. Haraguchi, M. Koguchi, H. J. Kakibayashi, J. Appl. Phys. **77**, 447 (1995).

[His64] S. E. R. Hiscocks, W. Hume-Rothery, Proc. R. Soc. (London) **282**, 318 (1964).

[Hoe11] N. Hörmann, I. Zardo, S. Hertenberger, S. Funk, S. Bolte, M. Döblinger, G. Koblmüller, and G. Abstreiter, Phys. Rev. B **84**, 155301 (2011).

[Hoo93] S. E. Hooper, D. I. Westwood, D. A. Woolf, S. S. Heghoyan, and R. H. Williams, Semicond. Sci. Technol. **8**, 1069 (1993).

[Hor89] S. Horng, K. Young, A. Khan, J. Vac. Sci. Technol. A **7**, 2039 (1989).

[How06] P. Howe, E. C. Le Ru, E. Clarke, R. Murray, and T.S. Jones, J. Appl. Phys. **98**, 113511 (2006).

[Hua01] Y. Huang, X. Duan, Y. Cui, L. J. Lauhon, K-H. Kim, and C. M. Lieber, Science **294**, 1313 (2001).

[Hua04] Y. Huang and C. M. Lieber, Pure Appl. Chem. **76**, 2051 (2004).

[Ike08] K. Ikejiri, T. Sato, H. Yoshida, K. Hiruma, J. Motohisa, S. Hara, and T. Fukui, Nanotechnology **19**, 265604 (2008).

[Ihn07a] S. G. Ihn, J. I. Song, Y. H. Kim, J. Y. Lee, and I. H. Ahn, IEEE Trans. Nanotech. **6**, 384 (2007).

[Ihn07b] S. G. Ihn and J. I. Song, Nanotechnology **18**, 355603 (2007).

[Jab08] F. Jabeen, V. Grillo, S. Rubini, and F. Martelli, Nanotechnology **19**, 275711 (2008).

[Jen04] L. E. Jensen, M. T. Björk, S. Jeppesen, A. I. Persson, B. J. Ohlsson, and L. Samuelson, Nano Lett. **4**, 1961 (2004).

[Jeo10] J. S. Jeong and J. Y. Lee, Nanotechnology **21**, 475603 (2010).

[Joh10] J. Johansson, K. A. Dick, P. Caroff, M. E. Messing, J. Bolinsson, K. Deppert, and L. Samuelson, J. Phys. Chem. C **114**, 3837 (2010).

[Kay05] B. M. Kayes, H. A. Atwater, and N. S. Lewis, J. Appl. Phys. **97**, 114302 (2005).

[Kim06] Y. Kim, H. J. Joyce, Q. Gao, H. H. Tan, C. Jagadish, M. Paladugu, J. Zou, and A. A. Suvorova, Nano Lett. **6**, 599 (2006).

[Kin08] S. W. King, R. F. Davis, R. J. Nemanich, Surf. Science **602**, 405 (2008).

[Kob02] G. Koblmüller, P. Pongratz, R. Averbeck, and H. Riechert, Appl. Phys. Lett. **80**, 2281 (2002).

[Kob04a] G. Koblmüller, *Studies of nucleation and surface kinetics in molecular beam epitaxy of GaN*, PhD thesis, TU Wien (2004).

[Kob04b] G. Koblmüller, R. Averbeck, H. Riechert, P. Pongratz, Phys. Rev. B **69**, 035325 (2004).

[Kob05] G. Koblmüller, J. Brown, R. Averbeck, H. Riechert, P. Pongratz, J. S. Speck, Appl. Phys. Lett. **86**, 041908 (2005).

[Kob07] G. Koblmüller, C. S. Gallinat, and J. S. Speck, J. Appl. Phys. **101**, 083516 (2007).

[Kob10] G. Koblmüller, S. Hertenberger, K. Vizbaras, M. Bichler, J.-P. Zhang, and G. Abstreiter, Nanotechnology **21**, 365602 (2010).

[Kob12] G. Koblmüller, K. Vizbaras, S. Hertenberger, S. Bolte, M. Döblinger, M.-C. Amann, J. J. Finley, and G. Abstreiter, Appl. Phys. Lett. **101**, 53103 (2012).

[Kog92] M. Koguchi, H. Kakibayashi, M. Yazawa, K. Hiruma, and T. Katsuyama, Jpn. J. Appl. Phys. **31**, 2061 (1992).

[Koh12] Y. Kohashi, T. Sato, K. Ikejiri, K. Tomioka, S. Hara, and J. Motohisa, J. Cryst. Growth **338**, 47 (2012).

[Kor09] E. Koren, Y. Rosenwaks, E. R. Hemesath, J. E. Allen, and L. J. Lauhon, Appl. Phys. Lett. **95**, 092105 (2009).

[Kro10] P. Krogstrup, R. Popovitz-Biro, E. Johnson, M. H. Madsen, J. Nygard, and H. Shtrikman, Nano Lett. **10**, 4475 (2010).

[Lan10] O. Landre, V. Fellmann, P. Jaffrennou, C. Bougerol, H. Renevier, A. Cros, and B. Daudin, Appl. Phys. Lett. **96**, 061912 (2010).

[Lau02] L. J. Lauhon, M. S. Gudiksen, D. Wang, and C. M. Lieber, Nature **420**, 57 (2002).

[Lee01] S.C. Lee, K.J. Malloy, and S.R.J. Brueck, J. Appl. Phys. **90**, 4163 (2001).

[Lew79] B. Lewis and J. C. Anderson, *Nucleation and Growth of Thin Films*, Academic Press, New York, San Francisco, London (1979).

[Li93] Y. B. Li, R. A. Stradling, T. Knight, J. R. Birch, R. H. Thomas, C. C. Philips, and I. T. Ferguson, Semicond. Sci. Techol. **8**, 101 (1993).

[Li09] C. Li, K. Usami, G. Yamahata, Y. Tsuchiya, H. Mizuta, and S. Oda, Appl. Phys. Express **2**, 015004 (2009).

[Li11a] T. Li, Y. Chen, W. Lei, X. Zhou, S. Luo, Y. Hu, L. Wang, T. Yang, Z. Wang, Nanoscale Res. Lett. **6**, 463 (2011).

[Li11b] S. Li, J. Wu, Z. Wang, Z. Li, Y. Su, Z. Wu, Y. Ju, G. J. Salomo, Phys. Stat. sol. rrl, online Oct. 24 (2011).

[Li11c] Z.-A. Li, C. Möller, V. Migunov, M. Spasova, M. Farle, A. Lysov, C. Gutsche, I. Regolin, W. Prost, F.-J. Tegude, and P. Ercius, J. Appl. Phys. **109**, 114320 (2011).

[Liu94] X.F. Liu, H. Asahi, Y. Okuno, D. Marx, K. Inoue, and S. Gonda, J. Cryst. Growth **136**, 250 (1994).

[Lug07] A. Lugstein, A. M. Andrews, M. Steinmair, Y. J. Hyun, E. Bertagnolli, M. Weil, P. Pongratz, M. Schrambock, T. Roch, and G. Strasser, Nanotechnology **18**, 35306 (2007).

[Mad11] M. H. Madsen, M. Aagesen, P. Krogstrup, C. Sorensen, J. Nygard, Nanoscale Research Lett. **6**, 516 (2011).

[Man06] B. Mandl, J. Stangl, T. Mårtensson, A. Mikkelsen, J. Eriksson, L. S. Karlsson, G. Bauer, L. Samuelson, and W. Seifert, Nano Lett. **6**, 1817 (2006).

[Man10] B. Mandl, J. Stangl, E. Hilner, A. A. Zakharov, K. Hillerich, A. W. Dey, L. Samuelson, G. Bauer, K. Deppert, and A. Mikkelsen, Nano Lett. **10**, 4443 (2010).

[Mar04] T. Mårtensson, C. P. Svesson, B.A. Wacaser, M. W. Larsson, W. Seifert, K. Deppert, A. Gustafsson, L. R. Wallenberg, and L. Samuelson, Nano Lett. **4**, 1987 (2004).

[Mar07] T. Mårtensson, J. B. Wagner, E. Hilner, A. Mikkelsen, C. Thelander, J. Stangl, B. J. Ohlsson, A. Gustafsson, E. Lundgren, L. Samuelson, and W. Seifert, Adv. Mater. **19**, 1801 (2007).

[Mar11] F. Martelli, S. Rubini, F. Jabeen, L. Felisari, V. Grillo, J. Cryst. Growth **323**, 297 (2011).

[Mat06] M. Mattila, T. Hakkarainen, H. Lipsanen, H. Jiang, and E. I. Kauppinen, Appl. Phys. Lett. **89**, 063119 (2006).

[Med95] G. Medeiros-Ribeiro, D. Leonhard, and P. M. Petroff, Appl. Phys. Lett. **66**, 1767 (1995).

[Mic08] W. M. Mickey Haynes, *CRC handbook on Chemistry and Physics*, CRC Press (2008).

[Mil93] A. G. Milnes and A. Y. Polyakov, Mat. Sci. and Eng. B **18**, 237 (1993).

[Moe09] M. Moewe, L. C. Chuang, S. Crankshaw, K. W. Ng, and C. Chang-Hasnain, Opt. Express **17**, 7831 (2009).

[Mur94] M. Murayama, T. Nakayama, Phys. Rev. B **49**, 4710 (1994).

[Nea83] J. H. Neave, B. A. Joyce, P. J. Dobson, N. Norton, Appl. Phys. A **31**, 1 (1983).

[nextnano] www.wsi.tum.de/nextnano

[Nob05] J. Noborisaka, J. Motohisa, and T. Fukui, Appl. Phys. Lett. **86**, 213102 (2005).

[Nog91] M. Noguchi, K. Hirakawa, and T. Ikoma, Phys. Rev. Lett. **66**, 2243 (1991).

[Nov05] C. J. Novotny and P. K. L. Yu, Appl. Phys. Lett. **87**, 203111 (2005).

[Oka93] A. Okamoto, Semicond. Sci. Technol. **8**, 1011 (1993).

[Ols96] L. Ö. Olsson, C. B. M. Andersson, M. C. Håkansson, J. Kanski, L. Ilver, and U. O. Karlsson, Phys. Rev. Lett. **76**, 3626 (1996).

[Pal08] M. Paladugu, J. Zou, Y.-N. Guo, X. Zhang, Y. Kim, H. J. Joyce, Q. Gao, H. H. Tan, and C. Jagadish, Appl. Phys. Lett. **93**, 101911(2008).

[Par02] W. I. Park, D. H. Kim, S.-W. Jung, and G.-C. Yi, Appl. Phys. Lett. **80**, 4232 (2002).

[Par06] H. D. Park, S. M. Prokes, M. E. Twigg, R. C. Cammarata, and A.-C. Gaillot, Appl. Phys. Lett. **89**, 223125 (2006).

[Per09] A. I. Persson, L. E. Fröberg, L. Samuelson, H. Linke, Nanotechnology **20**, 225304 (2009), and references therein.

[Pli10] S. Plissard, K. A. Dick, G. Larrieu, S. Godey, A. Addad, X. Wallart, and P. Caroff, Nanotechnology **21**, 385602 (2010).

[Pol93] A. Y. Polyakov, A. G. Milnes, Materials Science and Engineering: B **18**, 237 (1993).

[Por07] A. Portavoce, R. Hull, M. C. Reuter, and F. M. Ross, Phys. Rev. B **76**, 235301 (2007).

[Ram93] S. Ramo, J. R. Whinnery, and Th. van Duzer, *Fields and Waves in Communication Electronics*, 3rd edition, Wiley, New York (1993).

[Reg07] I. Regolin, D. Sudfeld, S. Lüttjohann, V. Khorenko, W. Prost, J. Kästner, G. Dumpich, C. Meier, A. Lorke, and F.-J. Tegude, J. Cryst. Growth **298**, 607 (2007).

[Rod09] S. Roddaro, P. Caroff, G. Biasiol, F. Rossi, C. Bocchi, K. Nilsson, L. Fröberg, J. B. Wagner, L. Samuelson, L. E. Wernersson, and L. Sorba, Nanotechnology **20**, 285303 (2009).

[Roe06] A. L. Roest, M. A. Verheijen, O. Wunnicke, S. Serafin, H. Wondergem, and E. P. A. M. Bakkers, Nanotechnology **17**, 271 (2006).

[Rud11] D. Rudolph, S. Hertenberger, S. Bolte, W. Paosangthong, D. Spirkoska, M. Döblinger, M. Bichler, J. J. Finley, G. Abstreiter, and G. Koblmüller, Nano Lett. **11**, 3848 (2011).

[Sat08] T. Sato, J. Motohisa, J. Noborisaka, S. Hara, and T. Fukui, J. Cryst. Growth **310**, 2359 (2008).

[Sch65] R. C. Schoonmaker, A. Buhl, J. Lemley, J. Phys. Chem. **69**, 3455 (1965).

[Sch04] L. Schubert, P. Werner, N. D. Zakharov, G. Gerth, F. M. Kolb, L. Long, U. Goesele, and T. Y. Tan, Appl. Phys. Lett. **84**, 4968 (2004).

[Sch11] K. W. Schwartz and J. Tersoff, Nano Lett. **11**, 316 (2011).

[Sea53] G. W. Sears, Acta Metall. **1**, 457 (1953).

[Sek10] H. Sekiguchi, K. Kishino, and A. Kikuchi, Appl. Phys. Lett. **96**, 231104 (2010).

[Sha10] J. N. Shapiro, A. Lin, P. S. Wong, A. C. Scofield, C. Tu, P. N. Senanayake, G. Mariani, B. L. Liang, and D. L. Huffaker, Appl. Phys. Lett. **97**, 243102 (2010).

[Shi11] J. C. Shin, K. H. Kim, K. J. Yu, H. Hu, L. Yin, C.-Z. Ning, J. A. Rogers, J.-M. Zuo, and X. Li, Nano Lett. **11**, 4831 (2011).

[Sor08] B. S. Sorensen, M. Aagesen, C. B. Sorensen, P. E. Lindelof, K. L. Martinez, and J. Nygard, Appl. Phys. Lett. **92**, 012119 (2008).

[Sun10] M. H. Sun, E. S. P. Leong, A. H. Chin, C. Z. Ning, G. E. Cirlin, Y. B. Samsonenko, V. G. Dubrovskii, L. Chuang, and C. Chang-Hasnain, Nanotechnology **21**, 335705 (2010).

[Spi09] D. Spirkoska, J. Arbiol, A. Gustafsson, S. Conesa-Boj, F. Glas, I. Zardo, M. Heigoldt, M. H. Gass, A. L. Bleloch, S. Estrade, M. Kaniber, J. Rossler, F. Peiro, J. R. Morante, G. Abstreiter, L. Samuelson, and A. Fontcuberta i Morral, Phys. Rev. B **80**, 245325 (2009).

[Sta03] E. A. Stach, P. J. Pauzauskie, T. Kuykendall, J. Goldberg, R. He, and P. Yang, Nano Lett. **3**, 682 (2003).

[Sto06] T. Stoica, R. J. Meijers, R. Calarco, T. Richter, E. Sutter, and H. Lüth, Nano Lett. **6**, 1541 (2006).

[Tan10] T. Tanaka, K. Tomioka, S. Hara, J. Motohisa, E. Sano, T. Fukui, Appl. Phys. Express **3**, 025003 (2010).

[Tak66] K. Takahashi and T. Moriizumi, Jpn. J. Appl. Phys. **5**, 657 (1966).

[Tch07] M. Tchernycheva, L. Travers, G. Patriarche, F. Glas, and J. C. Harmand, G. E. Cirlin and V. G. Dubrovskii, J. Appl. Phys. **102**, 094313 (2007).

[The11] C. Thelander, P. Caroff, S. Plissard, A. W. Dey, and K. A. Dick, Nano Lett. **11**, 2424 (2011).

[Tom07a] K. Tomioka, J. Motohisa, S. Hara, and T. Fukui, Jap. J. Appl. Phys. **46**, 1102 (2007).

[Tom07b] K. Tomioka, P. Mohan, J. Noborisaka, S. Hara, J. Motohisa, and T. Fukui, J. Cryst. Growth **298**, 644 (2007).

[Tom08] K. Tomioka, J. Motohisa, S. Hara, and T. Fukui, Nano Lett. **8**, 3475 (2008).

[Tom11] K. Tomioka, T. Tanaka, S. Hara, K. Hiruma, and T. Fukui, IEEE J. Select. Topics Quantum Electronis **17**, 1112 (2011) and references therein.

[Tra07] J. Tragardh, A. I. Persson, J. B. Wagner, D. Hessmann, and L. Samuelson, J. Appl. Phys. **101**, 123701 (2007).

[Ucc11] E. Uccelli, J. Arbiol, C. Magen,P. Krogstrup, E. Russo-Averchi, M. Heiss, G. Mugny, F. Morier-Genoud, J. Nygard, J. Ramon Morante, and A. Fontcuberta i Morral, Nano Lett. **11**, 3827 (2011).

[Urb11] A. Urban, J. Malindretos, M. Seibt, A. Rizzi, Nano Lett. **11**, 398 (2011).

[Vea] T. D. Veal et al., unpublished.

[Wag64] R. S. Wagner and W. C. Ellis, Appl. Phys. Lett. **4**, 89 (1964).

[Wan06] Y. Wang, V. Schmidt, S. Senz, and U. Goesele, Nat. Nanotechnol. **1**, 186 (2006).

[Wei09] W. Wei, X.-Y. Bao, C. Soci, Y. Ding, Z.-L. Wang, and D. Wang, Nano Lett. **9**, 2926 (2009).

[Wer09] F. Werner, F. Limbach, M. Carsten, C. Denker, J. Malindretos, and A. Rizzi, Nano Lett. **9**, 1567 (2009).

[Wu02] Z. H. Wu, X. Y. Mei, D. Kim, M. Blumin, and H. E. Ruda, Appl. Phys. Lett. **81**, 5177 (2002).

[Wu04] Z. H. Wu, M. Sun, X. Y. Mei, and H. E. Ruda, Appl. Phys. Lett. **85**, 657 (2004).

[Wun06] O.Wunnicke, Appl. Phys. Lett. **89**, 083102 (2006).

[Yan08] M. D. Yang, C. H. Hu, J. L. Shen, S. M. Lan, P. J. Huang, G. C. Chi, K. H. Chen, L. C. Chen, and T. Y. Lin, Nanoscale Res. Lett. **3**, 427 (2008).

[Yos10] M. Yoshimura, K. Tomioka, K. Hiruma, S. Hara, J. Motohisa, and T. Fukui, Jap. J. Appl. Phys. **49**, 04DH08 (2010).

[Zan07a] Z. Zanolli, M. E. Pistol, L. E. Froberg, and L. Samuelson, J. Phys: Condens. Matter **19**, 295219 (2007).

[Zan07b] Z. Zanolli, F. Fuchs, J. Furthmüller, U. von Barth, and F. Bechstedt, Phys. Rev. B **75**, 245121 (2007).

[Zar09] I. Zardo, S. Conesa-Boj, F. Peiro, J. R. Morante, J. Arbiol, E. Uccelli, G. Abstreiter, and A. Fontcuberta i Morral, Phys. Rev. B **80**, 245324 (2009).

[Zha98] Z. Zhang, J. Y. Ying, and M. S. Dresselhaus, J. Mater. Res. **13**, 1745 (1998).

[Zhe05] G. F. Zheng, F. Patolsky, Y. Cui, W. U. Wang, and C. M. Lieber, Nat. Biotechnol. **23**, 1294 (2005).

[Zhu89] A. E. Zhukov, A. R. Kovsh, V. M. Ustinov, Y. M. Shernyakov, S. S. Mikhrin, N. A. R. D. Grober, H. D. Drew, J.-I. Chyi, S. Kalem, and H. Morkoc, J. Appl. Phys. **65**, 4079 (1989).

[Zhu99] A. E. Zhukov, A. R. Kovsh, V. M. Ustinov, Y. M. Shernyakov, S. S. Mikhrin, N. A. Maleev, E. Y. Kondrat'eva, D. A. Livshits, M. V. Maximov, B. V. Volovik, D. A. Bedarev, Y. G. Musikhin, N. N. Ledentsov, P. S. Kopev, Z. I. Alferov, and D. Bimberg, IEEE Photon. Tech. Lett. **11**, 1345 (1999).

List of publications

- *High composition homogeneity in In-rich InGaAs nanowire arrays on nanoimprinted SiO_2/Si(111) grown by catalyst-free molecular beam epitaxy*
  S. Hertenberger, S. Funk, K. Vizbaras, A. Yadav, D. Rudolph, J. Becker, S. Bolte, M. Döblinger, M. Bichler, G. Scarpa, P. Lugli, I. Zardo, J. J. Finley, M.-C. Amann, G. Abstreiter, and G. Koblmüller, Appl. Phys. Lett. **101**, 043116 (2012).

- *Rate-limiting mechanisms in high-temperature growth of catalyst-free InAs nanowires with large thermal stability*
  S. Hertenberger, D. Rudolph, J. Becker, M. Bichler, J. J. Finley, G. Abstreiter, and G. Koblmüller, Nanotechnology **23**, 235602 (2012).

- *Diameter dependent optical emission properties of InAs nanowires grown on Si*
  G. Koblmüller, K. Vizbaras, S. Hertenberger, S. Bolte, M. Döblinger, M.-C. Amann, J. J. Finley, and G. Abstreiter, Appl. Phys. Lett. **101**, 53103 (2012).

- *Ultrafast photocurrents and THz-generation in single InAs nanowires*
  N. Erhard, P. Seifert, L. Prechtel, S. Hertenberger, H. Karl, G. Abstreiter, G. Koblmüller and A. W. Holleitner, submitted (2012).

- *Absence of vapor-liquid-solid growth during molecular beam epitaxy of self-induced InAs nanowires on Si*
  S. Hertenberger, D. Rudolph, S. Bolte, M. Döblinger, M. Bichler, D. Spirkoska, J. J. Finley, G. Abstreiter, and G. Koblmüller, Appl. Phys. Lett. **98**, 123114 (2011).

- *Direct observation of a non-catalytic growth regime for GaAs nanowires*
  D. Rudolph, S. Hertenberger, S. Bolte, W. Paosangthong, D. Spirkoska, M. Döblinger, M. Bichler, J. J. Finley, G. Abstreiter, and G. Koblmüller, Nano Lett. **11**, 3848 (2011).

- *Effects of stacking variations on the lattice dynamics of InAs nanowires*
  N. Hörmann, I. Zardo, S. Hertenberger, S. Funk, S. Bolte, M. Döblinger, G. Koblmüller, and G. Abstreiter, Phys. Rev. B **84**, 155301 (2011).

- *Growth kinetics in position-controlled and catalyst-free InAs nanowire arrays on Si(111) grown by selective area molecular beam epitaxy*
  S. Hertenberger, D. Rudolph, M. Bichler, J. J. Finley, G. Abstreiter, and G. Koblmüller, J. Appl. Phys. **108**, 114316 (2010).

- *Self-induced growth of vertical free-standing InAs nanowires on Si(111) by molecular beam epitaxy*
  G. Koblmüller, S. Hertenberger, K. Vizbaras, M. Bichler, J.-P. Zhang, and G. Abstreiter, Nanotechnology **21**, 365602 (2010).

List of conference contributions

- 6th Nanowire growth workshop, poster presentation.
  St. Petersburg, Russia. June 4–6, 2012.

- 17th International Winterschool on New Developments in Solid State Physics, poster presentation.
  Mauterndorf, Austria. February 12–17, 2012.

- MRS Fall Meeting & Exhibit, oral presentation.
  Hynes Convention Center, Boston, USA. November 28 – December 2, 2011.

- SemiconNano 2011, oral presentation.
  Traunkirchen, Austria. September 11–16, 2011.

- PDI topical workshop on MBE-grown Arsenide Nanowires, invited talk.
  Paul-Drude-Institut, Berlin, Germany. September 8–9, 2011.

- 5th Nanowire growth workshop, poster presentation.
  Rome, Italy. November 4–5, 2010.

- 16th International Conference on Molecular Beam Epitaxy, oral presentation.
  Berlin Congress Center, Berlin, Germany. August 22–27, 2010.

- 16th International Winterschool on New Developments in Solid State Physics.
  Mauterndorf, Austria. February 21–26, 2010.

Acknowledgments

There are so many people who helped to accomplish my thesis. In particular I would like to thank the following persons.

- Gerhard Abstreiter for giving me the opportunity to do my PhD at the Walter Schottky Institute and for countless helpful discussions during the entire time. I really appreciate the good atmosphere in the E24 group.
- Gregor Koblmüller for the supervision of my thesis and guiding the way through the nanowire jungle. Thanks a lot for discussing and correcting all abstracts, publications and this thesis, and giving me the opportunity to present my work on many international conferences. Special thanks for the organization of my research stay at UC Santa Barbara in April 2011 and for showing me the city and surroundings. I further deeply appreciate the "open door" atmosphere in your group paving the road for successful teamwork.
- Jonathan Finley and Alexander Holleitner for fruitful collaborations and support.
- Max Bichler for supporting me with expert knowledge about the MBE system and keeping it running all the time.
- Daniel Rudolph for the great teamwork on growth, RHEED investigation, processing, HF etching and conference travels.
- Stefanie Bolte and Markus Döblinger for TEM investigation and interpretation.
- Stefan Funk, Nicolas Hörmann, Sara Yazji and Ilaria Zardo for Raman spectroscopy.
- Stefanie Bolte, Emanuel Forster, Philipp Geselbracht, Verena Hintermayr and Dance Spirkoska for electrical characterization of InAs nanowires.
- Andreas Brenneis, Kun Chen, Mengyu Liang and Tao Yang for optical measurements.

- Jonathan Becker, Lukas Hanschke, Florian Herzog, Sarah Lindner and Bernhard Loitsch for endless SEM, AFM and lithography effort during their internships. Special thanks to Jonathan Becker for supporting me for two years with his various skills. Without your help it would have taken me one more year.
- Paolo Lugli, Giuseppe Scarpa and Anandi Yadav for the awesome and fruitful nanoimprint collaboration. Especially Anandi for imprinting so many wafers for us.
- Sepp Grottenthaler, Sonja Matich, Claudia Paulus, Hubert Riedl and Peter Weiser for great technical support.
- Bernhard Laumer and Fabian Schuster for XRD support.
- Kristijonas Vizbaras for PL measurements.
- Irmgard Neuner for too many things to write on that limited space. You make the WSI a place to feel at home.
- Alessandro Cavalli, Norman Hauke, Martin Heiss, Martina Hofmann, Kai Müller, Markus Schuster, Thomas Zabel and many other colleagues for having a good time.
- My family for always being there for me.

This work was supported by the Marie Curie FP7 Reintegration Grant, the EU FP7 project SOLID, the DFG excellence program Nanosystems Initiative Munich, and the collaborative research center SFB 631.